

Critical Heat Flux Phenomena at High Pressure & Low Mass Fluxes: NEUP Final Report Part I: Experiments

Reactor Concepts

Dr. Michael Corradini

University of Wisconsin-Madison

In collaboration with:

Oregon State University

Timothy Beville, Federal POC
Brian Robinson, Technical POC

NEUP 11-3080

Critical Heat Flux Phenomena at High Pressure & Low Mass Fluxes: NEUP Final Report Part I: Experiments

PART I: Experiments

Michael Corradini (UW PI) and M.Scott Greenwood

Department of Engineering Physics, UW-Madison

Corradini@engr.wisc.edu

PART II: Modeling

Qiao Wu (OSU Co-PI) and Jeff Luitjens

Department of Nuclear Engineering, Oregon State University

Qiao.Wu@Oregonstate.edu

October 15, 2014

Abstract

This report is a preliminary document presenting an overview of the Critical Heat Flux (CHF) phenomenon, the High Pressure Critical Heat Flux facility (HPCHF), preliminary CHF data acquired, and the future direction of the research. The HPCHF facility has been designed and built to study CHF at high pressure and low mass flux ranges in a rod bundle prototypical of conceptual Small Modular Reactor (SMR) designs. The rod bundle is comprised of four electrically heated rods in a 2x2 square rod bundle with a prototypic chopped-cosine axial power profile and equipped with thermocouples at various axial and circumferential positions embedded in each rod for CHF detection. Experimental test parameters for CHF detection range from pressures of $\sim 80 - 160$ bar, mass fluxes of $\sim 400 - 1500$ kg/m²s, and inlet water subcooling from $\sim 30 - 70^\circ\text{C}$. The preliminary data base established will be further extended in the future along with comparisons to existing CHF correlations, models, etc. whose application ranges may be applicable to the conditions of SMRs.

Table of Contents

Abstract	i
Acknowledgments	Error! Bookmark not defined.
Table of Contents	iii
List of Figures	v
List of Tables	viii
Nomenclature	ix
I. Introduction	1
I.A. The Critical Heat Flux Phenomenon.....	3
I.A.1. Nomenclature	4
I.B. The Small Modular Reactor	7
I.C. Concept Design	9
I.D. Research Goals.....	10
II. Literature Review	11
II.A. Existing Rod Bundle CHF Data.....	12
II.B. Parametric Trends	13
II.B.1. Inlet Subcooling	14
II.B.2. Influence of Pressure.....	15
II.B.3. Mass Flux	17
II.B.4. Non-Uniform Axial Heat Flux	18
II.B.5. Grid Spacer Effects	18
II.C. CHF Prediction Methods	20
II.C.1. Experimental Correlations & Look-Up Tables	21
II.C.2. Departure from Nuclear Boiling Mechanistic Models.....	23
II.C.3. Computational Techniques: Subchannel Analysis and CMFD.....	25
III. Experimental Facility	27
III.A. Facility Overview.....	28
III.B. Design Guidelines and Goals	29
III.C. Primary System Details.....	29
III.C.1. Main Loop Details	30
III.C.2. Test Section.....	31

III.C.3.	High Pressure Heat Exchanger	50
III.C.4.	High Pressure Pump	51
III.C.5.	Test Bypass Section	52
III.C.6.	Pressurization System	53
III.C.7.	Emergency Pressure Relief System	57
III.D.	Secondary Systems Details	57
III.D.1.	Main Supporting Structure	57
III.D.2.	Weight Bearing Spring Supports	58
III.D.3.	Secondary Cooling and Pressure Systems	60
III.D.4.	Data Acquisition System	64
III.E.	Pressure & Temperature Rating	65
IV.	Facility Performance	66
IV.A.	Safety Considerations	66
IV.B.	Start-Up	67
IV.C.	Steady State	68
IV.D.	Experimental Run	68
IV.E.	Shutdown	70
IV.F.	Error Analysis	70
V.	Preliminary Critical Heat Flux Data	72
V.A.	Inlet Subcooling	72
V.B.	Inlet Pressure	73
V.C.	Mass Flux	74
V.D.	Thermodynamic Quality	74
V.E.	CHF Location	75
V.F.	Repeatability	76
VI.	Summary & Future Work	78
	Bibliography	79
Appendix A	Official Documents	84
Appendix B	Facility Operation Procedures	88

List of Figures

Fig. 1 – The first published ‘boiling curve’ by Nukiyama in 1934 ²	2
Fig. 2 – Representative boiling curve indicating various regions of boiling ¹¹	4
Fig. 3 – Linear effect of inlet subcooling on the critical heat flux for fixed inlet condition ³²	15
Fig. 4 – Influence of pressure on the critical heat flux for a fixed inlet condition ⁵	16
Fig. 5 – Illustration of the abrupt drop in CHF over the LQR due to a shift in mechanism ²⁵	17
Fig. 6 – Quasi linear effect of mass flux on the critical heat flux for fixed inlet condition ³³	18
Fig. 7 – Enhancement of the heat transfer properties of a the coolant near a grid spacer ³⁷	19
Fig. 8 – Effect of grid spacers on the critical heat flux ³⁸	20
Fig. 9 – Portion of the 2006 LUT entered into a searchable spreadsheet	23
Fig. 10 – Schematic of the near-wall bubble crowding model ⁴¹	24
Fig. 11 – DNB CHF caused by the formation of a vapor blanket ⁴²	25
Fig. 12 – (Left) Channel centered and (Right) rod centered subchannels	26
Fig. 13 – (Left) Secondary Systems (includes TRIGA CHF Facility) and (Right) Primary Test Loop of HPCHF Facility.....	27
Fig. 14 – (Left) 2-D drawing and (Right) photo of the HPCHF primary system.	29
Fig. 15 – Basic process flow diagram and 3-D model (accumulator not shown) of the HPCHF facility...	30
Fig. 16 – Test section of the HPCHF facility with removable portion and start of the square flow channel indicated.	32
Fig. 17 – Detailed drawing of heater elements (in mm) as provided by Stern Laboratories ⁴⁶	33
Fig. 18 – (Left) Lower end of copper leads connecting to power cables (green wires for ground reference). (Right) Each cable leads to a SCR via conduit piping (top silver pipe) and attach on right of SCR. Top wires are AC power cables.....	34
Fig. 19 – Modified top hub with installed copper cooling block. The moisture seal can be seen between the white disc and cooling block and a portion of the threaded packing seal is visible between the cooling block and the Grayloc hub.	35
Fig. 20 – (Left) Bottom hub cooling block. (Middle) Modified bottom hub and cooling block. (Right) 15 cm standoff.....	36
Fig. 21 – Power profile of non-uniform heater elements as a function of heated length.....	36
Fig. 22 – TC orientation of each heater element type, heater number reference used in paper, and heater element locations.....	38
Fig. 23 – Chopped cosine power profile and associated axial thermocouple location on each heater element. Green markers indicate possible location of a grid spacer.	38
Fig. 24 – Visual comparison of the flow into the first 2.54 cm of the square channel for four inlet plenum options. The outline of the heater elements can be seen in the lower portion of each figure. Vertical and inner diameter dimensions are given for reference as images are not scaled the same. Inlet (In), tee section (Tee) and outlet (Out) have the same dimensions. Velocity color scheme is identical across all figures. .	40
Fig. 25 – Velocity contour plot of each plenum in Fig. 24 at (Left) the transition and (Right) 2.54 cm after the transition.....	41
Fig. 26 – Velocity contour plots of a straight plenum of 1) 25.4 cm, 2) 15.2 cm, and 3) 2.54 cm.....	42

Fig. 27 – Temperature contours capturing the transition (left to right) of preferential heat distribution from between the heating elements to between the heating elements and wall based on $h_{\text{gap}}/G_{\text{gap}}$ ratio.....	44
Fig. 28 – (Left) 3-D internal view of the support plate. (Right) Actual support place welded in place.	45
Fig. 29 – SS316 channel pieces (thickness of 0.3175 cm) comprising the square flow channel. Dimensions are in cm.....	45
Fig. 30 – (Left) Top end of square channel inserted into piping (Right) 3-D view of channel inserted into square plate.	46
Fig. 31 – Custom grid spacers used in HPCHF facility. (Right) Installed grid spacer on actual heater elements.	46
Fig. 32 – Comparison of predicted pressure drop from ASME correlation to calibration data of the orifice flow meter scaled to water at 275°C and 12.8 MPa.....	48
Fig. 33 – (Left) Schematic of axial bulk TC position. (Right) Bulk TCs 5-8 distribution with representation of minimal entrance into flow channel.....	49
Fig. 34 – (Counter Clockwise from Top Left) Pressure tubes and support/mixing baffles, tube sheet, high pressure inlet/outlet, installed heat exchanger with bypass valve.....	50
Fig. 35 – Installed primary heat exchanger bypass valve.	51
Fig. 36 – HPCHF Facility primary loop pump	52
Fig. 37 – HPCHF Facility primary loop pump curve	52
Fig. 38 – Simple diagram of the pressurization/thermal expansion system.....	54
Fig. 39 – (Clockwise from top left) Pneumatic control valves, pressurization tanks, concentric tube heat exchanger.	55
Fig. 40 – Primary support structure and location of test loop weight bearing supports	57
Fig. 41 – (Left) 2-D side and top view and (Right) photo of primary loop spring support	59
Fig. 42 – Support system for the high pressure heat exchanger	60
Fig. 43 – Modified TRIGA CHF Facility	61
Fig. 44 – (Left) Plate heat exchanger. (Middle) Glycol/Water tank. (Right) Glycol/water air chiller.	61
Fig. 45 – TRIGA facility (Left) before and (Right) after addition of distribution manifold	62
Fig. 46 – (Left) High pressure pump heat exchanger. (Right) Glycol/water control valves.	62
Fig. 47 – Secondary cooling manifold and flowmeters for rod pressure boundaries, pressurizer concentric tube heat exchanger and shell side of high pressure heat exchanger (flowmeter with blue top).....	63
Fig. 48 – (Left) Primary hardware for DAQ system. (Right) Screenshot of portion of LabVIEW interface.	64
Fig. 49 – Test inlet pressure (P_{in}) at CHF occurrence as a function of the test section mass flux (G_{test}) based on an initial cold starting pressure (lines) with an initial cold pressurizer water height (H_{press}) of 137 cm.....	68
Fig. 50 – Heater element thermocouple measurements for an experimental run indicating a CHF event.	69
Fig. 51 – (Left) All bulk thermocouples at CHF occurrence. (Right) Bulk thermocouples at the same axial height.....	71
Fig. 52 – The CHF as a function of inlet subcooling	73
Fig. 53 – The CHF as a function of inlet pressure	73
Fig. 54 – The CHF as a function of mass flux	74
Fig. 55 – The CHF as a function of thermodynamic quality	75
Fig. 56 – The thermodynamic exit quality as a function of (Left) mass flux and (Right) inlet pressure....	75

Fig. 57 – Axial and circumferential location of CHF occurrence detected with embedded thermocouples.	
.....	76

List of Tables

Table I – Summary of operating parameters of LWR SMR designs as reported by IAEA ¹⁶	9
Table II –Operating Range of HPCHF Facility	28
Table III – Summary of test section and heater element dimensions	28
Table IV – Thermocouple axial location from beginning of the heated length and circumferential location (0° is TC #9 for Type 1 and TC #3 for Type 2 from the orientations shown in Fig. 22) of the two types of heater elements.....	37
Table V – Outlet cross sectional plenum velocity data (m/s)	41
Table VI – Summary of Square Channel Geometry Parameters	44
Table VII – Custom orifice plate dimensions and regressed C_d	48
Table VIII – Bulk thermocouple axial location	49
Table IX – Main components of the DAQ system.....	65
Table X – Summary of Test Range of Preliminary CHF Data	72
Table XI – Average deviation between identical tests.....	77

Nomenclature

CHF	critical heat flux ($\text{kW/m}^2\text{s}$)
BO	burnout
DO	dryout
BC	boiling crisis
SMR	small modular reactor
LWR	light water reactor
NEUP	nuclear energy university program
DOE	department of energy
CFD	computational fluid dynamics
SS	stainless steel or steady state
htr	heater/heater element
D	diameter
P	pitch
h_{gap}	heater element to wall distance
G_{gap}	distance between surfaces of heater elements
L_{HL}	heated length of heater elements
q	power
q_{max}	maximum power
q_{avg}	average power

I. Introduction

In 1937, Thomas B. Drew and Alfred C. Mueller presented a paper at the American Institute of Chemical Engineers meeting in Toronto exploring an interesting link largely dismissed by the scientific base at the time¹. In this paper, the authors discuss how since man first put a pot of water on a fire it was known that the water would boil and the pot would, relatively, never be much hotter than the liquid inside it. Furthermore, if the temperature of the fire was increased, the violence of boiling would also increase. Although the Leidenfrost effect was known, it is noted that of all the investigators of heat transfer at the time, only Nukiyama appeared to recognize and investigate the existence of a ‘maximum boiling rate’ beyond which additional heating through a surface would actually decrease the heat transfer, exactly opposite the normal behavior associated with the boiling pot scenario. Nukiyama first presented his important findings and the first ‘boiling curve’ (Fig. 1) in the Japanese Journal Society of Mechanical Engineers in 1934 (reproduced in English for the first time in 1966²). The paper by Drew and Mueller presented additional data using steam heating to ‘fill in’ the gaps (between b and c in Fig. 1) with experimental data using steam heating and re-evaluated numerous data from other researches for indications of the maximum boiling rate. Their results confirmed the conclusions of Nukiyama who perhaps may be credited with the birth of the study of critical heat flux (CHF).

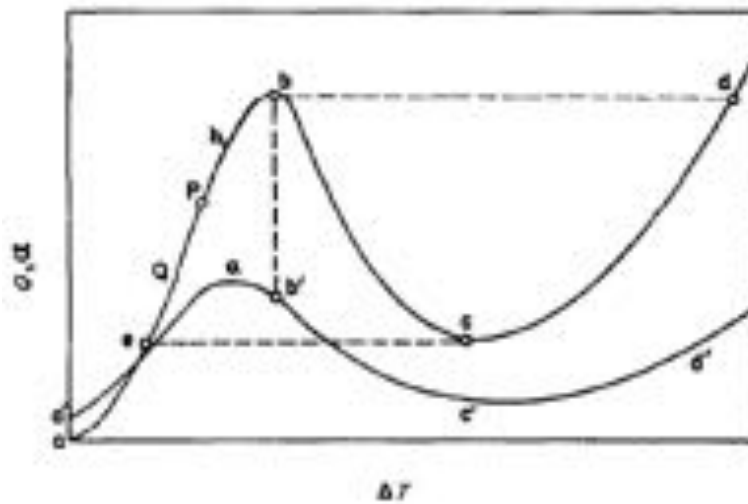


Fig. 1 – The first published ‘boiling curve’ by Nukiyama in 1934²

The implications of a maximum boiling rate beyond which heat transfer degradation would occur were quickly realized in various industries. As nuclear energy is somewhat unique both in its constant heat flux energy source and the consequence associated with fuel failure, an increased focus of the boiling rate limit grew along with nuclear energy programs. In particular, water reactors which rely on boiling as one of the steady state heat transfer mechanisms; a heat flux associated with the boiling limit event was naturally a limiting criterion in the design and operation of both boiling and pressurized water reactors (BWR/PWR).

From its first discovery, the boiling limit was quickly realized to be highly dependent on system parameters (i.e. pressure, mass flux, materials, etc.) though how was not yet known. Therefore, once initial data began to be gathered, models and mechanisms were put forth accurately describing specific experimental set ups and conditions. However, as experience grew, it was realized that no one current model, correlation, etc. was able to capture the boiling limit for each new system geometry, material, testing conditions, etc. The turbulent two phase nature of the boiling limit and its dependence eluded every effort for a completely general physical mechanism as well as any general correlation or analytical model. Undeterred, due to the critical implications of the boiling limit, enormous amounts of money were

and continue to be invested in experiments. To date, tens of thousands of public data points alone have been gathered for various purpose be it basic scientific research or for the design and operation of nuclear reactors.

This paper is a direct result of the situation previously described. New, untested systems designs (namely small modular reactors) are in need of empirical data to determine if existing methods can predict this boiling limit. If not, new methods must be determined in order to safely and efficiently design and operate this new set of systems. This paper focuses on proposed pressurized light water small modular nuclear reactor designs and their high pressure, low mass flux operating conditions as its focus.

A few references for information on two phase flow, critical heat flux, and related material in addition to and beyond what is discussed in this paper can be found in the bibliography^{3 4 5 6 7 8 9 10}.

I.A. The Critical Heat Flux Phenomenon

The boiling limit or Critical Heat Flux (CHF) is a two-phase flow phenomenon that is characterized by a flow regime change near the heater wall which rapidly decreases the efficiency of the heat transfer performance at the heater surface. The CHF condition is characterized by a local increase in vapor void fraction which covers the heater surface. The increased vapor void fraction triggers an abrupt and significant decrease in heat transfer rate between the heated surface and the two-phase coolant. The system response to a CHF event depends on the heat source; constant temperature or constant heat flux. The decrease in the heat transfer coefficient of a constant temperature heat source (e.g. steam heating) will cause the heat flux through the system to quickly decrease. A constant heat flux source (e.g. nuclear reactor, Ohmic heating) will have a rapid rise in the heating element wall temperature. The rise in temperature can lead to melting, enhanced chemical attack, and/or other metallurgical changes.

Although strictly applicable quantitatively to pool boiling, Fig. 2 qualitatively generalizes the transition in flow regime which triggers the CHF phenomenon previously described. As the temperature

difference (ΔT) between the heated wall (T_w) and fluid saturation temperature (T_{sat}) increases, the flow passes from a single phase fluid, to subcooled boiling, to saturated nucleate boiling (Region I-II). As ΔT continues to increase, the nucleate boiling becomes sufficiently vigorous that a vapor layer blankets a portion or the entire heater surface (point C), effectively ‘starving’ the heat transfer. The introduction of the vapor layer significantly increases the heat transfer resistance forcing the temperature of the heater surface to rapidly rise (for a constant heat flux source). This rise in temperature, indicative of a CHF event transitions the system from nucleate to film boiling (Region IV), characterized by conduction through a continuous vapor layer.

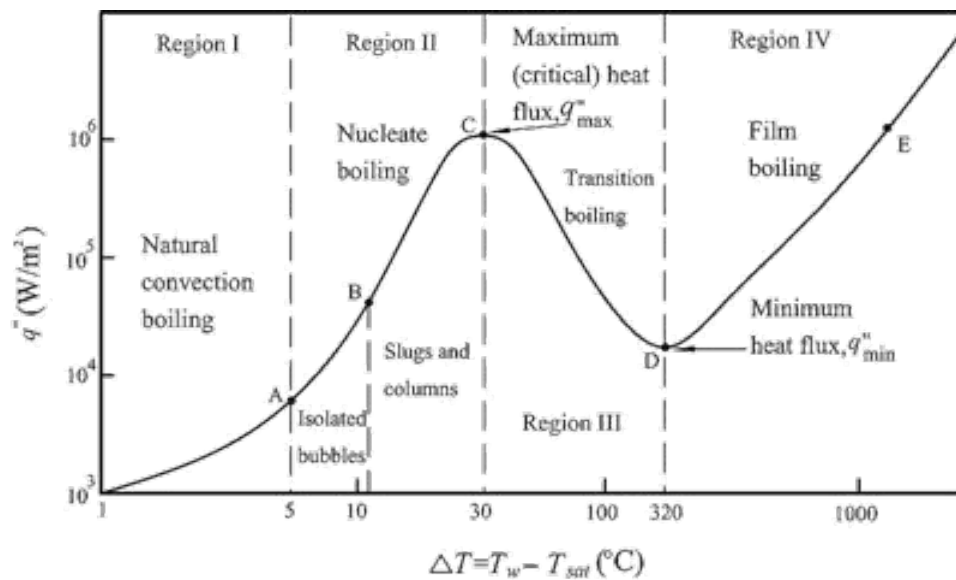


Fig. 2 – Representative boiling curve indicating various regions of boiling¹¹

I.A.1. Nomenclature

The first recorded usage in the English language of the term ‘critical heat flux’ is accredited to Zuber¹² in 1959. Over the decades in which this important boiling parameter has been under investigation, there have been numerous terms coined to label the phenomenon in an effort to better describe the actual mechanisms involved. A few of the more prominent terms that have gained credence are burnout (BO), departure from nucleate boiling (DNB), dryout (DO), critical heat flux or critical heat

flux condition (CHFC), and boiling crisis (BC). However, by the late 80s to early 90s, the term critical heat flux had become the most widely used generic term. The evolution of the use of CHF can be captured by two statements from prominent researchers. Burnout, for example, was used by G. F. Hewitt in his classic two phase text book published in 1970 ⁸. In his chapter, prominently titled ‘Burnout’, Hewitt states the following:

“The large diversity of terms tends to be confusing and this diversity reflects a continuing search for a term which is both descriptive and scientifically accurate... Although all the terms are, in one way or another, unsatisfactory... [burnout] is chosen because, for most purposes, it is the least unsatisfactory of those listed above and also because it has the widest acceptance. However, the reader should be quite clear that in a heat flux controlled system the term ‘burnout’... does not necessarily imply physical melting of the wall... In our view [critical heat flux] nomenclature... is clumsy and should not be employed.”

In contrast to Hewitt’s comments in 1970, and as a reflection of the transition to ‘critical heat flux’, J. G. Collier and J. R. Thome stated in their 1994 textbook ⁵:

“There is considerable disparity in nomenclature for the critical heat flux condition. The most common name is ‘burnout’ but this implies a physical destruction of the heated surface... The alternative forms ‘DNB’... and ‘dryout’ [and ‘boiling crisis’] are equally unsatisfactory for a *general* description of the phenomenon since they imply definite mechanisms. The term ‘critical heat flux condition’ has therefore been chosen to denote the *state* of the system when the characteristic reduction in heat transfer coefficient has just occurred... The term ‘burnout heat flux’... has been abused by many who use it to denote the heat flux at which the rapid deterioration of the cooling process occurs...”

In accordance with the apparent acceptance of ‘critical heat flux’ as the best generic term, this paper will employ the usage put forth by Collier and Thome above. Specifically, a critical heat flux condition (or event, occurrence, etc.) will characterize the state of the system when an abrupt reduction in

heat transfer occurs while the critical heat flux will refer to the heat flux of the system at the initiation of the event. Generally accepted descriptions of the primary terms noted above used to designate a CHF conditions are presented below for reference.

- Critical Heat Flux (Condition): Generally used to describe the state (i.e. flow rates, thermodynamics, etc.) of the system when a characteristic reduction in the heat transfer coefficient occurs. This nomenclature should be understood that to have a CHF event does *not* necessitate an approach to the condition by increasing the heat flux. The critical condition is met by the confluence of numerous parameters (e.g. pressure, mass flux, subcooling, etc.). The CHF condition encompasses both DNB and DO.
- Burnout: Also called ‘physical burnout’, this term is typically descriptive of the physical destruction of the heating element following a temperature excursion. Heating element destruction is not a guaranteed consequence of heat transfer deterioration as burnout heat flux may be many times greater than the actual flux at the onset of the deterioration.
- Boiling Crisis: Used by some synonymously with CHFC but is not generally used.
- Departure from Nucleate Boiling: In subcooled and low quality flows, the generally accepted mechanism of CHF is the generation of a vapor layer along the heated surface which prohibits heat transfer. The abrupt increase of heat transfer resistance leads to a sharp increase in the temperature of the heated surface. This can be a sustained or periodic event (i.e. appearance and disappearance of dry patches). Low quality DNB is believed to be the dominate CHF type associated with this particular study and various postulated mechanistic CHF predictions are presented in section II.C.2. Subcooled DNB refers to a subcooled fluid at CHF (as opposed to saturated), not to subcooled inlet conditions, and is observed, for example, under extremely high heat fluxes (e.g. fusion reactors).

- *Dryout*: In high quality regions, the balance of evaporation, entrainment, and liquid deposition on the heated surface lead to the depletion or ‘dryout’ of the thin liquid film layer. Typical dryout conditions occur in annular flows where high velocities are prevalent. These high flows lead to a post CHF heat transfer case with mildly reduced heat transfer coefficients. Since heat transfer is still relatively effective, the characteristic spike in heated surface temperature observed is reduced.

I.B. The Small Modular Reactor

From increasing contributions of intermittent power sources, introduction of micro-grids, aging infrastructure, negative anthropogenic impacts on the environment (including effects of the modernization of the ‘South’), and increasing regulation to name a few; there are numerous challenges the energy industry are working to address. Solutions for the variety of challenges faced, along with their complexity, will require the development and application of new technologies and political savvy. From a technological standpoint, a more compact nuclear reactor design dubbed a ‘Small Modular Reactor’ (SMR) has gained significant attention as a promising option to meet several of the challenges of the 21st century.

A ‘small’ nuclear power reactor is categorized according to an electrical power output of 300 MWe or less (typical based load plants are typically around 1000 MWe). The size of the reactor naturally lends itself to potential hybridization with other energy sources and industry applications along with an ability to contribute to micro-grids although it will most likely sacrifice thermal efficiency and neutron economy.

‘Modular’ refers to the ability to manufacture the major components of the reactor in a factory setting and then ship the components to the point of use. This modularity also may include all reactor cooling components (e.g. steam generator) enclosed within a single pressure vessel (also known as an integrated reactor design, IPWR). The modularity of the reactor is envisioned to significantly reduce

construction time/cost and improve standardization, quality control, etc. through an assembly line type production. Furthermore, the size and modularity of the reactor is predicted to lower capital investment by permitting additional modules to be purchased as the customers power demands change. In addition to potentially improved economics, SMR designs are focused on simplicity of design with enhanced safety features¹³. For more information, a publication of small modular reactors and specifically the NuScale Power approach¹⁴ is recommended as a starting point in addition to numerous other resources (e.g. NRC meetings¹⁵, company websites, numerous conferences presentations, etc.)

Though the successfulness of the business model is debatable (as it is still in its infancy), there are numerous reactors under design around the world ranging from traditional light water reactors (LWRs) to gas cooled to liquid metal cooled reactors. The IAEA has provided a useful overview of the status of numerous SMR designs¹⁶ from which a summary of the LWR SMR designs is presented in Table I. Lui and Fan¹⁷ provide a brief overview of a few SMR designs along with a qualitative evaluation of the technological ‘readiness’ of the most mature SMR LWR designs. Their assessment indicates an approximate ten year lead time until full deployment of a SMR. This corresponds well with timelines set forth by companies such as Oregon USA based NuScale Power which is expected to submit its design certification (DC) in the second half of 2016¹⁸ corresponding to end of year three of a ten year projected timeline presented to Energy NorthWest by NuScale Power¹⁹. First SMR commercial deployment is thus expected in the 2020s.

Table I – Summary of operating parameters of LWR SMR designs as reported by IAEA ¹⁶

Reactor	Country	Reactor Type	System Pressure (MPa)	Core Outlet Temperature (°C)	Primary Circulation
CAREM	Argentina	IPWR	12.25	326	Natural
FBNR	Brazil	PWR	16	326	Forced
CNP-300	China	PWR	15.2	302	Forced
Flexblue	France	PWR	15.5	310	Forced
IMR	Japan	BWR	15.51	345	Natural
SMART	South Korea	IPWR	15	323	Forced
ABV-6M	Russia	PWR	15.7	330	Natural
SHELF	Russia	PWR	17	320	Forced/Natural
RITM-200	Russia	IPWR	15.7	N/A	Forced
VK-300	Russia	BWR	6.9	285	Natural
VBER-300	Russia	PWR	12.7	316	Forced
WWER-300	Russia	PWR	16.2	325	Forced
KLT-40S	Russia	PWR	12.7	316	Forced
UNITHERM	Russia	PWR	16.5	330	Natural
IRIS	International	IPWR	15.5	330	Forced
mPower	USA	IPWR	14.1	320	Forced
NuScale	USA	IPWR	12.76*	329	Natural
Westinghouse	USA	IPWR	15.5	310	Forced
*IAEA value is incompatible with core outlet temperature. This pressure was taken from a NuScale presentation to the U.S. NRC ²⁰ .					

I.C. Concept Design

The University of Wisconsin High Pressure Critical Heat Flux facility (HPCHF) design was based on available open literature, focusing primarily on the more mature SMR designs of NuScale Power and the Babcock & Wilcox mPower. Specifically, the geometry of the test section of the facility is a square heater element array enclosed in a rectangular channel, mimicking a unit cell of the larger fuel bundle. The power profile of each heater element is a chopped cosine axial power heater profile 2.0 m long. The remainder of the facility was designed to operate between approximately 8.0 – 16.0 MPa, 400 – 1500 kg/m²s, inlet subcooling of 30 – 70°C, and power levels associated with conservative CHF predictions. In lieu of natural convection as height restrictions necessitate alternative solutions, low flow

forced convection of the coolant was applied via a high pressure pump. It has been determined that this is an acceptable alternative as there is no apparent dependency of the CHF on the circulation type, only the actual flow rate^{21 22}.

I.D. Research Goals

As outlined in the summary of the funding proposal to the Nuclear Energy University Program (NEUP) funded by the U.S. Department of Energy (see Appendix A), the purpose of this research is to provide ‘validation data for an updated critical heat flux model for use in thermal-hydraulic computer codes’ and improve ‘understanding of the CHF process... in a rod bundle geometry’ for SMR designs (e.g. NuScale PWR, Babcock-Wilcox mPower) for which data do not currently exist. In fulfillment of the scope of the project, the necessary work was divided in to four specific goals/tasks.

1. Perform a scaling analysis for rod bundle geometry appropriate for SMR designs
2. Design and construct a CHF test facility
3. Create a CHF database from gathered experimental data
4. Compare the CHF data with current correlations and develop a more mechanistic model

Requirements of the first task are with described in section III.C.2 as appropriate. The second task is the focus of section III with the basic performance of the facility discussed in section IV. The third and fourth goals are in progress. Preliminary data and the future work necessary to satisfy the third and fourth goal are discussed in sections V and VI respectively.

II. Literature Review

Over the last several decades, enormous amount of monetary and person resources have been spent on acquiring CHF data for a myriad conditions. The data bank collected by Atomic Energy of Canada Limited (AECL) and Institute of Physics and Power Engineering (IPPE) contains over 30,000 non-proprietary data points for water cooled tubes dating from as far back as the 1964 publication of the first collection of CHF data (3,800 points)²³. It is from this database that the oft referenced ‘Look-Up Tables’ (LUT) are derived (i.e. the 1986²³, 1995²⁴, and 2006²⁵ versions). Experimental CHF data, such as that mentioned above, is typically used to create correlations for CHF prediction and validate mechanistic models. Unfortunately, once derived, these methods still suffer from narrow regions of application, bounded by the data from which they are built. The complex, two phase nature of the CHF condition has so far thwarted the scientific community’s ability to generalize the prediction of the CHF condition. It is for this reason more than 1000 correlations have been presented for varying conditions²⁵.

Whatever the limitations, given the large number of experiments performed using simple tube type geometries, many attempts have been made to use existing databases, correlations, and mechanistic models to create a general and reliable prediction method for more complex geometries and parameters (e.g. rod bundles and non-uniform heat fluxes). The general approach of relating uniform tube data to other conditions is with the application of a correction coefficient that attempts to capture trends observed by experimental data (e.g. Tong F-Factor Method). These methods have been met with varying levels of success that are once again bounded, just as with the tube data, by the narrow ranges of data upon which their derivation is based. Therefore, owing to the critical importance of the CHF phenomenon limitation in design and operation of various systems, continued resources have been allotted to numerous rod bundle CHF experiments.

II.A. Existing Rod Bundle CHF Data

To the author's knowledge, there are currently two collections of rod bundle CHF data open to the public. The first known compilation of rod data was performed by Baker, Ka-Lam, Carbon, and Hughes^{26 27}. This data bank is a collection of over 4000 data points from various researches which were compiled into a computer program and evaluated for distribution of testing parameters and comparison to correlations. Unfortunately, the databank contact no longer keeps the database so it appears that the computer program is no longer in existence. However the publications do include a detailed list of the source of all the data. In addition to the data sources' primary parameters have been noted facilitating comparison of the conditions of the CHF data to the conditions associated with this research (i.e. high pressure, low mass flux of SMRs).

The authors of this databank note that there was almost no data in the medium pressure ranges, specifically between 10-13 MPa, heated lengths between 1.83-2.44 m, and non-uniform axial heat flux. A closer look at the parameters associated with the various data sources further reveals that there were no data that meet all the conditions associated with prototypic SMRs. Any non-uniform axial heat flux data was either at too great of mass fluxes and pressures or far too long heated lengths and at too low of pressures.

The second collection is a series of experiments performed at the Heat Transfer Research Facility at Columbia University over a period of approximately 20 years culminating in a final three volume report^{28 29 30 31} in 1982 to the Electric Power Research Institute (EPRI), who maintains the database today. The database contains over 11,000 points from covering numerous test sections and wide range of both BWR and PWR flow conditions. The databank was analyzed using the subchannel code COBRA from which the EPRI correlation was created.

Examination of the general parameters covered by this databank summarized by various plots in the report suggests that there is limited data between 10-12 MPa and no data with a heated of length of 2

nor any in a 2x2 array (smallest is 3x3). Further inspection of the experimental data indicates little, if any, data with a non-uniform axial flux at low mass flux (less than approximately $1300 \text{ kg/m}^2\text{s}$). If additional sub categorization of the experimental data was performed further limitations of the parameters covered would likely be evident. This suggests that while various aspects of SMR conditions are covered by this database, there is limited to no data available that satisfies a multiple parameter criteria (i.e. pressure, subcooling, mass flux, and non-uniform axial flux) necessary to predict relevant CHF conditions.

II.B. Parametric Trends

As part of the effort to define mechanisms and produce accurate correlations, the scientific community has gone to great lengths to understand what system parameters influence the CHF. It has been determined that there are two general categories in which system variables may be categorized: primary and secondary. Primary variables are defined as those which significantly alter the CHF condition. These primary parameters have been determined to be inlet subcooling, system pressure, mass flux (velocity), geometry (e.g. length, diameter). Secondary parameters are those whose influence is generally dominated by the primary variables' effects. These secondary variables therefore have, in general, little effect on the CHF. Examples of secondary variables include the method of heating, system materials (including heated wall thickness and surface roughness), and channel orientation. It should be noted that certain 'secondary' parameters (e.g. channel orientation) may change the CHF value significantly but is still controlled by the primary parameters (i.e. difference in CHF between horizontal and vertical channels decreases as the mass velocity and/or system pressure is increased and the system diameter is decreased⁵).

The wide range of investigated parameters and the amount of literature summarizing the results do not lend themselves to a completely inclusive discussion within this document as the primary scope of this research is on rod bundle power reactors. Therefore, only pertinent parameters with direct

implications to this thesis (e.g. saturated DNB CHF) will be discussed in additional detail. Any variables not discussed are assumed to negligibly affect the CHF in this study or are not applicable based on discussions in the literature.

It is evident from the literature that there are a significant variety of approaches to viewing data in efforts characterize parameter effects. A useful approach is to entertain the study of a topic based on what will be termed the ‘fixed inlet’ approach. This terminology is not unique to the present discussion. In the operation of the facility the controlled and measured flow parameters are inlet subcooling, inlet pressure, and mass flux. ‘Fixing’ all but one of these parameters is known as a fixed inlet condition. CHF trends associated with variation of these measurables will be described. A shortcoming of this approach is that this method fails to capture some less obvious variations such property changes associated with pressure. However, in the author’s opinion, this simple and general approach captures the macro view of the CHF phenomenon thereby permitting an easily understood foundation from which more in depth examinations can be initiated.

II.B.1. Inlet Subcooling

Inlet subcooling (enthalpy, Δh_{sub} or Δi_{sub} , or temperature, ΔT_{sub}) is the difference of the saturated (h_{fsat} , T_{sat}) and the inlet (h_{in} , T_{in}) enthalpy/temperature. Over wide ranges of subcooling the CHF increases approximately linearly with increased inlet subcooling. A set experimental data often referenced in literature is that of Weatherhead³² plotted in Fig. 3 illustrating this linear dependence. Additional studies^{33 34} suggest that at low mass fluxes ($G < 500 \text{ kg/m}^2\text{s}$) the effects of subcooling are diminished and are potentially negligible. Likewise at other extreme conditions (e.g. very high subcooling) other non-linear behaviors may be observed^{7 33}.

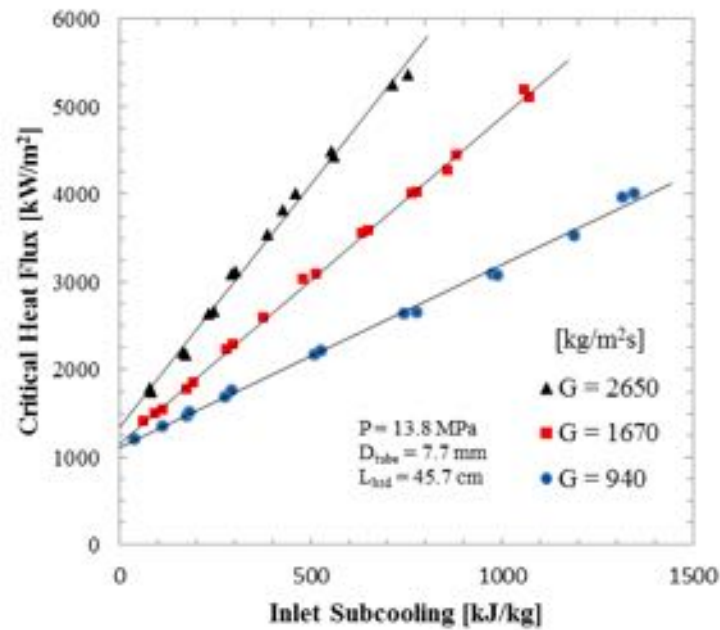


Fig. 3 – Linear effect of inlet subcooling on the critical heat flux for fixed inlet condition³²

II.B.2. Influence of Pressure

The pressure (P - local, inlet, or exit) is often referred to as the system pressure. With this usage, it is assumed that the channel pressure loss as compared to the static system pressure is negligible. Pressure effects on the CHF are complex though some generalities may be made. In the fixed inlet approach, CHF typically increases with pressure at low pressures, attains a maximum, and then decreases with increasing pressure (Fig. 4). Additional discussions on other trends observed with pressure are readily available⁵⁻⁹.

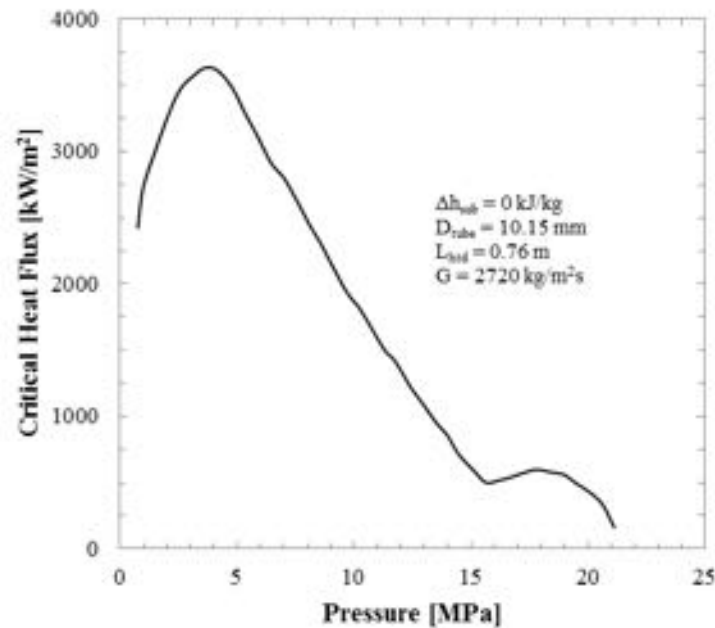


Fig. 4 – Influence of pressure on the critical heat flux for a fixed inlet condition⁵.

A proposed explanation of this parabolic behavior is based on a balance of evaporation rate and entrainment. The evaporation rate increases as pressure increases due to a decreasing latent heat of vaporization which is reflected in a decreasing CHF value. Entrainment rate is proportional to the ratio of the specific volume of the steam to water. Therefore, if the entrainment rate is larger, the CHF will increase due to enhanced wetting and more uniform dispersion of the vapor. As pressure increases the specific volume ratio decreases, thereby reducing the entrainment rate and diminishing CHF enhancement. These two competing forces are believed to contribute to the behavior of the CHF and pressure and, thus, may explain the diminishing CHF value at higher pressures³⁵.

An additional observation requiring mention is the second maximum occurring in high pressure region. This phenomenon is believed to be attributed to the limiting quality region (LQR). This region is defined where the CHF rapidly decreases with an increase in steam quality associated with what is believed to be a change in mechanism as the steam quality changes. Bennet et al.³⁶ and Groeneveld et al.²⁵ among others illustrate this approach in their papers as shown in Figure 8. Region I is characterized by

a thick liquid layer being depleted from the heated surface via entrainment in vapor while Region III is characterized by a thin liquid film replenished by the deposition of entrained droplets from a thick vapor stream. Region II is the LQR which transitions between these two mechanisms. This phenomenon is generally associated with intermediate to high steam qualities associated with annular flow and is therefore not an expected behavior for experimental data produced from this research.

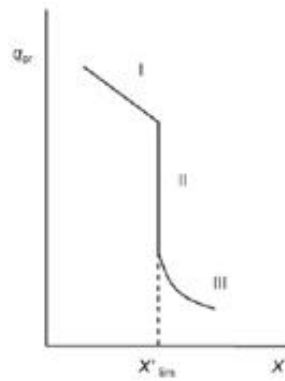


Fig. 5 – Illustration of the abrupt drop in CHF over the LQR due to a shift in mechanism²⁵

II.B.3. Mass Flux

From a fixed inlet condition, the CHF has been shown to increase with increasing mass flux (G) (Fig. 6) in a quasi linear behavior. This dependency is generally greater at lower flow mass fluxes and diminishes at higher pressures, presumably dependent on the change of flow patterns. Additional means of viewing mass flux dependency is elaborated upon by Tong & Tang⁹.

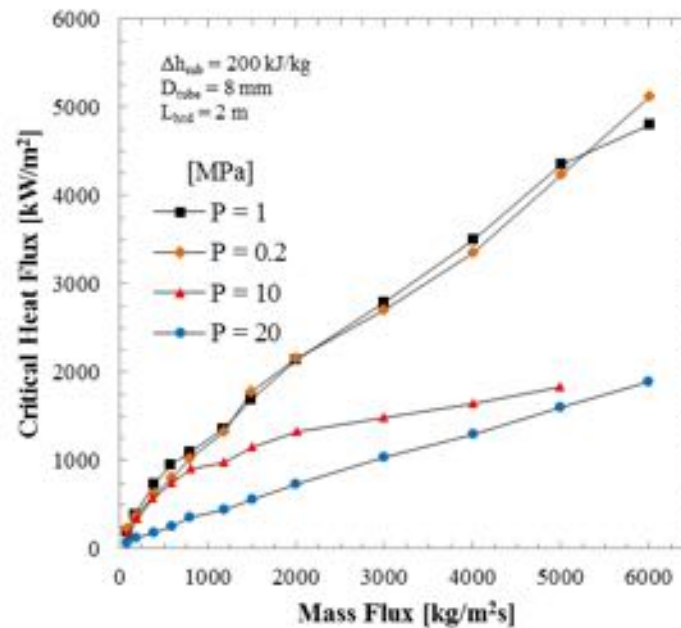


Fig. 6 – Quasi linear effect of mass flux on the critical heat flux for fixed inlet condition³³

II.B.4. Non-Uniform Axial Heat Flux

Depending on the type of non-uniformity of the axial heating profile (e.g. skewed, sinusoidal, spike), various influences on the CHF may occur. In regards to a heat profile where only part of a full sine wave (i.e. chopped cosine/sine) is used, the CHF will occur upstream of a comparable uniformly heated section with an ‘overall’ power reduction of approximately 5-10% for the non-uniform heat flux^{5 10}. A good summary of additional non-uniform heat flux effects is presented by Collier and Thome⁵.

II.B.5. Grid Spacer Effects

Grid spacers have multiple purposes. As the name suggests, the primary use is to secure the heater elements to prevent significant movement (e.g. vibrations, sliding) that induces wear and alters the thermohydraulic of the system in undesired ways. An additional purpose is to apply mixing vanes to increase the turbulence, and thus the heat transfer, of the coolant. This research employs grid spacers only for physically securing the heater elements and are thus as minimally intrusive as possible.

The effects of grid spacers have generally been shown to significantly increase the local CHF just downstream of the spacers, primarily a result of the increased turbulence. Some supporting data is shown in Fig. 7 demonstrating the increase of the Nusselt number (Nu) from the base case (no spacer present – Nu_0) over the downstream distance from the spacer. The local increase in the heat transfer effect results in the enhanced CHF as sketched in Fig. 8. ‘Simple grids’ or those with no mixing vanes and minimal flow blockage have been shown to generally not significantly alter the CHF²⁹.

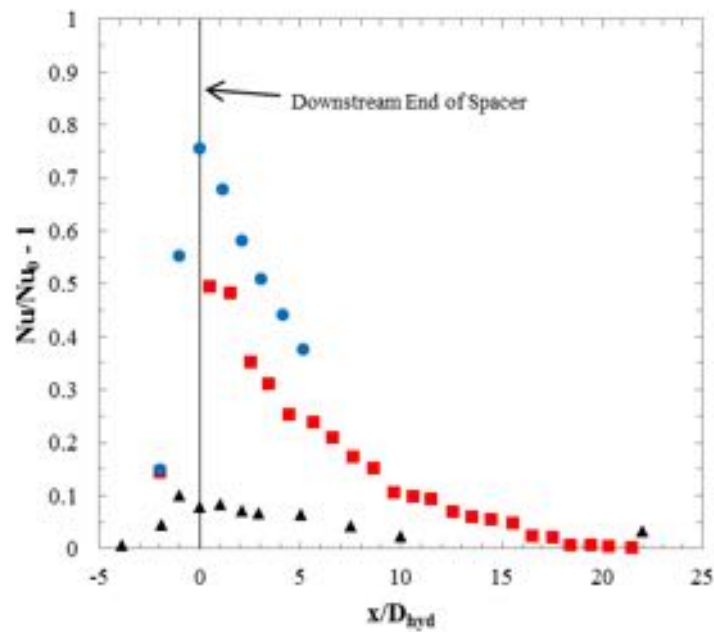


Fig. 7 – Enhancement of the heat transfer properties of a the coolant near a grid spacer³⁷

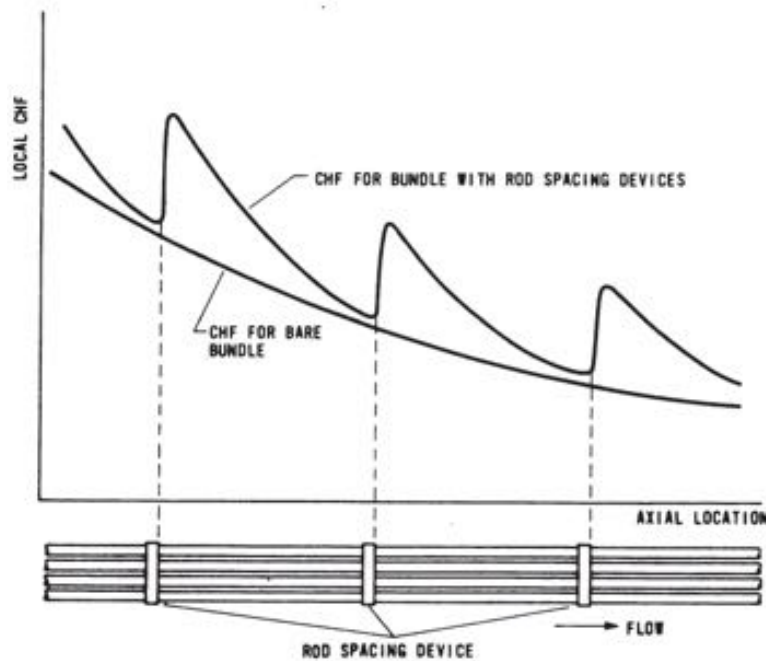


Fig. 8 – Effect of grid spacers on the critical heat flux³⁸

II.C. CHF Prediction Methods

As previously mentioned, there have been hundreds if not thousands of correlations, models, etc. created in an effort to accurately predict the CHF of various specific applications. Historically, applied methods suffer from limited ranges of applicability. These methods are prone to drastic differences in predicted and observed CHF values when used outside their range of applicability. Understandably there would be a great advantage if one correlation or model could predict the CHF of any general problem. As of this report, a unifying method has not been established. Therefore, presented below are a few methods that have met with promising results in their respective applications. These same methods will eventually be used to compare the data from this project. Additional methods may be included in the future (e.g. 1967 Biasi, Tong F-Factor).

II.C.1. Experimental Correlations & Look-Up Tables

CISE-GE or GEXL Correlation

This correlation was developed for the General Electric BWR program in 1977 from data taken from the ATLAS Heat Transfer facility³⁹. The form of the correlation is based on the CISE correlation hence CISE-GE. GEXL is the original name of the correlation as it is a critical quality (X), boiling length (L) correlation: GEXL.

$$x_{CHF} = \frac{AL_B}{B + L_B} \left(\frac{1.24}{R_f} \right)^{\frac{1}{2}} \quad (1)$$

$$A = 1.055 - 0.013 \left(\frac{(P - 4.137 \times 10^6)^2}{2.758 \times 10^6} \right) - 1.233(7.37 \times 10^{-4} G)^2$$

$$+ 0.907(7.37 \times 10^{-4} G)^2 - 0.205(7.37 \times 10^{-4} G)^3$$

$$B = 0.457 + 2.003 \left(7.37 \times 10^{-4} G \right)^2$$

$$G \Rightarrow \text{mass flux} \left[\frac{\text{kg}}{\text{m}^2 \text{ s}} \right]$$

$$x_{CHF} \Rightarrow \text{thermodynamic quality at CHF} [-] ; L_B \Rightarrow \text{boiling length [m]}$$

$$R_f \Rightarrow \text{radial peaking factor in fuel assembly} ; P \Rightarrow \text{pressure [Pa]}$$

Validated Range:

$$5.52 < P < 9.65 \text{ MPa} ; 135 < G < 1700 \text{ kg/m}^2\text{s} ; 0 < \Delta h_{\text{sub}} < 230 \text{ kJ/kg}$$

EPRI Correlation

The EPRI correlation (Equation(2)) is a result of the studies performed at the Heat Transfer Research Facility discussed previously in an effort to improve the predictive capability of the COBRA-3C subchannel code ²⁹ . The form of the method is based on the assumption that the CHF is linearly dependent on inlet subcooling and does require iteration.

$$q''_{CHF} = \frac{AF_A - x_{in}}{CF_g F_C F_{nu} + \left[\frac{x_{local} - x_{in}}{q''_{local}} \right]} \quad (2)$$

$$A = P_1 P_r^{P_2} G^{P_5 + P_7 P_r} ; C = P_3 P_r^{P_4} G^{P_6 + P_8 P_r}$$

$$P_1 = 0.5328; P_2 = 0.1212; P_3 = 1.6151; P_4 = 1.4066; P_5 = -0.3040; P_6 = 0.4843; P_7 = -0.3285; P_8 = -2.0749$$

$$q''_{CHF,local} \Rightarrow \text{critical and local heat flux} \left[\frac{Btu}{hr ft^2} \right]$$

$$x_{local,in} \Rightarrow \text{local and inlet thermodynamic quality} [-]$$

$$P_r = \frac{P}{P_{critical}} \Rightarrow \text{reduced pressure} ; G \Rightarrow \text{mass flux} \left[\frac{10^6 lb_m}{hr ft^2} \right]$$

$$\text{If Cold Wall Effects are Applicable: } F_A = G^{0.1}; F_C = 1.183G^{0.1} ; \text{ else } F_A = F_C = 1.0$$

$$\text{If Grid Spacer Effects are Applicable: } F_g = 1.3 - 0.3K_g ; \text{ else } K_g = 1 \text{ yielding } F_g = 1.0$$

$$K_g \Rightarrow \text{grid spacer pressure loss coefficient}$$

$$\text{If Non-Uniform Axial Profile: } F_{nu} = 1 + \frac{1-Y}{1+G} \text{ where } Y = \frac{1}{L} \int_0^L \frac{q''(z)}{q''_{local}} dz ; \text{ else } F_{nu} = 1.0 ;$$

Validated Range:

$$1.38 < P < 16.9 \text{ MPa} ; 270 < G < 5560 \text{ kg/m}^2\text{s} ; -0.25 < x_{local} < 0.75 ; -1.10 < x_{in} < 0.0$$

$$0.76 < L_{htd} < 4.27 \text{ m} ; 0.889 < D_{hyd} < 1.397 \text{ cm} ; 0.965 < D_{rod} < 1.60 \text{ cm}$$

The 2006 Look-Up Table

In a joint effort by AECL and IPPE, a very large databank of CHF data was created. Various statistical methods were then applied to the database in order to create a table for which one could determine the CHF of a system based on the pressure, mass flux, and critical quality relying on linear interpolation between tabulated values. This table was first published in 1986 with additional revisions, expansions, and improvements in 1995 and 2006 as mentioned previously. As part of this project, the 2006 Look-Up Table (LUT) ²⁵ into an easily accessible spreadsheet format allowing for interpolation quickly and efficiently over the entire table (Fig. 9).

Fig. 9 – Portion of the 2006 LUT entered into a searchable spreadsheet

II.C.2. Departure from Nuclear Boiling Mechanistic Models

Under low quality conditions, typically the flow characteristics associated with the CHF occurrence are agglomerations of vapor in the near-wall region and liquid in the center channels. The governing heat transfer mechanisms are bubble growth, detachment, and their migration from the wall into the liquid bulk. The details associated with these general mechanisms are not so decisive resulting in many proposed mechanisms⁴. Two of the more promising explanations is the near-wall bubble crowding model first introduced by Tong⁴⁰ and carried on by Weisman and Pei⁴¹ and the liquid sublayer

dryout theory proposed by Lee and Mudawwar⁴² and extended to low quality flows by Lin, Lee, and Pei⁴³.

Near-Wall Bubble Crowding Model - Weisman and Pei

During low quality boiling, a bubbly layer grows along the channel until it covers a region near the wall where turbulent eddies are too small to transport bubbles from the surface radially. This condition occurs when the volume fraction of steam in the layer exceeds the fraction permitting flattened ellipsoidal bubbles from having significant contact. CHF is assumed to occur at the location of this bubbly layer.

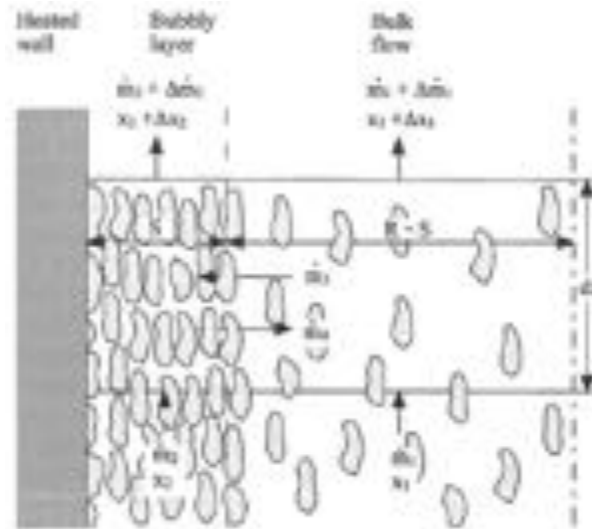


Fig. 10 – Schematic of the near-wall bubble crowding model⁴¹

Formation of a Vapor Blanket – Lin, Lee, and Pei

It has been observed that the coalescence of bubbles near the heated wall may form an extended vapor formation or blanket, trapping a thin liquid film to the wall⁴² (Fig. 11). Ingress of the liquid is restricted, thus a CHF condition will occur when the heat supplied is greater than the cooling at the surface. The prediction of the blanket and subsequent CHF event is based on Helmholtz instabilities at the

liquid/vapor interface. The Helmholtz instability occurs due to large relative velocity difference between liquid and vapor flows.

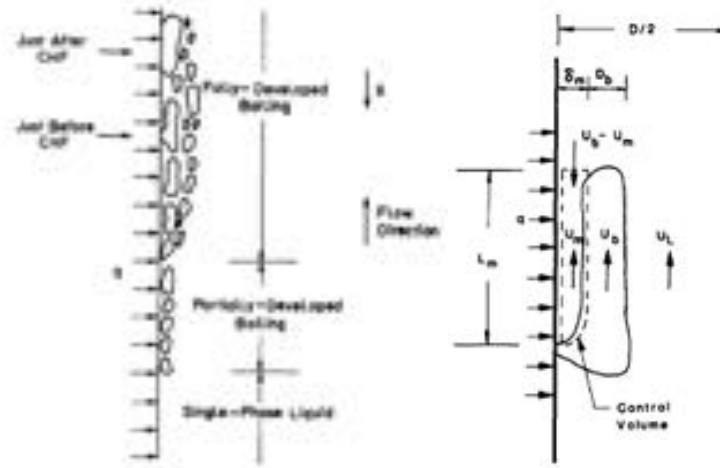


Fig. 11 – DNB CHF caused by the formation of a vapor blanket⁴²

II.C.3. Computational Techniques: Subchannel Analysis and CMFD

With the ever increasing computational power readily available to research and the complexity of multiphase phenomenon, computational methods have become the standard tool for any prediction method. Subchannel analysis has been an important tool for many years for understanding flow conditions within complicated geometries such as nuclear fuel bundles. As the name implies, the geometry under consideration is divided into either coolant or rod centered subchannels (Fig. 12) for which the thermal hydraulics are then determined. This analysis allows better thermalhydraulic behavior and CHF prediction than correlations alone that typically rely on bundle average properties. VIPRE and COBRA are two commonly used subchannel codes.

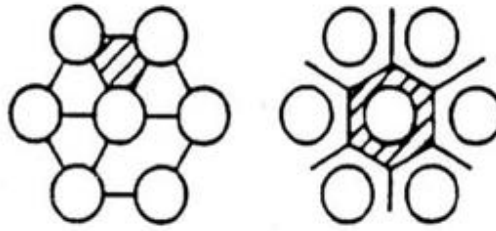


Fig. 12 – (Left) Channel centered and (Right) rod centered subchannels

A rapidly improving field of science is computational fluid dynamics (CFD) and with it, computational multiphase fluid dynamics (CMFD). Yadigaroglu argues that as CMFD improves, all the classical problems of predicting CHF will be overcome⁴⁴. However, there are significant hurdles yet to clear in direct CHF prediction with CMFD methods. Even so, CMFD is slowly making progress in tackling aspects of specific problems (e.g. mixing spacers) and will likely be a significant tool in the study and prediction of CHF in the future..

III. Experimental Facility

Given the great difficulty in accurately predicting the CHF for any unique condition (e.g. geometry, mass flux), it is not sufficient to rely on subchannel analysis, mechanistic models, or experimental correlations outside their range of applicability. SMRs are predicted to operate in just such a unique condition (i.e. moderate to high pressures and low mass fluxes). The University of Wisconsin – Madison High Pressure Critical Heat Flux Test Facility (UW-HPCHF - Fig. 13) was specifically designed to obtain CHF data at the unique operating conditions of these novel nuclear reactor designs.



Fig. 13 – (Left) Secondary Systems (includes TRIGA CHF Facility) and (Right) Primary Test Loop of HPCHF Facility

III.A. Facility Overview

The UW-HPCHF experimental facility is a vertical forced circulation loop, 2x2 equally spaced, non-uniformly heated square rod bundle. The facility is designed to operate ranges (Table II) associated with the low mass flux and high pressures prototypic of SMR designs. A summary of the primary dimensions of the test section and heater elements is summarized in Table III with detailed explanations included in section III.C.2.

Table II –Operating Range of HPCHF Facility

Parameter	Range
Pressure (MPa)	8.0 - 16.0
Mass Flux (kg/m ² s)	400 - 1200
Temperature (°C)	25 - 350

Table III – Summary of test section and heater element dimensions

Parameter	Ratio	Parameter	Size (cm)	Parameter	Size (cm ²)
$P_{\text{htr}}/D_{\text{htr}}$	1.33	D_{htr}	0.95	A_{test}	4.32
		P_{htr}	1.26		
$h_{\text{gap}}/G_{\text{gap}}$	0.75	G_{gap}	0.31		
		h_{gap}	0.23		
$q_{\text{peak}}/q_{\text{avg}}$	1.5	Width _{channel}	2.67		
		D_{hyd}	0.76		
		L_{HL}	200.00		

The components of the facility can be divided into two categories: Primary and Secondary Systems. The primary system consists of the high pressure/high temperature rated components, main heating elements/controls, and the primary heat removal system. Secondary systems are responsible for weight bearing, fulfilling auxiliary temperature control requirements, and data acquisition. Each of these systems is given a complete description in the sections that follow.

III.B. Design Guidelines and Goals

As mentioned in the introduction, the overall goal of the facility is to provide ‘validation data for an updated critical heat flux model for use in thermal-hydraulic computer code’ and improve ‘understanding of the CHF process... in a rod bundle geometry’ for SMR designs. In achieving the overall purpose of the facility, special considerations were given to the recording of key parameters (e.g. temperatures, flow rates, pressures) and permitting a flexible design for future experimental investigations (e.g. flow visualization, higher operating pressures/temperatures). These considerations are discussed in each section as appropriate and served as general guidelines in the overall facility design.

III.C. Primary System Details

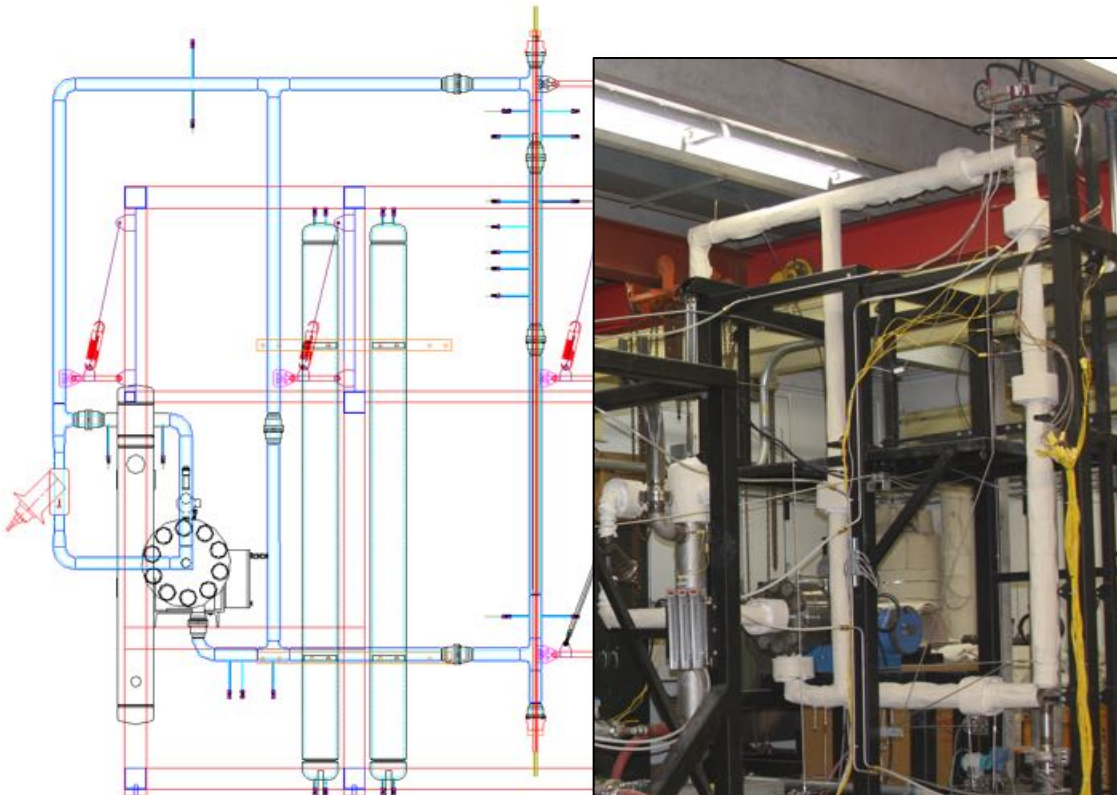


Fig. 14 – (Left) 2-D drawing and (Right) photo of the HPCHF primary system.

III.C.1. Main Loop Details

A simple process flow diagram and a 3-D model of the primary system are shown in Fig. 15. In reference to the process flow diagram, water from the high pressure variable speed pump (1) is diverted into two streams: one to the test section (2) fitted with a flow meter and one to a bypass (3) which mixes with the hot fluid exiting the test section. The ratio of the split is coarsely controlled with custom orifice plates with fine control obtained by a LabVIEW controlled inverter on the high-pressure pump.

The purpose of the test section bypass is to reduce the stream quality allowing for better control and predictability of heat transfer in the heat exchanger (5), pressure/level in the accumulator (7), etc. The mixed stream then enters the tube side of the heat exchanger and is then pumped back through the system. The bypass (6) for the heat exchanger allows for coarse control of the heat exchange necessary for the wide range of operating parameters and small thermal mass of water present in the loop (~26 L). Finer control of the heat exchanger is obtained via a variable speed pump on the shell side of the heat exchanger and throttle valve (neither one depicted). The shell side cooling consists of a water reservoir at near ambient pressure and temperatures (TRIGA tank) and an industrial glycol/water chiller system.

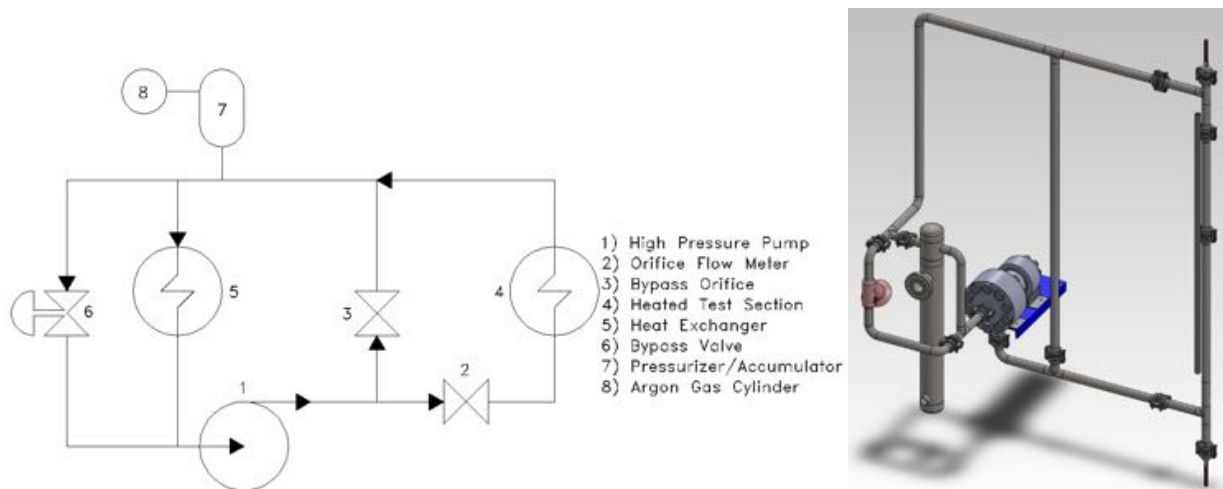


Fig. 15 – Basic process flow diagram and 3-D model (accumulator not shown) of the HPCHF facility

Two pressurizers (7) are used to control the operating pressure, dampen pressure oscillations, and serve as overflow reservoirs as the water is heated from ambient to test conditions. The volume of each pressurizer is approximately 43.5 L. Pressurization of the loop is accomplished via a compressed cover gas supplied by a ~41 MPa argon gas cylinder.

All primary process pressure piping and Grayloc fittings (2GR16) are SMLS 2 inch (5.08cm) NPS SS316 SCH 160 unless otherwise noted. Employed $\frac{1}{4}$ inch (0.635 cm) tubing is SS316 but the thickness varies and will be indicated in the appropriate section. All necessary design calculations prior to construction (e.g. heat transfer and pressure drop calculations) were performed jointly with Matthew De Angelis and are recorded in his Master's Thesis⁴⁵.

III.C.2. Test Section

The 'Test Section' as used in this document encompasses the vertical section of piping containing the full length (heated and unheated) of the heating elements. In reference to Fig. 15, and reproduced in Fig. 16, the test section starts at the 'tee' located at the bottom right of the 3-D model and continues to the other 'tee' at the top right of the 3-D model. There is a removable portion of the section built into the test section to provide flexibility for possible future experiments (e.g. viewing window) and contains all the bulk thermocouples but otherwise does not currently affect any other features of the test section. The entrance to the square channel is initiated by a square support plate welded to the inside of the piping, creating the transition from the inlet plenum (Fig. 16). Each aspect of the test section is discussed in detail below.

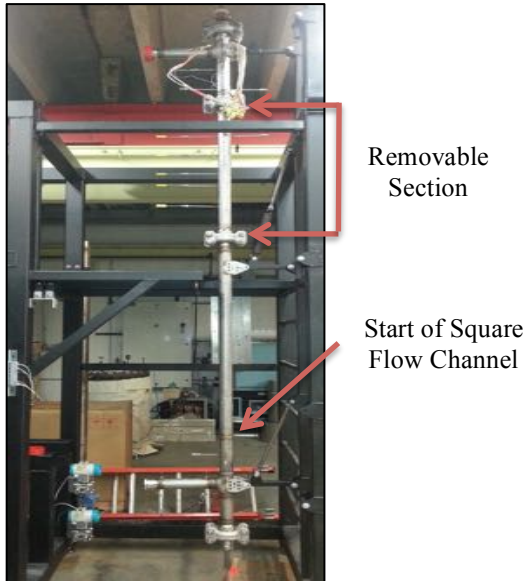


Fig. 16 – Test section of the HPCHF facility with removable portion and start of the square flow channel indicated.

III.C.2.a. Heater Elements

The HPCHF facility consists of a non-uniformly heated 2x2 rod bundle placed in a square flow channel to simulate a unit cell of a fuel assembly. These elements are electrically heated over a 2 m length with a prototypic axial chopped cosine power profile (100 kW max– 175.4 A/570 V max per element) with physical dimensions chosen to be representative of proposed SMR designs. Embedded within each rod are ten, stationary K type thermocouples spaced to maximize coverage of the most likely areas of CHF occurrence. The following discussion will elaborate on the heater element characteristics. The heater elements were manufactured by Stern Laboratories Inc.

Heater Element Details

Each heating element consists of several layers and materials as indicated in Fig. 17 with dimensions customized for the HPCHF facility (note dimensions shown are approximate). Key features include the Inconel 718 resistance filament and Monel K500 cladding. The filament is a fully annealed seamless tube with a nominal wall thickness of 0.51 mm. The tube was helically cut with varying pitch

(thinnest in the middle and thicker at the ends) to provide the desired axial power profile via the associated change in electrical resistivity. The filament is electrically isolated from the cladding with boron nitride insulation (both within the filament tube and its periphery) and then welded to 50 mm nickel transitions which are then welded to the copper leads. The cladding is annealed Monel K500 seamless tubing with a nominal wall thickness of 0.38 mm and diameter of $0.95 \text{ cm} \pm 0.05 \text{ mm}$.

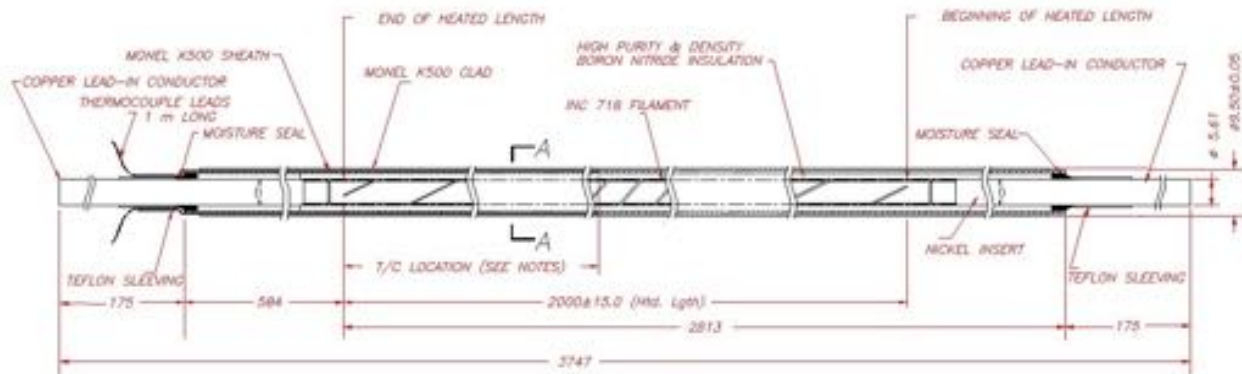


Fig. 17 – Detailed drawing of heater elements (in mm) as provided by Stern Laboratories⁴⁶.

Power System

Each heater element copper lead connects via insulated copper cables within conduit piping to a Silicon-Controlled Rectifier (SCR model Fusion-DC-2-5550-0-0000-0000 – one per heater element) which transforms the AC building supply to a user specified variable DC power.

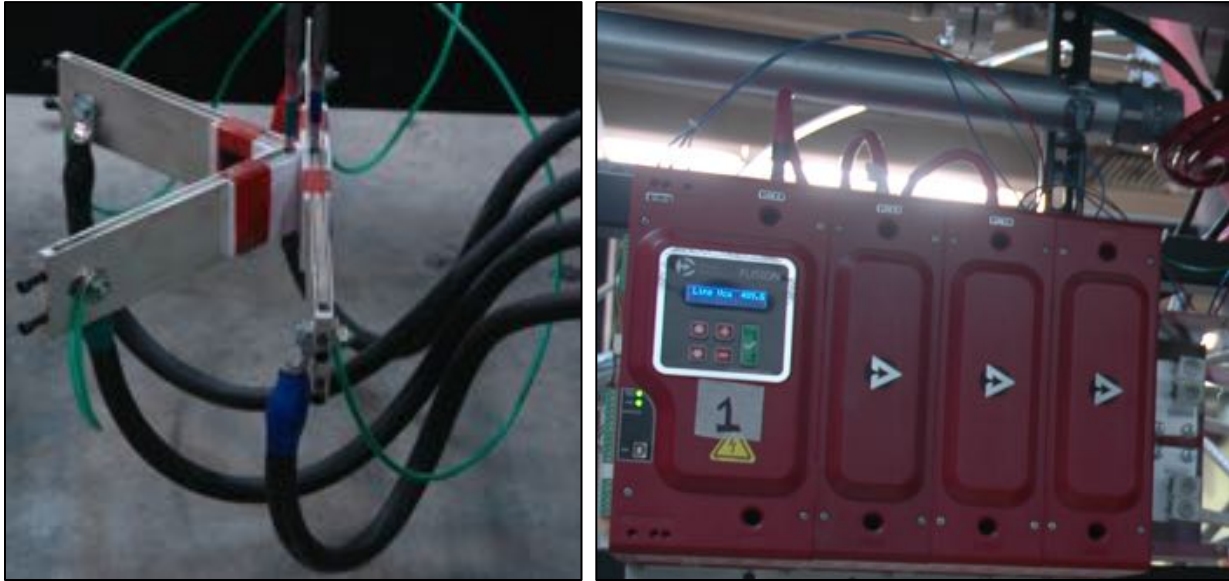


Fig. 18 – (Left) Lower end of copper leads connecting to power cables (green wires for ground reference). (Right) Each cable leads to a SCR via conduit piping (top silver pipe) and attach on right of SCR. Top wires are AC power cables.

Heater Element Pressure Boundary

The use of copper leads required specialized fittings that would permit the heater elements to be removed easily from the test section and be able to withstand the demanding conditions of the experiments, including thermal expansion of the heater elements. For this purpose, Stern Laboratories modified SS316 2GR14 blind hubs with threaded packing seals/O-ring seals and provided custom cooling blocks. Two separate hub designs, capable of sealing the facility to above 25 MPa, are used: a fixed threaded hub at the top and a sliding O-ring seal on the bottom. While both boundaries are required to stay below 200°C based on protecting the moisture seals of the heater rods, the pressure boundaries failure is tied to other temperature limits.

The top hub contains a graphite lubricant used in the threaded packing seal which limits the hub temperature to ‘much higher than 200°C’ as it uses a graphite sealant. If raised significantly above 200°C the lubricant will begin to burn off. While the graphite sealant temperature limit could potentially be exceeded safely if needed, the temperature limit of the moisture seal (200°C) must not be exceeded.

Therefore a copper cooling block is positioned directly upon the threaded seals to efficiently regulate the temperature and keep the hub and moisture seals well below their operational limits. A thermocouple attached to the hub near the packing seals monitors the temperature.

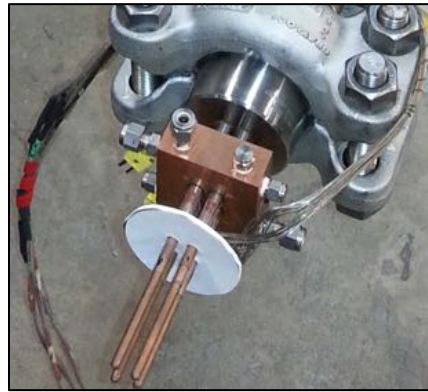


Fig. 19 – Modified top hub with installed copper cooling block. The moisture seal can be seen between the white disc and cooling block and a portion of the threaded packing seal is visible between the cooling block and the Grayloc hub.

In addition to the moisture seals on both rod ends, the O-rings on the lower hub are also required to stay below a temperature of $\sim 200^{\circ}\text{C}$. However, as the O-rings are located directly in the hub, the cooling block for the bottom hub is compressed onto the modified hub thereby providing efficient heat transfer. This allows to the coolant to be as close as possible to the O-ring while maintaining a sliding seal for thermal expansion. Additional O-rings are located within the cooling block as well to provide the water tight seal at that location as well. However, even with the cooling block, it was theorized that, due to the proximity of the O-rings to the rapidly moving hot test fluid, the cooling block may not be sufficient. Therefore, a buffer zone of approximately 15 cm was inserted between the lower tee and the bottom hub to decrease convective heat transfer by further isolating the O-rings. Similar to the top hub, a thermocouple placed close to the O-rings monitors the hub's temperature.

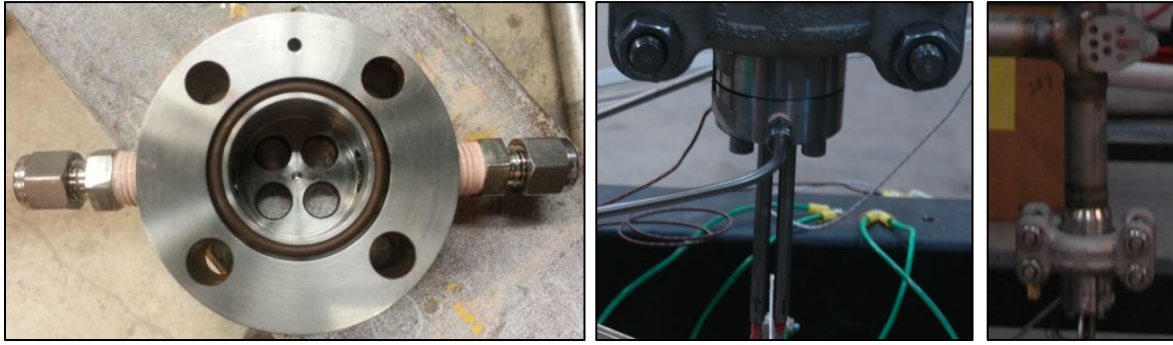


Fig. 20 – (Left) Bottom hub cooling block. (Middle) Modified bottom hub and cooling block. (Right) 15 cm standoff.

Power Profile

The nondimensional power profile ($q(x)/q_{avg}$) of the heater elements is defined by Equation (3) where x is the axial location of interest and L_{HL} is the total heated length (i.e. 2 m for these heaters). Fig. 21 is the graphical representation of the profile. The peak to average power ratio (q_{peak}/q_{avg}) is 1.5.

$$\frac{q(x)}{q_{avg}} = \theta_0 + \theta_1 \cos \left(2\theta_2 \left[\frac{x}{L_{HL}} - 0.5 \right] \right) \quad (3)$$

Given: $\theta_0 = 0.8187458177$; $\theta_1 = 0.6812541823$; $\theta_2 = 2.436354311$

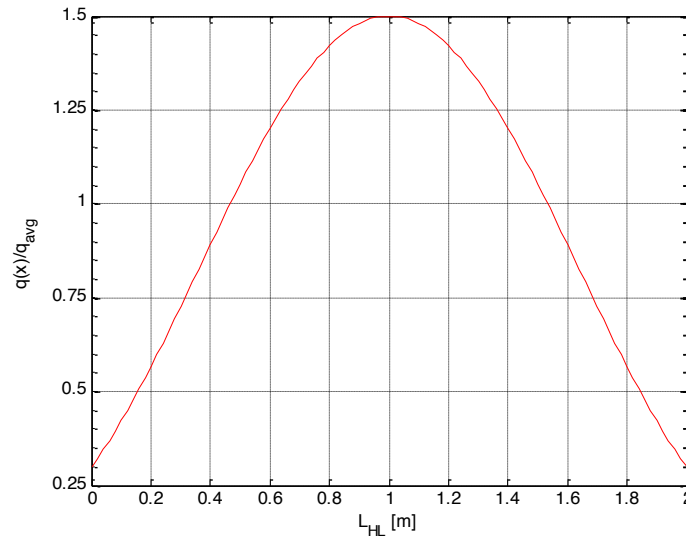


Fig. 21 – Power profile of non-uniform heater elements as a function of heated length

Thermocouples for CHF Detection

Within each heating element are ten ANSI Type K, ungrounded thermocouples (TC) embedded in grooves cut into the Monel sheath⁴⁶. The thermocouples are placed at various axial and circumferential locations (Table IV) to maximize the coverage of the regions of the flow channel in which CHF is most likely to occur while avoiding direct coverage by grid spacers. Based on maximizing coverage of potential CHF locations, two different heater element ‘types’ (Type 1 and 2) with different thermocouple circumferential orientations, but otherwise identical (i.e. power profile, axial thermocouple location, etc.), were constructed.

Table IV – Thermocouple axial location from beginning of the heated length and circumferential location (0° is TC #9 for Type 1 and TC #3 for Type 2 from the orientations shown in Fig. 22) of the two types of heater elements

Type 1 Heater Element	Thermocouple #	1	2	3	4	5	6	7	8	9	10
	Distance from Beginning of HL (cm)	96.2	103.8	133.4	133.4	146.2	146.2	153.8	177.8	177.8	197.5
	Circumferential Location (°)	90°	30°	120°	225°	150°	270°	60°	180°	0°	315°
Type 2 Heater Element	Thermocouple #	1	2	3	4	5	6	7	8	9	10
	Distance from Beginning of HL (cm)	96.2	103.8	133.4	146.2	133.4	146.2	153.8	177.8	177.8	197.5
	Circumferential Location (°)	300°	45°	0°	90°	180°	270°	210°	330°	135°	240°

Additional views of the axial and circumferential thermocouple locations are shown in Fig. 22 and Fig. 23. Note that any given thermocouple number can be referenced between the two figures and the power profile to understand where exactly in the channel the thermocouple is located. Any reference to a heater and thermocouple number in this paper will be referenced to the locations specified by these two figures.

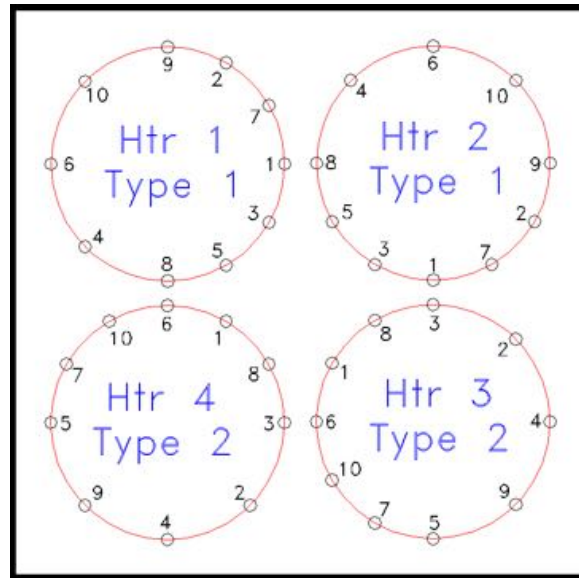


Fig. 22 – TC orientation of each heater element type, heater number reference used in paper, and heater element locations.

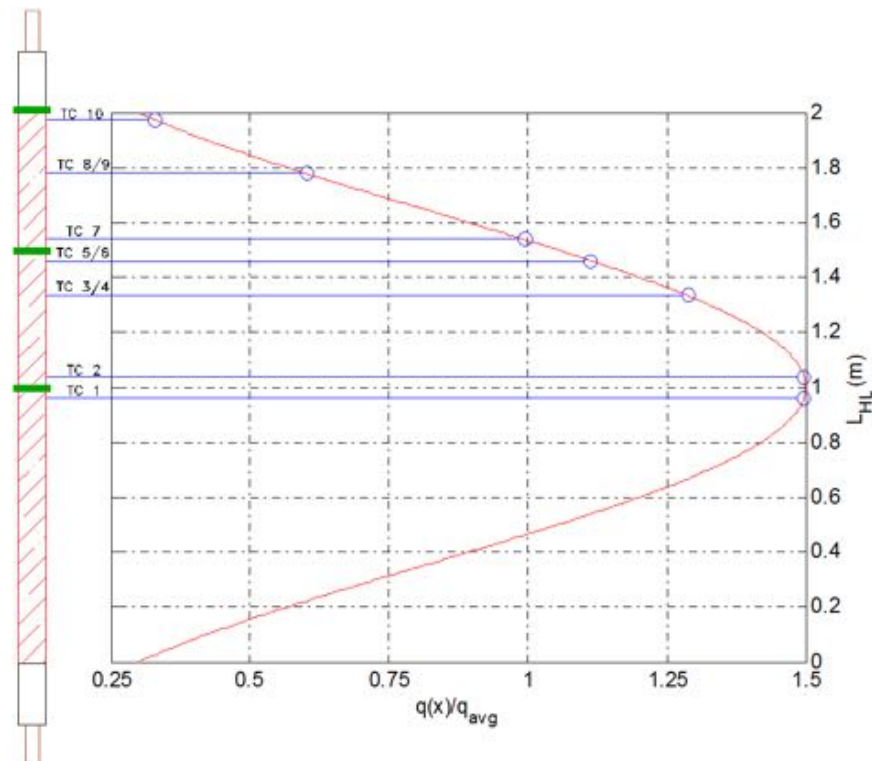


Fig. 23 – Chopped cosine power profile and associated axial thermocouple location on each heater element. Green markers indicate possible location of a grid spacer.

The number of embedded thermocouples was limited to ten along with a minimum circumferential spacing of 30° due to rod fabrication considerations. It is noted that sliding TCs have been shown to be better options to accurately detect the initial CHF location but this was not an available option.

III.C.2.b. Inlet Plenum

Before entering the heated portion of the test section, the flow turns 90° from a horizontal to a vertical flow and passes through a ‘plenum’. The purpose of the plenum is to stabilize the flow so upon entering the square channel the flow is evenly distributed in order to avoid any biased flow effects on the CHF. Determination of the inner diameter and length of the plenum necessary to accomplish this goal required the use of a computational fluid dynamics package (CFD). In this study ANSYS FLUENT was used for all CFD applications. Convergence was determined based on the agreement between solutions and arrival at an asymptotic limit for the residuals between various iteration lengths. Additionally, the coarseness of the mesh was varied to further validate the solutions.

Plenum Type

Fig. 24 is a visual representation of the evaluation of four plenum candidates with the transition to the square channel indicated. The color shift from dark blue to red indicates increasing fluid velocity. Initially two different plenums were evaluated: a straight section of pipe (A) and a 12.2 cm inner diameter (ID) plenum directly connected to the tee joint (B). The behavior of the flow preferentially passing on the far side of the inlet in the large plenum led to an expansion to two more plenum options: a 12.2 cm ID plenum (C) and an 8.5 cm ID plenum (D) each with a 7.62 cm straight section to suppress the flow behavior noted. As shown, the larger the plenum, the more static the flow behavior. Also, the straight section improves the behavior by impeding reducing the momentum of the fluid as it races through the tee. A smaller plenum appears to approach the solution of the straight section as would be expected. As

these four plenums predict the range of feasible designs, the outlet condition of each model was then compared to determine the most appropriate choice.

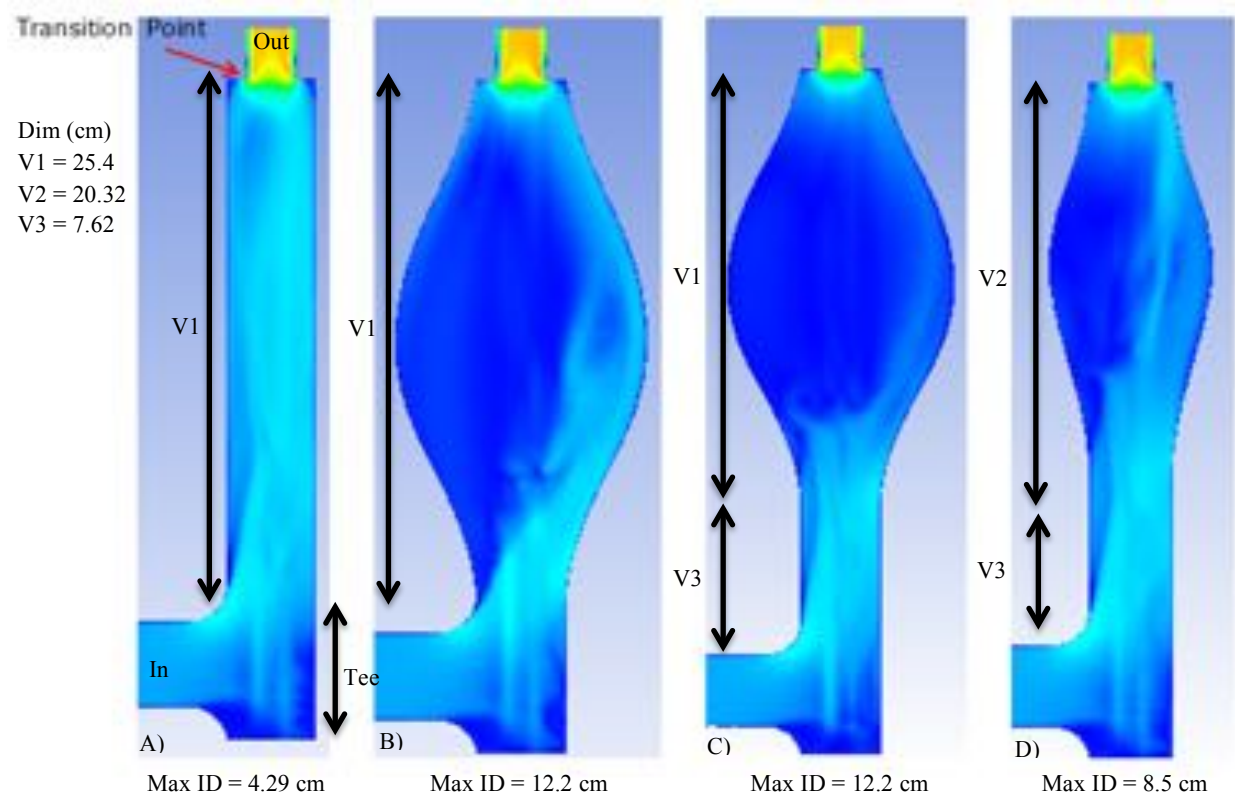


Fig. 24 – Visual comparison of the flow into the first 2.54 cm of the square channel for four inlet plenum options. The outline of the heater elements can be seen in the lower portion of each figure. Vertical and inner diameter dimensions are given for reference as images are not scaled the same. Inlet (In), tee section (Tee) and outlet (Out) have the same dimensions. Velocity color scheme is identical across all figures.

Evaluation of the plenums was performed by comparison of the cross sectional velocities at the point of transition and 2.54 cm after the transition (Fig. 25 and Table V). By inspection, the velocity contour maps across each plenum option are nearly identical at each elevation and show a similar increase in velocity in the middle channel at the 2.54 cm mark. Furthermore, the cross sectional data shown in Table V further quantify the behavior observed in the contour maps. This behavior is believed to be due to the severe restriction (63% reduction in flow area as compared to the straight section with rods).

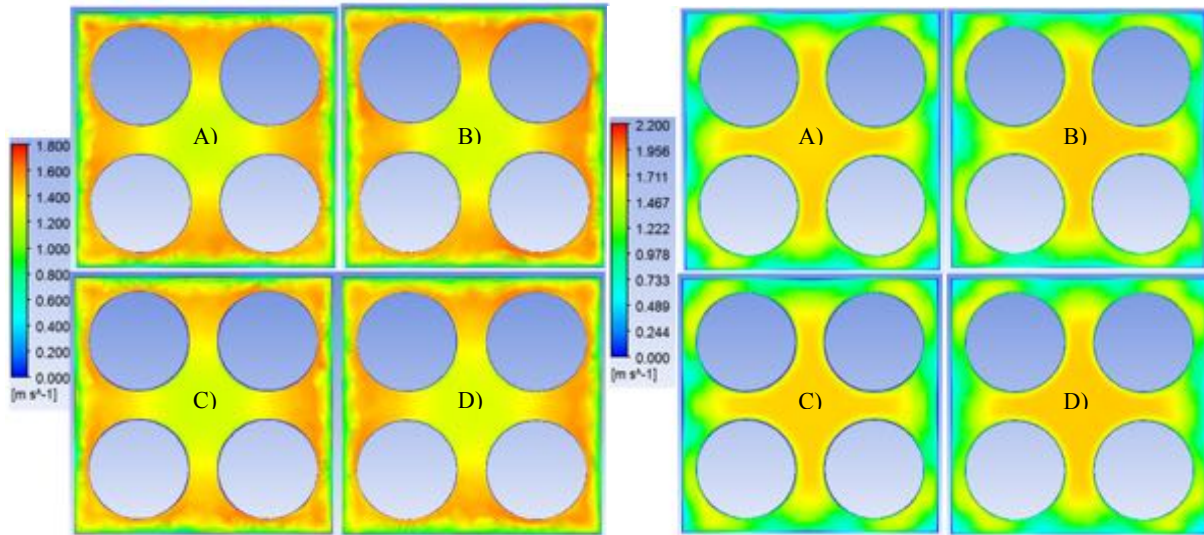


Fig. 25 – Velocity contour plot of each plenum in Fig. 24 at (Left) the transition and (Right) 2.54 cm after the transition.

The restriction into the square channel is hypothesized to act as the dominating force of the velocity behavior observed. This explanation apparently describes the slight variations among the modeled plenums. Therefore, based on this analysis, the straight plenum type was chosen as the best option to apply to the facility.

Table V – Outlet cross sectional plenum velocity data (m/s)

Plenum	At Transition				2.54 cm After Transition			
	Max	Min	Mean	σ	Max	Min	Mean	σ
A	1.79	0.31	1.20	0.37	1.96	0.06	1.44	0.39
B	1.80	0.28	1.21	0.35	2.08	0.07	1.46	0.39
C	1.78	0.35	1.18	0.58	2.05	0.06	1.44	0.44
D	1.80	0.29	1.09	0.37	1.96	0.04	1.45	0.40

Plenum Length

A possible breakdown in the velocity behavior observed among the plenum types was believed to be possible if the straight section before the transition became too short. As the straight section was shortened, the momentum of the fluid passing the tee would preferentially impact the square channel and

adversely affect the uniformity of the velocity distribution. The necessary plenum length was therefore investigated in a similar manner as the plenum type; adapting the length of the pipe between the tee and the square channel and observing the change on velocity data until an acceptable minimum length was determined. Fig. 26 shows contour maps of three scenarios: 1) a 25.4 cm length 2) a 15.2 cm length and 3) a 2.54 cm length. The effect of the straight section being too close to the tee is clearly noted in scenario 3 by the curve of the velocity field in the channel. This behavior diminished and disappeared as the straight length was increased.

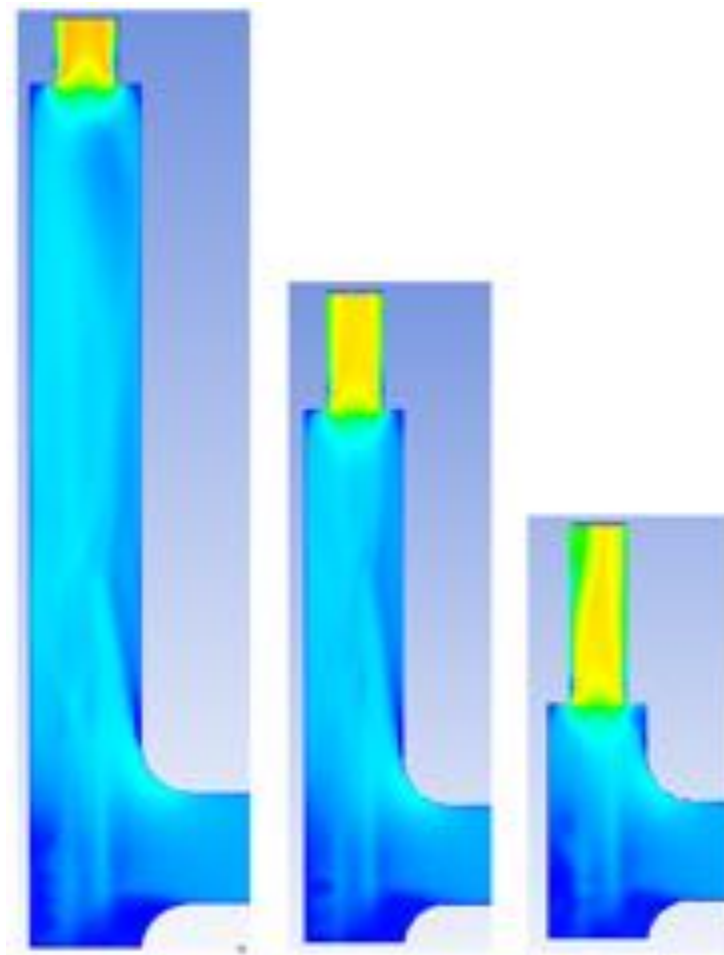


Fig. 26 – Velocity contour plots of a straight plenum of 1) 25.4 cm, 2) 15.2 cm, and 3) 2.54 cm

From this analysis it was determined that a minimum length of approximately 15 cm was required to avoid deleterious impacts on the outlet behavior of the plenum. The actual straight length used in

construction was 20.32 cm and was determined from the minimum length required and other fixed constraints unique to the heater elements and location of the facility.

III.C.2.c. Square Flow Channel

$h_{\text{gap}}/G_{\text{gap}}$ Ratio

The geometry arrangement applied to the HPCHF is a square channel housing the heater elements through which the coolant is conveyed. The width of the square channel was determined based on the ratio of the element to wall gap (h_{gap}) and of the gap between heating elements (G_{gap} – fixed based on heater pitch). To simulate a small rod bundle within a larger bundle, the ratio was limited between 0.5 and 1.0 as these constitute an h_{gap} length of half to a full G_{gap} distance. The ideal h_{gap} was determined to minimize $h_{\text{gap}}/G_{\text{gap}}$ ratio while preventing a preferential CHF event on the outer periphery of the heating elements. Additionally, the h_{gap} chosen needed to allow the physical channel to fit into the round pipe forming the pressure boundary.

CFD simulations provided insight to an appropriate compromise to the competing bounds specified previously. Fig. 27 demonstrates the representative temperature contours of various gap ratio simulations. Based on these simulations it was determined that the a ratio of 0.75 would best satisfy all bounding requirements while still erring slightly towards the CHF occurrence on the inner channel given that the outer wall in practice will slightly lower the wall temperature as compared to the simulations which assumes an adiabatic wall condition. The chosen ratio was additionally supported by similar ratios used in peer reviewed literature^{47,48,49,50,51}. Table VI summarizes the resulting dimensions of the square channel from this evaluation.

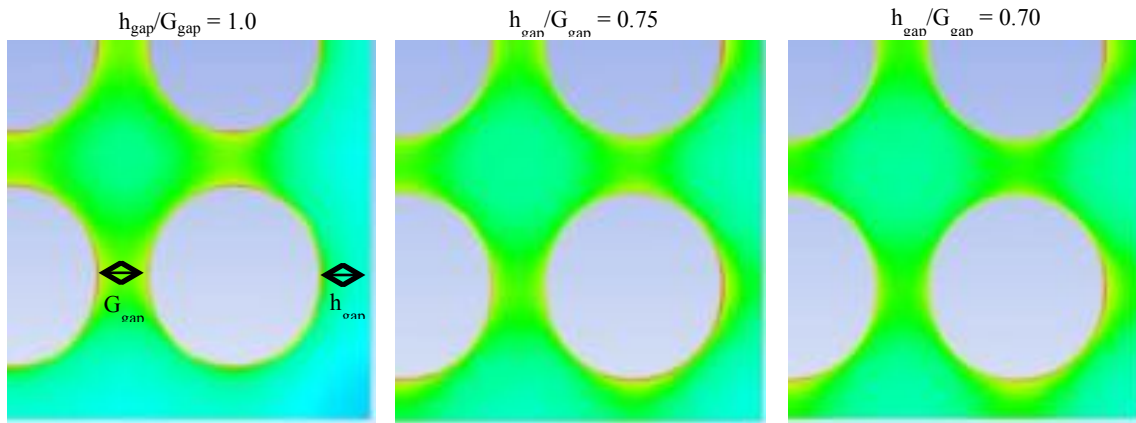


Fig. 27 – Temperature contours capturing the transition (left to right) of preferential heat distribution from between the heating elements to between the heating elements and wall based on $h_{\text{gap}}/G_{\text{gap}}$ ratio

Table VI – Summary of Square Channel Geometry Parameters

Parameter	Ratio	Parameter	Size (cm)
$P_{\text{htr}}/D_{\text{htr}}$	1.33	D_{htr}	0.95
		P_{htr}	1.26
$h_{\text{gap}}/G_{\text{gap}}$	0.75	G_{gap}	0.31
		h_{gap}	0.23
		$\text{Width}_{\text{channel}}$	2.67

Square Support Plate

The initiation (or transition point) of the flow channel is created by a support plate made of two laser cut SS316 pieces welded together and then welded into the round pressure piping to form a platform and create a seal to force the flow to enter the channel (Fig. 28). The plate is designed support the weight of, and secure in place, the channel and limit appreciable amounts of flow from entering the regions outside of the channel.

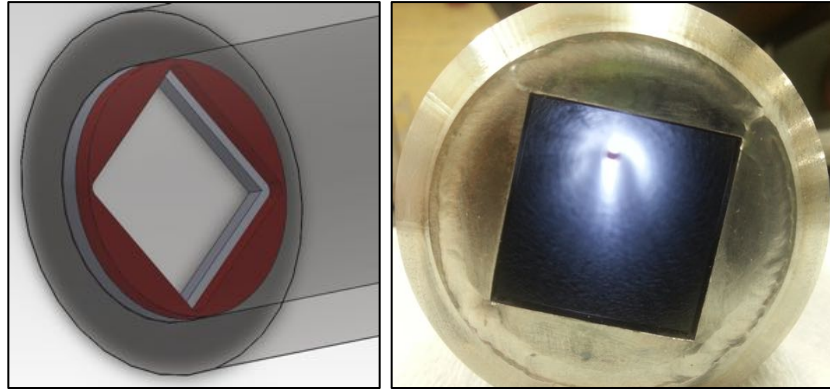


Fig. 28 – (Left) 3-D internal view of the support plate. (Right) Actual support place welded in place.

Square Channel

The square channel is made of four laser cut SS316 lengths cut into two types of mating connections (Fig. 29). The four pieces are tack welded approximately every 7-15 centimeters and the outside corner edge and one end are slightly ground to create a tight fit into the round piping and support plate which serves as the entrance or transition into the square channel (Fig. 30 and Fig. 30). The tightness of the fit into the pipe precludes any need for additional structural support of the channel. Additionally, eight holes just large enough for 0.125" thermocouples have been drilled through the channel at the points specified in section III.C.2.g to allow access to bulk temperature fluid measurements. The channel (including the support plate) is designed to provide approximately 7 cm of channel length before the start of the heated length and continue for approximately 10 cm after the end of the heated length.

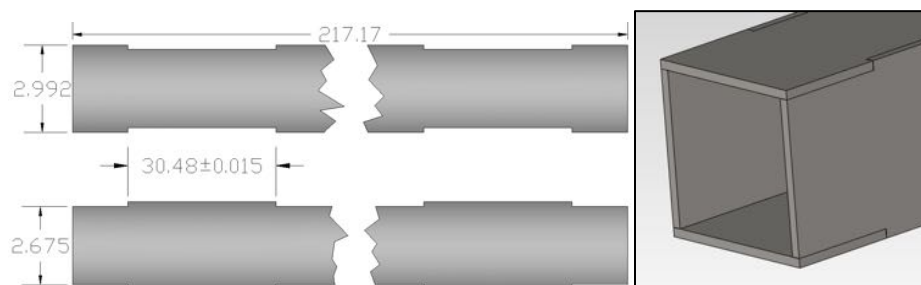


Fig. 29 – SS316 channel pieces (thickness of 0.3175 cm) comprising the square flow channel. Dimensions are in cm.

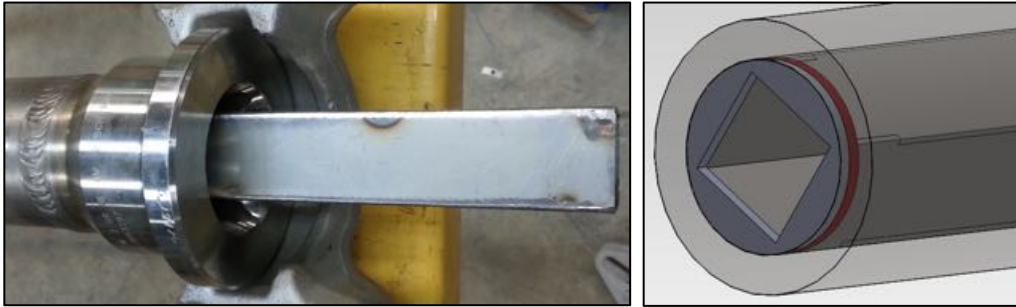


Fig. 30 – (Left) Top end of square channel inserted into piping (Right) 3-D view of channel inserted into square plate.

III.C.2.d. Grid Spacers

Although it is recognized that obstacles in the flow channel, such as grid spacers, can have a significant enhancement effect on the CHF, due to concerns that boiling and flow induced vibrations will cause the rather flexible heating elements to make contact and significantly alter the geometry, custom grid spacers have been applied at locations corresponding to 50%, 75% and 100% of the heated length (Fig. 23). In order to minimize the potential effect of the spacers, they were designed as to minimize flow blockage. The design used in the experiment is shown in Fig. 31 and yields a 16% flow blockage over a length of 2.54 cm per spacer. The spacers are 2.54 cm long, 2.49 cm wide and 0.048 cm thick. These spacers do not have any mixing vanes, only tabs to spring on the element surface to prevent slippage.



Fig. 31 – Custom grid spacers used in HPCHF facility. (Right) Installed grid spacer on actual heater elements.

III.C.2.e. Test Pressure Measurements

Gauge Pressure

The pressure of a specific test, as referenced throughout this document, is determined from a gauge pressure measurement (Omega PX409-5.0KGI) taken 10 cm from the transition point to the square channel and then corrected to absolute pressure.

Differential Pressure

The differential pressure (dP) across the test section is measured (Siemens 7MF4533-1FA32-1NC6-Z+AO2B21) between 10 cm before the transition point to the square channel and 10 cm after the square channel is terminated. The range of the transmitter is 16.3-1630 cm of H₂O.

III.C.2.f. Test Flowrate Measurement

Due to the high design pressure and temperatures, a commercial flow meter was not available. Therefore the mass flowrate through the test section was measured with a custom orifice flow meter designed based on the ASME⁵² standards for sizing, up/downstream straight length requirements, etc. The flow meter comprises a differential pressure transmitter (Siemens 7MF4533-1FA32-1NC6-Z+AO2B21) with pressure taps at equal spacing (2.7 cm) on either side of the midpoint of an interchangeable custom orifice plate machined to ASME specification from a blind Grayloc seal ring.

Two orifices were created for these experiments, both of which were calibrated at 0.1 MPa and 20°C to determine their discharge coefficient (C_d) by measuring the pressure drop ($\Delta P_{\text{orifice}}$) through the test section with a vortex flow meter temporarily installed in the line at 0.1 MPa and 20°C. Mass flowrate (\dot{m}) was determined from the pressure drop data using equation (2). ρ is the density of the fluid, A_{orifice} is the cross sectional area of the orifice, β is the ratio of the diameter of the orifice and the diameter of the pipe. Fig. 32 shows a graphical comparison of experimental data and the correlation both scaled from the

calibration conditions to representative test conditions. Uncertainty analysis of the flow meter is discussed in section IV.F. The determined coefficients and other pertinent information are summarized in Table VII.

$$\dot{m} = \rho A_{orifice} C_d \sqrt{\frac{2\Delta P_{orifice}}{\rho(1 - \beta^4)}} \quad (4)$$

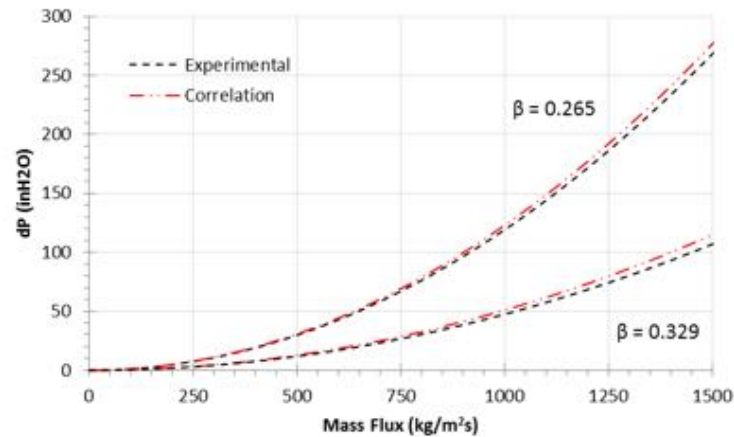


Fig. 32 – Comparison of predicted pressure drop from ASME correlation to calibration data of the orifice flow meter scaled to water at 275°C and 12.8 MPa.

Table VII – Custom orifice plate dimensions and regressed C_d

Orifice	D (cm)	β	C_d	+/-
Small	1.143	0.265	0.62	0.01
Big	1.422	0.329	0.63	0.01

III.C.2.g. Bulk Temperature Measurement

Inlet/Outlet

Both the inlet and outlet temperatures are measured 10 cm before and after square flow channel with Resistance Temperature Detectors (RTD – Omega PR-11-2-100-1/8-10-E-OTP). The inlet temperature referenced throughout the document is this temperature probe at the above specified location.

Bulk Test Section

Within the test section are eight ungrounded Type K thermocouples at five different axial locations. A thermocouple enters into the square channel through predrilled holes at the locations specified in Table VIII and Fig. 33.

Table VIII – Bulk thermocouple axial location

Bulk Thermocouple #	1	2	3	4	5-8
Distance from Beginning of HL (cm)	133.4	146.2	153.8	165.8	177.8

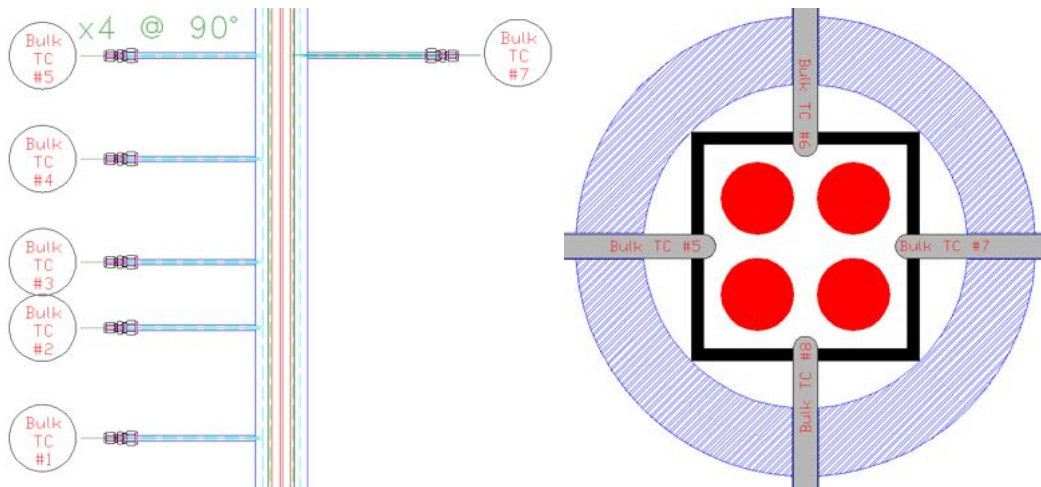


Fig. 33 – (Left) Schematic of axial bulk TC position. (Right) Bulk TCs 5-8 distribution with representation of minimal entrance into flow channel.

Each thermocouple protrudes into the outside portion of the flow channel just enough to capture the fluid temperature while limiting wall effects (Fig. 33). Thermocouples 5-8 are located at the same axial position in order to better understand any discrepancies in flow/temperature distribution. Ideally these four thermocouples should have identical responses (i.e. within their inherent error limits) while consistent, significant deviations may indicate non-uniformity in the flow channels.

III.C.3. High Pressure Heat Exchanger

Heat Exchanger

The primary heat exchange mechanism is a custom designed and built shell and tube heat exchanger⁴⁵ consisting of fifteen tubes (high pressure) and designed for low temperature/pressure water as the shell side coolant. Fig. 34 displays photos of the exchanger under construction and installed in the facility. The maximum rating of the exchanger is 25 MPa at 540°C and constructed of SS316. Inlet and outlet temperature of both the shell and tube side of the exchanger are monitored with 0.125" ungrounded Type K TCs.



Fig. 34 – (Counter Clockwise from Top Left) Pressure tubes and support/mixing baffles, tube sheet, high pressure inlet/outlet, installed heat exchanger with bypass valve.

Bypass Valve

In order to provide rough control of the heat exchanger given the wide operation parameters, a linear response bypass valve⁴⁵ was incorporated into the design of the heat exchanger (Fig. 35). This valve is a limiting factor of the pressure/temperature rating limit of the facility being rated to 25 MPa at

50°C or approximately 20 MPa at 350°C. Although current CHF experiments are well below this limit, the valve design is such that it can be removed and replaced with an orifice seal ring if required future experiments operating conditions.



Fig. 35 – Installed primary heat exchanger bypass valve.

III.C.4. High Pressure Pump

The primary loop pump is a Chempump canned motor (model GCT-5k 36I) (Fig. 36) capable of operating at super critical water (SCW) conditions up to 25 MPa at 593°C and constructed with Inconel (ASTM B564, UNS N06600). It is powered and controlled with a frequency inverter (Danfoss VLT5011PT2C20STR3DLF00A00C0) through LabVIEW. As the motor itself is temperature limited, the pump has its own heat exchanger. For reference, the pump curve of this motor is presented in Fig. 37. Additional pump information is located in Appendix A.



Fig. 36 – HPCHF Facility primary loop pump

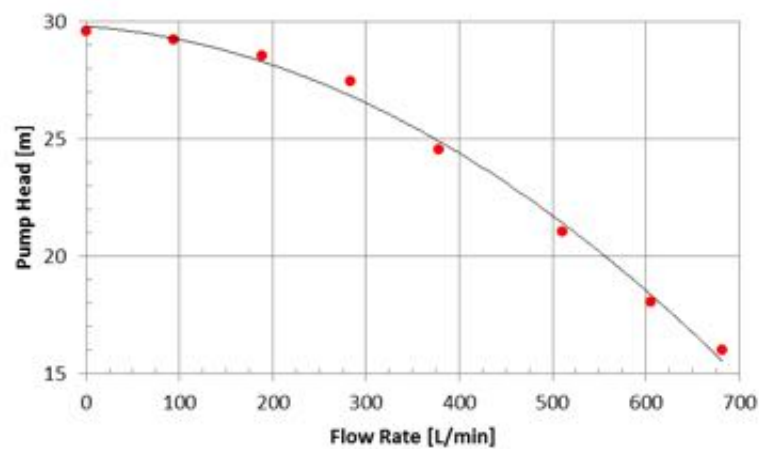


Fig. 37 – HPCHF Facility primary loop pump curve

III.C.5. Test Bypass Section

In reference to Fig. 14 and Fig. 15, the test loop incorporates a bypass of the test section. This bypass section consists of a simple pipe with one of the two orifice plates designed for flow measurement located at the Grayloc connection. This orifice increases the pressure drop of the bypass in order to allow

an approximate flowrate twice that of the test section. The orifice is required as the bypass pressure drop would otherwise be too small (i.e. flowrate in bypass would be too large) for the pump to be able to achieve the necessary flowrates in the test section. This bypass improves controllability of the experiment providing additional thermal mass, limits sections of pipe under a two-phase condition, decreases temperature gradient across heat exchanger, etc.

III.C.6. Pressurization System

Pressurization of the facility is performed via application of a compressed argon cover gas from a ~41 MPa cylinder over water in two partially filled 43.5 L tanks. References to the tanks may include the nomenclature of pressurization/expansion tanks, pressurizer, and/or accumulator. The pressurization tanks, connected in parallel, lead back to the facility through a concentric tube heat exchanger and connect at the top of the facility after the mixing tee described in section III.C.1. A depiction of the general features of the system is shown in Fig. 38. All fittings used are ¼ inch (0.635 cm) or ½ inch (1.27 cm) Swagelok SS316 fittings with the exception of an HIP fitting (20-LM4-6 and 20-21LF4-C) connecting the ¼ inch (0.635 cm) tube at the top of the test loop. This fitting provides extra safety given the extensive thermal cycling of this section being so close to the test loop.

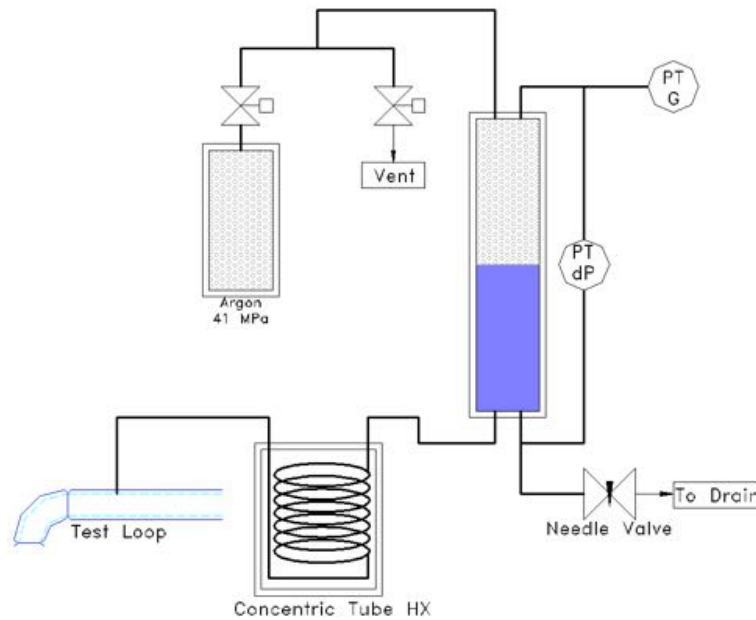


Fig. 38 – Simple diagram of the pressurization/thermal expansion system.

Pressurization Tanks

Each of the two tanks (Fig. 39) are 6 inch (15.24 cm) NPS SS316 SCH 80 and designed to operate with a water level of approximately 25-50% of their total volume. Details of their performance during an experiment can be found in section IV. The tanks are rated at 18 MPa at 204°C. This rating is well within the range of experimental tests performed given adequate cooling to the line passing through the concentric tube heat exchanger. However, if experiments outside this rating are performed these tanks require replacement.

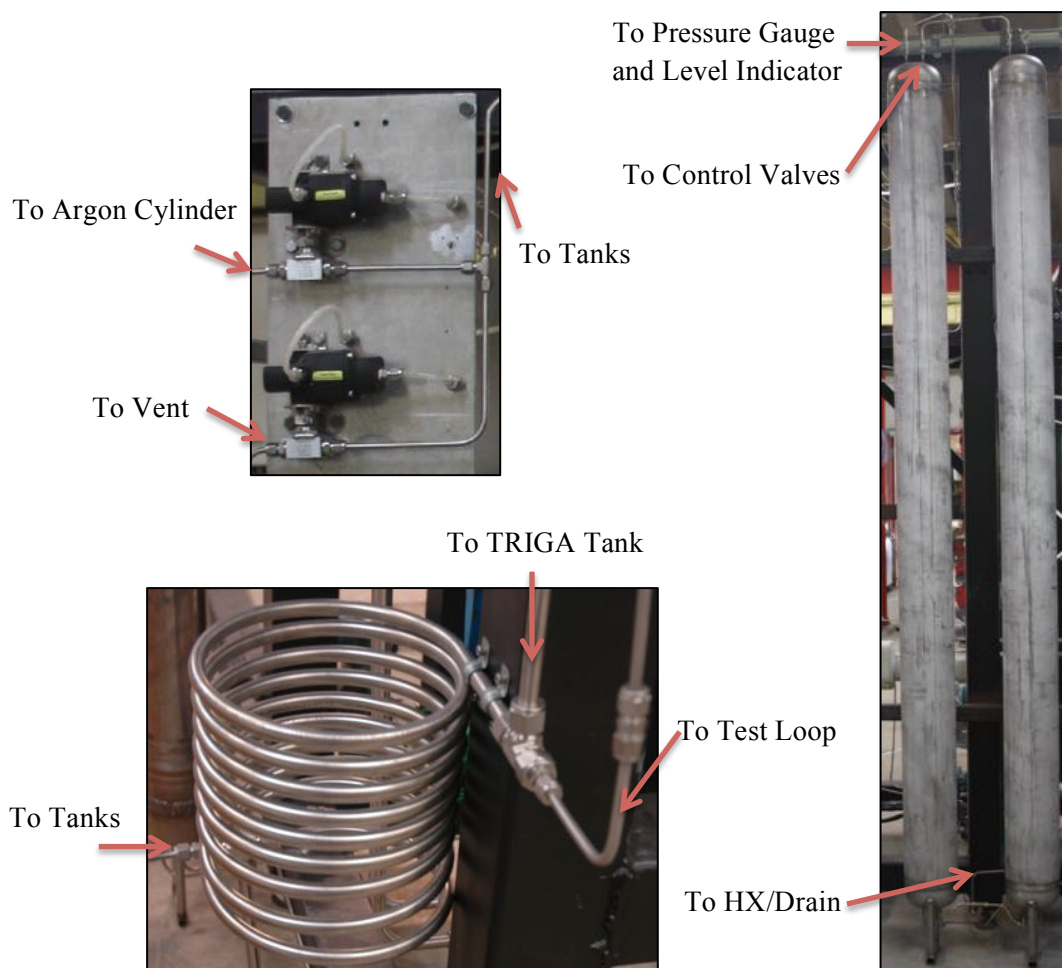


Fig. 39 – (Clockwise from top left) Pneumatic control valves, pressurization tanks, concentric tube heat exchanger.

Pressure Control

The gauge pressure of the tanks is monitored by a single Omega pressure transmitter (PX309-5KGI). The pressure of the tanks, and thereby the whole system, is varied via two pneumatically controlled spring actuator (Swagelok MS-131-SR) on a $\frac{1}{4}$ inch (0.635 cm) ball valve (Swagelok SS-4SKPS4), both in a normally closed position (Fig. 39). One of the actuators leads to the argon cylinder while the other depressurizes the system by venting to the atmosphere. Each actuator is controlled manually via LabVIEW using a 3 way 2 position valve (Grainger 4HN47). Additional control of the

pressure is available by removing water from the system during an experiment via use of a needle valve (Swagelok SS-4GUF4-G) leading to the drain.

Gauge and Level Indicator

The water level within the tanks is monitored using a single 0-250 mbar Rosemount differential pressure (dP) transmitter (3051CD2A22A1AM5DFE5L4Q4). This is possible because the tanks are connected in parallel. Truly, the transmitter measures the differential pressure between a tube filled with water to the same height of the tanks and the pressure from the unknown height of fluid. The result is the approximate height of the argon cover gas from which the level of the water can be backed out by simple subtraction.

Concentric Tube Heat Exchanger

Given the proximity of the rating to the limits of the experiments and the increased hazard of having unnecessary hot, pressurized lines, it was advantageous to cool the connecting line between the primary test loop and the pressurization tanks. The heat exchanger is created from a SMLS $\frac{1}{4}$ inch (0.635 cm) OD 0.065 inch (1.65 mm) wall SS316 tube (high pressure) and a SMLS $\frac{1}{2}$ inch (1.27 cm) OD 0.035 inch (0.89 mm) wall SS316 tube both initially 6 m in length. To construct the heat exchanger, the $\frac{1}{4}$ inch (0.635 cm) tube is fed completely through the $\frac{1}{2}$ inch (1.27 cm) tube, swaged on one end, and then the two tubes are turned slowly in a lathe to coil the tubes together. Once coiled, any slack of the $\frac{1}{4}$ inch (0.635 cm) tube was pulled through and then the two tubes were swaged in the exact same manner as the other end. Fig. 39 shows the heat exchanger and a swaged end and the $\frac{1}{4}$ inch (0.635 cm) tube leading to another fitting that leads to the primary test loop.

III.C.7. Emergency Pressure Relief System

In case of a system over-pressurization event, an adjustable, spring loaded Swagelok pressure relief valve (SS-4R3A1) was incorporated into the facility to quickly lower the system pressure to safe limits. For the experiment performed the valve was set to release at 22 MPa.

III.D. Secondary Systems Details

The secondary systems are those systems which could be changed with alternative systems without any direct effect on CHF experiments in the facility. Included in this category are all secondary heat exchange systems, weight bearing structures, and data acquisition systems.

III.D.1. Main Supporting Structure

The supporting structure for the primary test loop (Fig. 40) is constructed from A500 carbon steel of various sizes with a mass of approximately 700 kg. The steel is coated with both a brown primer and a black finishing layer to prevent rusting and consist of a platform for easy access to the upper portion of the primary test loop.

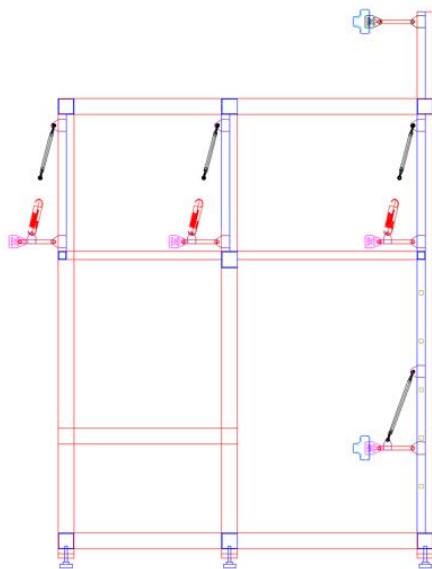


Fig. 40 – Primary support structure and location of test loop weight bearing supports

III.D.2. Weight Bearing Spring Supports

The primary test loop is supported by a floating spring system designed to hold the load of the facility and permit free thermal expansion about the high pressure pump which is the stationary point of expansion. The primary loop is supported with one type of system and the heat exchanger another.

Primary Loop Supports

All four supports in Fig. 40 consist of a square bar system shown in Fig. 41 to limit any cross motion of the system that may occur either in installation or operation, a slotted bracket welded to the tube permitting horizontal motion, and a high strength $\frac{3}{4}$ inch (1.91 cm) 4130 steel tube welded to a $\frac{3}{8}$ inch (0.95 cm) 24 right/left threaded tube end weld nut and attached to $\frac{3}{8}$ inch (0.95 cm) 24 right/left threaded shank steel ball end joint. The top three supports in Fig. 40 attach the square support to the $\frac{3}{4}$ inch (1.91 cm) tube with a 9 inch (22.9 cm) SS316 spring (Century Spring #81185) which allows thermal expansion in the vertical direction. The lower support in Fig. 40 is the vertical fixed point of expansion (level with the high pressure pump) and thus does not have a spring. All four supports are loaded with approximately the same mass (~ 45 kg).

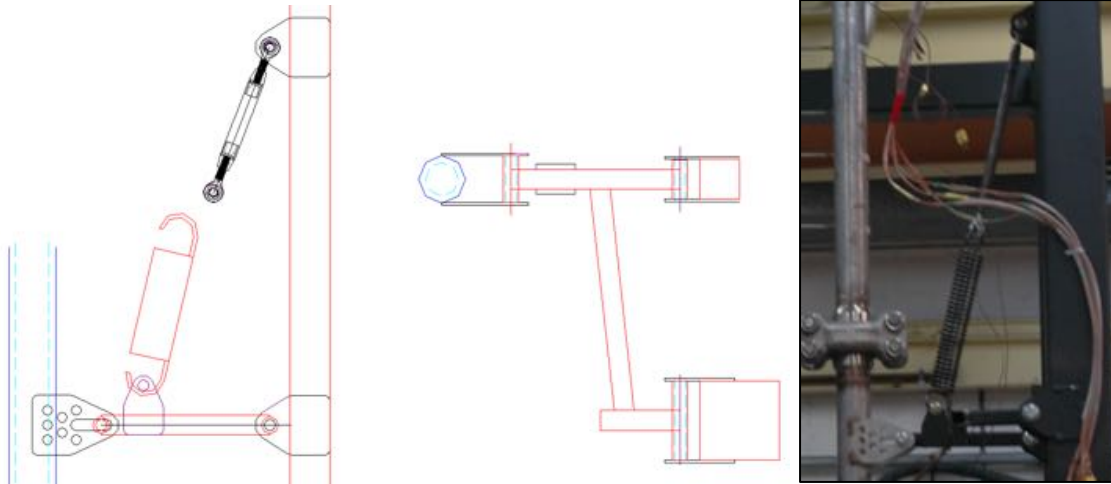


Fig. 41 – (Left) 2-D side and top view and (Right) photo of primary loop spring support

Heat Exchanger Support

Similar to the primary loop supports, the heat exchanger is supported with the same adjustable rod system with three springs (Century Spring #627) chosen to reduce the spring rate. A lower spring rate reduces any weight shifted to fittings as the heat exchanger expands vertically. The springs are supported by a removable overhang bolted to the facility (Fig. 42). The load of the heat exchanger can be alternatively transferred to bolted tabs if necessary (i.e. for removing fittings) which also help locate the exchanger in the other two directions during installation. These bolts must be loosened after installation to allow for unrestricted movement of the heat exchanger.

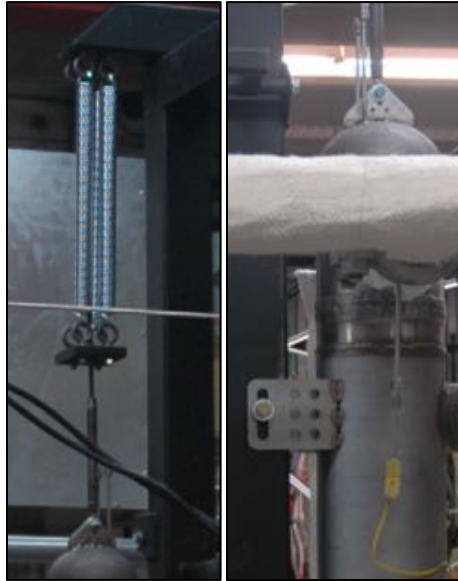


Fig. 42 – Support system for the high pressure heat exchanger

III.D.3. Secondary Cooling and Pressure Systems

The following sections of the secondary system elaborate on equipment and important features associated with heat removed from the primary system and the secondary system pressurization. The general view of this system is that all heat sinks of the primary system lead back to the large TRIGA tank which acts as a large thermal mass (Fig. 43). This tank relies on a 50/50 ethylene glycol/water plate heat exchanger to remove the energy build up within. The glycol/water coolant leads to storage tank and then to an industrial air chiller, the ultimate heat sink of the experiment (Fig. 44). The chiller is capable of removing up to 400 kW from the coolant. The incorporation of the TRIGA CHF Facility was, in part, because it was existing infrastructure which required only slight modifications to handle the heat sink requirements of the HPCHF facility.



Fig. 43 – Modified TRIGA CHF Facility

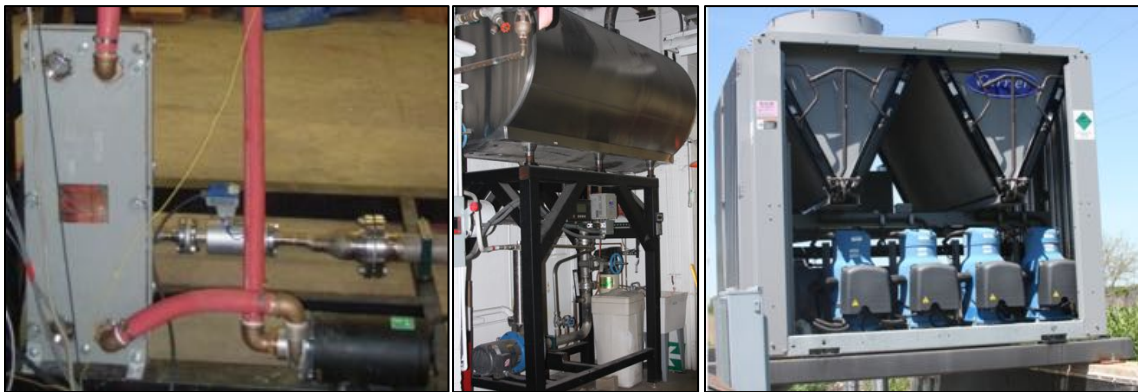


Fig. 44 – (Left) Plate heat exchanger. (Middle) Glycol/Water tank. (Right) Glycol/water air chiller.

TRIGA CHF Facility

Additional details of the HPCHF facility (e.g. parts not mentioned, capabilities, etc.) can be found in the Master's thesis by Michael Avery⁵³. Modification of the facility required the addition of a distribution manifold for secondary cooling (Fig. 45) needs and the addition of return lines to the tank port cover. These were the only necessary modifications of the flow systems required of this system. This facility is rated 0.4 MPa at 100°C.



Fig. 45 – TRIGA facility (Left) before and (Right) after addition of distribution manifold

High Pressure Pump

Due to the material (carbon steel) of the heat exchanger of the high pressure pump (Fig. 46), the 50/50 glycol/water coolant is used directly from a tap on the glycol/water line of the plate heat exchanger. In order for this to function, the glycol water chiller valves and valves on lines from the plate heat exchanger must be open. Additionally, the glycol/water pump must be running. If these conditions are met, the pump will remain sufficiently cooled for all operating conditions.



Fig. 46 – (Left) High pressure pump heat exchanger. (Right) Glycol/water control valves.

High Pressure Heat Exchanger

The shell side of the high pressure heat exchanger is cooled via water flowing from the TRIGA tank through a flowmeter (Kronhne MA-UFM-030) shown in Fig. 45 and Fig. 47 provided by a variable

speed pump. As this flow path shares that of the rod pressure boundaries and concentric tube heat exchanger, an adjustable valve is located after the flow meter in order to better control the heat removal (i.e. coolant flow rate) from the primary system while still providing adequate cooling to all other connected systems.

Rod Pressure Boundaries

As discussed in section III.C.2, the rod ends require constant cooling to protect the integrity of the pressure boundary and heater elements. From the distribution manifold, water lines run to and from each rod boundary at a rate of at least 4 L/min monitored with the flow meter shown in Fig. 47.

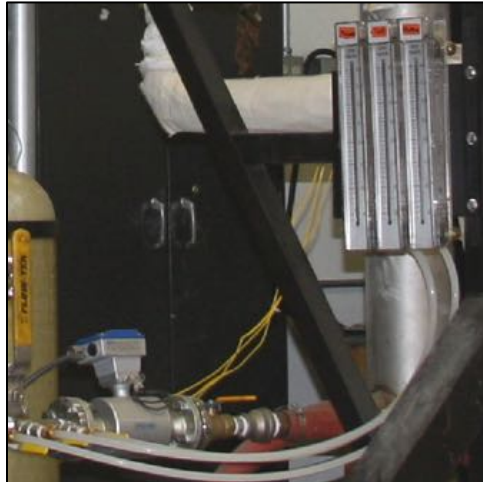


Fig. 47 – Secondary cooling manifold and flowmeters for rod pressure boundaries, pressurizer concentric tube heat exchanger and shell side of high pressure heat exchanger (flowmeter with blue top).

Pressurizer Concentric Tube Heat Exchanger

Similar to the rod pressure boundaries, the concentric tube heat exchanger uses the same distribution manifold to provide a flowrate of at least 4 L/min. Note, as boiling in the test section increases the flow through the high pressure side of the heat exchanger increases slightly. The high temperature of the fluid may boil the coolant slightly and the coolant lines may shake. This behavior is normal. Additionally, when a CHF event occurs and the heater elements turn off there may be the sound of

fluid flowing quickly in the concentric tube heat exchanger. This is simply high pressure fluid returning to the primary loop as the volume displaced by boiling is refilled. Once again this is normal behavior.

III.D.4. Data Acquisition System

The data acquisition (DAQ) system includes all hardware necessary for controlling devices and reading the various measurements of the system along with the software (LabVIEW 2013 32 bit) needed to interface with the hardware and record pertinent information for post processing (Fig. 48). The hardware components and their function in this system are given in Table IX.

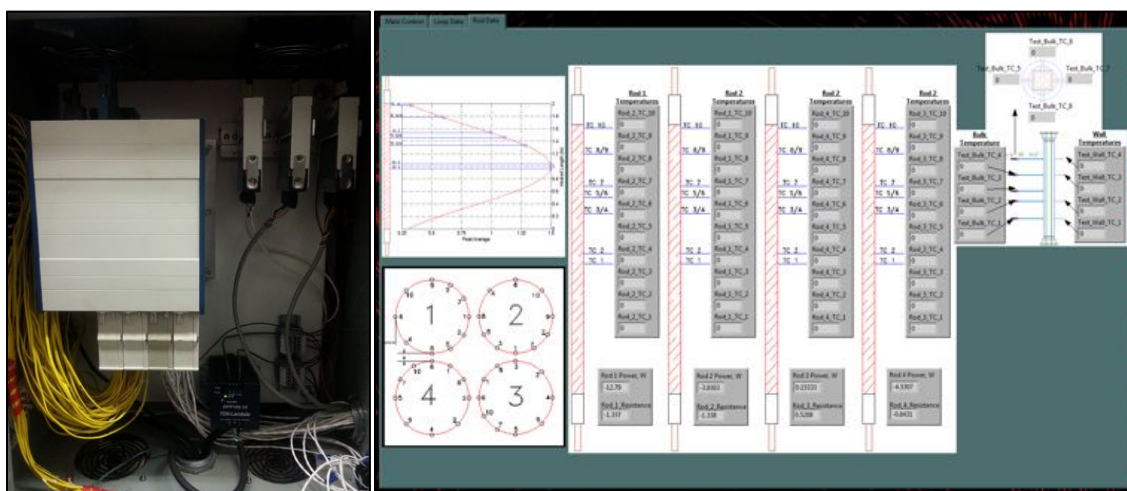


Fig. 48 – (Left) Primary hardware for DAQ system. (Right) Screenshot of portion of LabVIEW interface.

Table IX – Main components of the DAQ system

Component	Quantity	Function
PCI 6289	1	Interfaces SCXI components to computer
SCXI 1000	1	Chassis for SCXI components
SCXI 1102	2	TC Input Module
SCXI 1100	1	+/- 10 V Analog Input Module
SCXI 1160	1	General Purpose Relay Input Module
SCXI 1303	3	32 Channel Terminal Block (e.g. TCs and flowmeters)
SCXI 1324	1	Terminal Block for Relays (e.g. SCR/Inverter on/off)
NI 9263	2	Analog Output (e.g. SCR/Inverter control)
NI 9219	1	RTD Measurement

III.E. Pressure & Temperature Rating

Any operational range of a facility is limited by its lowest rated component. With the heat exchanger bypass valve and 11.5 L pressurization tanks in the system, the maximum allowable working pressure (MAWP) is 18 MPa with a maximum allowable working temperature (MAWT) of approximately 350°C in the primary loop and 200°C in the pressurizer system. If these components are replaced, the MAWP and MAWT are set by the high pressure heat exchanger to 25 MPa and 540°C (Grayloc clamps may or may not be permitted to be insulated at this temperature, check with manufacturer for details). The TRIGA facility is rated to 4 MPa and 100°C (temperature limited by secondary cooling line components).

In addition to mentioned components, it is important to always satisfy the temperature requirements of the rod pressure boundaries (section III.C.2), pressure transmitters (see product manual), etc. Any change to the facility requires a high pressure hydrotest approximately 1.5 times the maximum operating pressure expected to verify safe operation.

IV. Facility Performance

The performance of the facility includes various procedures used in different aspects of a facilities operation, important safety points, and the uncertainty in the measured properties (e.g. TCs, flowmeters, etc.). Each section that follows will elaborate on each of these important aspects in the operation of the HPCHF facility.

IV.A. Safety Considerations

The HPCHF facility was intentionally designed with significant pressure and temperature margins for safety (see section III for part item specific details and section III.E for overall facility operating limits). However, the high pressures and temperatures associated with this facility must be respected at ALL times. The following list identifies specific safety requirements and provides a helpful acronym to keep safety at the forefront of all activities. Appendix B contains a safety checklist of these points. The importance of understanding the effect of an action before being carried out cannot be overstressed.

- Never start the high pressure pump without water in the primary test loop
- Do NOT exceed 21°C (70°F) on Glycol/Water return line
- Do NOT exceed a TRIGA absolute tank pressure of 0.4 MPa
- Do NOT exceed temperature limits (200°C) of rod pressure boundaries
- Do NOT approach the facility while heating elements are energized.
- Power OFF and unplugged high pressure pump inverter for 15 minutes before servicing

Don't Forget Your **SOCS**!

- Be **S**afe: You are the most valuable piece of equipment. Every person has stop work authority.
- Be **O**rganized: Plan your emergency actions and keep pathways and work areas clean.
- Be **C**areful: High Voltage, Pressure, and Temperature are present and must be respected at ALL times. Additionally, the heater elements and other equipment are delicate; treat them with care so they are not broken.
- Be **S**mart: Think before you act! Ask for help if you need it! Stop work if necessary!

IV.B. Start-Up

Before every initiation of the start-up procedure, a review of the safety checklist is required. Upon completion, all DAQ hardware must be turned on followed by the computer and other equipment. A step by step procedure is included in Appendix B. This procedure readies the facility for operation.

Once the start-up procedure is completed, the system must be brought up to the appropriate initial pressure for a given experimental run. This procedure is outlined in Appendix B and includes setting the water level of the pressurizers and argon cover gas pressure. Fig. 49 is representative of the initial cold water level and pressure required to achieve a CHF event for a set test section mass flux and inlet pressure. As the system heats up and boiling occurs, the pressurizer water height will increase thereby increasing the system pressure.

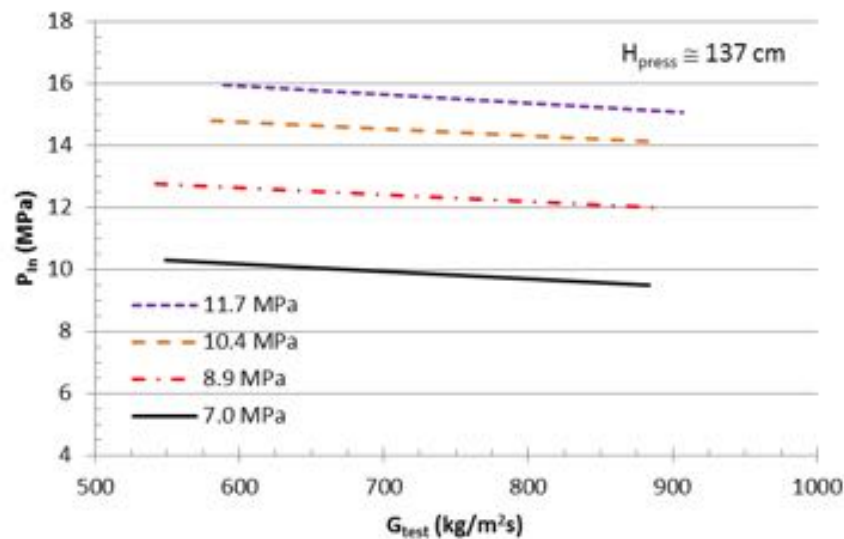


Fig. 49 – Test inlet pressure (P_{in}) at CHF occurrence as a function of the test section mass flux (G_{test}) based on an initial cold starting pressure (lines) with an initial cold pressurizer water height (H_{press}) of 137 cm.

IV.C. Steady State

Once the necessary starting pressure is achieved, the ‘Test Procedure’ in Appendix B increases the temperature of the facility by about $1\text{-}2^\circ\text{C}/\text{min}$ until the power to the facility is $\sim 20 \text{ kW/rod}$ below the expected power per rod at the CHF event. When this condition is met, the mass flux through the test section is increased to a $\sim 100 \text{ kg/m}^2\text{s}$ above the flux desired in the experiment (increased pressure drop as the CHF is approached will lower the mass flux) and the heat balance of the facility is adjusted to create a steady state condition from which CHF can slowly be approached.

IV.D. Experimental Run

From a steady state condition, the power of the heater elements is increased slowly ($\sim 1 \text{ kW/heater/min}$) while allowing the inlet temperature to slowly approach the desired subcooling and the pressure in the system to increase. If the power is increased too rapidly the low pressure side of the concentric tube heat exchanger will dryout and cut off the coolant flow. This must be avoided by not

increasing the heater power to quickly. If significant boiling occurs, the power should be slightly decreased and the coolant should be allowed to stabilize.

On approach to the CHF, the facility behaves in such a way that the only parameters controlled manually are the power to the heating elements and the rate of heat removal from the system (i.e. the inlet subcooling). Controlling these two parameters will slowly bring the facility to a critical condition where a CHF event will occur, recognizable by a significant spike (Fig. 50) in one or more of the thermocouples embedded in the heater elements. The ‘trip’ temperature for the system which indicates CHF occurrence is set approximately 150°C above the saturation point (i.e. ~75-100°C above the embedded thermocouple measurements).

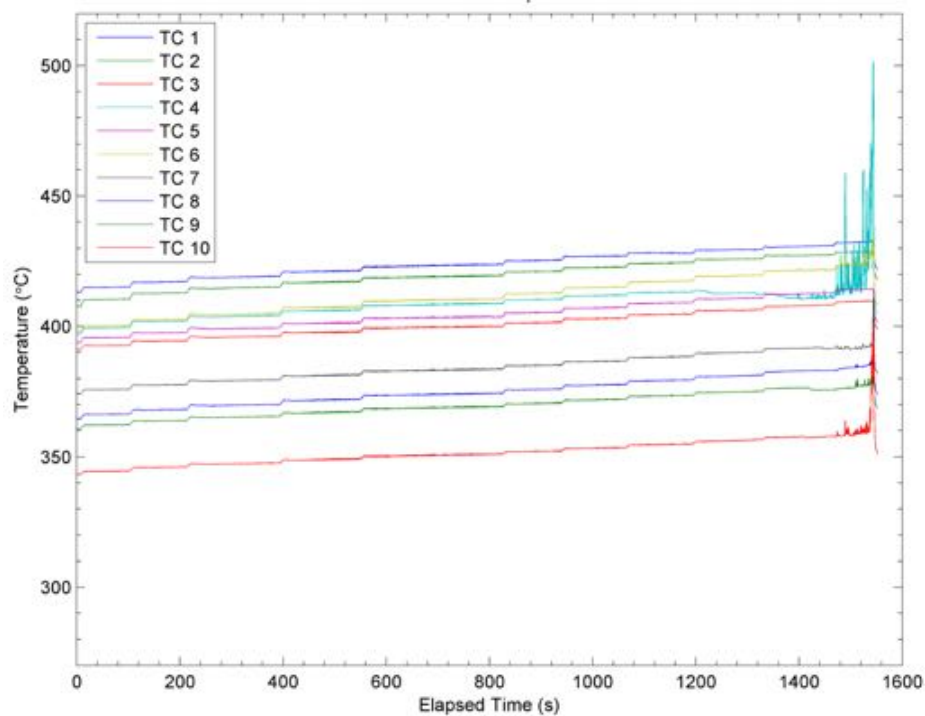


Fig. 50 – Heater element thermocouple measurements for an experimental run indicating a CHF event.

Once a CHF event occurs, the LabVIEW program is written such that each heater’s power will automatically reduce to a specified fraction of its previous level. When this occurs, the system will quickly return to the steady state established before the experimental run (with a little fine tuning of the

heat balance). When a steady behavior is achieved, another test can be performed (system pressure can be increased/decreased to a new condition if desired) or the facility can be shutdown.

IV.E. Shutdown

When testing is finished, the HPCHF facility should be slowly be decreased in temperature ($\sim 2^{\circ}\text{C}/\text{min}$) to below 100°C by adjusting heat transfer from the facility and slowly decreasing rod power as necessary. Pressure will decrease with temperature but do NOT manually bleed the pressure until the temperature is below 100°C .

Once the facility has reached the desired temperature, turn off power to heater elements (i.e. turn off power in LabVIEW, shutoff SCR fuse boxes, unplug SCRs), turn off and unplug all pump inverters, close gas cylinder if open, and depressurize the facility if necessary (it may remain pressurized for short durations provided the facility is clearly labeled and personnel with access to the laboratory are informed of the hazard). If an extended period of time is expected before the next use, drain the water from the facility and pressurize the facility to slightly above atmospheric pressure with argon.

When the system is cooled, de-energized and depressurized (if applicable); double check that all data is saved and continue to shut down all remaining systems. Appendix B contains the shutdown procedure and end of day checklist for reference.

IV.F. Error Analysis

An accurate interpretation of experimental results and facility operation requires an understanding of the error of the various measurements from the facility. The potential sources of measurement error for these CHF tests are associated with thermocouple location on the heated rods, calibration of the heater rods, inlet RTD, gauge pressure transmitter, mass flux (which depends on the inlet RTD, dP transmitter, gauge pressure, and flow meter used for orifice calibration accuracies), and dimensional tolerances (e.g. heater rod length and diameter, square channel dimensions).

As of yet a detailed error analysis has not yet been performed on the HPCHF facility and as such will be an important portion of the future work included on the final version of this document.

A portion of the uncertainty of the CHF depends upon the uniformity of the subchannels. Fig. 51 presents the bulk thermocouples discussed in Fig. 33 for each test run included in this report. If the channels were perfectly identical, bulk thermocouples 5-8 would indicate the same temperature within the measurement uncertainty ($\sim 2^\circ\text{C}$). Although not perfect, it appears that the channels on average are not highly variant lending confidence to the conclusion that there is no gross difference between any particular channel.

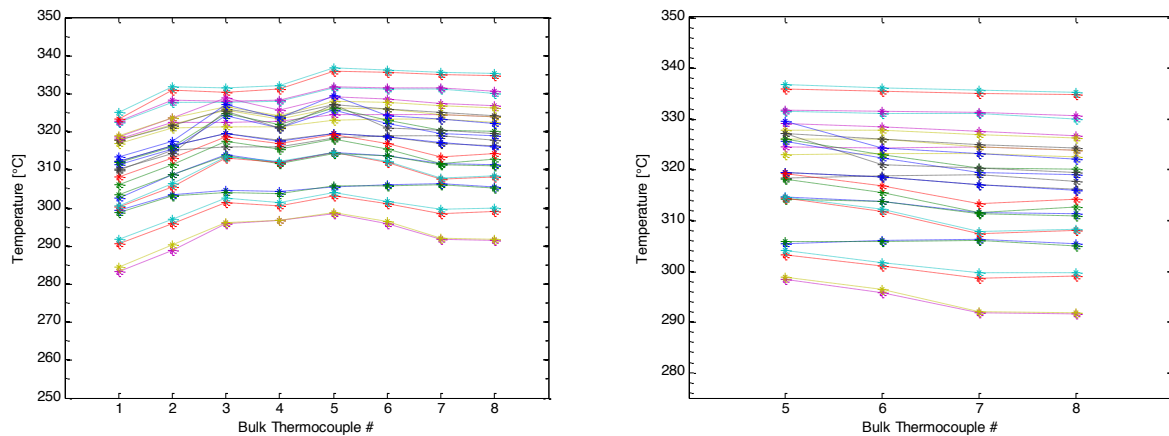


Fig. 51 – (Left) All bulk thermocouples at CHF occurrence. (Right) Bulk thermocouples at the same axial height.

V. Critical Heat Flux Data

The following section presents the preliminary CHF data gathered from using the HPCHF facility. Each section consists of the same set of data (29 data points) presented according to important parameters commonly evaluated in discussions of the CHF from a fixed inlet condition approach, and plotted both by local and average CHF. Local CHF refers to the heat flux at the location of the tripped thermocouple that indicated a CHF event. Average CHF refers to the average rod heat flux at the time of CHF occurrence. The range of conditions covered by these data is summarized in Table X. Data has been plotted in ranges to improve general interpretability. The inlet conditions at CHF occurrence is determined by a ten second interval average from the first data point prior to the CHF event.

Table X – Summary of Test Range of Preliminary CHF Data

Parameter	Range
Inlet Subcooling (kJ/kg)	320-480
Inlet Pressure (MPa)	9.5-16
Mass Flux (kg/m ² s)	540-910

V.A. Inlet Subcooling

Evaluation of the data in regards to inlet subcooling demonstrates that the expected trend of linear increase in the CHF with increasing subcooling. Fig. 52 is a plot of the data both for local and average CHF. Focusing on the data between 11 and 13.1 MPa at various mass fluxes (red circles, squares, and diamonds) seems to demonstrate the stated linear behavior. Additional data will help to verify this trend and provide a means to verify the quality of data²⁷.

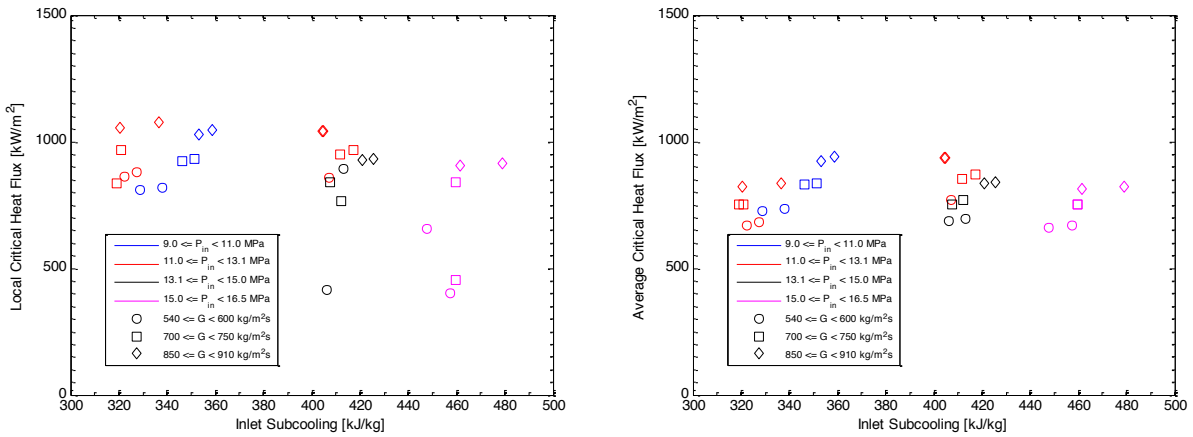


Fig. 52 – The CHF as a function of inlet subcooling

V.B. Inlet Pressure

Fig. 53 presents the CHF data as a function of the inlet pressure. This figure, especially focusing on a subcooling of 300 – 360 kJ/kg for varying mass fluxes (blue circles, squares, and diamonds), demonstrates a clear decrease in the CHF with increasing pressure as expected.

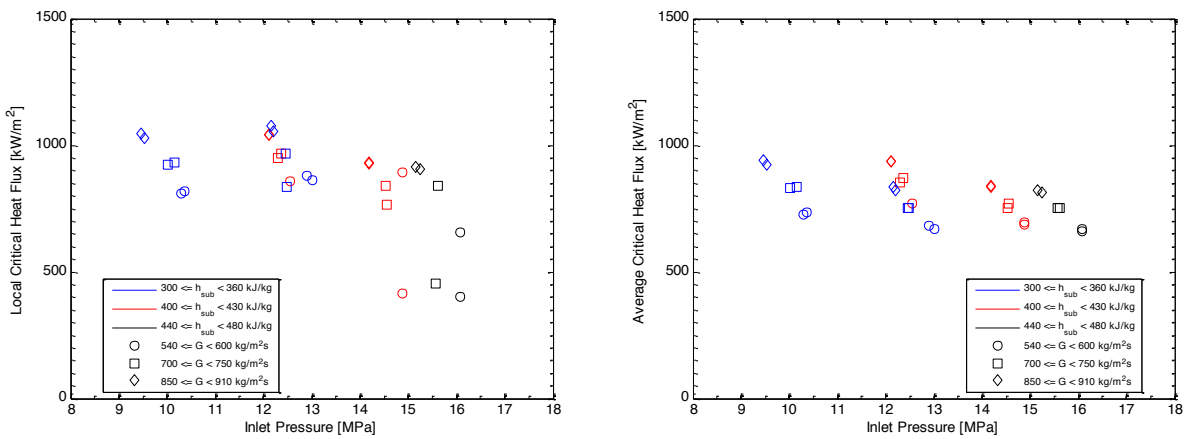


Fig. 53 – The CHF as a function of inlet pressure

V.C. Mass Flux

Increases in mass flux have been demonstrated in the literature review to increase the CHF given all other conditions are fixed. Each set of data at the same mass flux and pressure (Fig. 54) demonstrate that the CHF for these test ranges behave in this same manner.

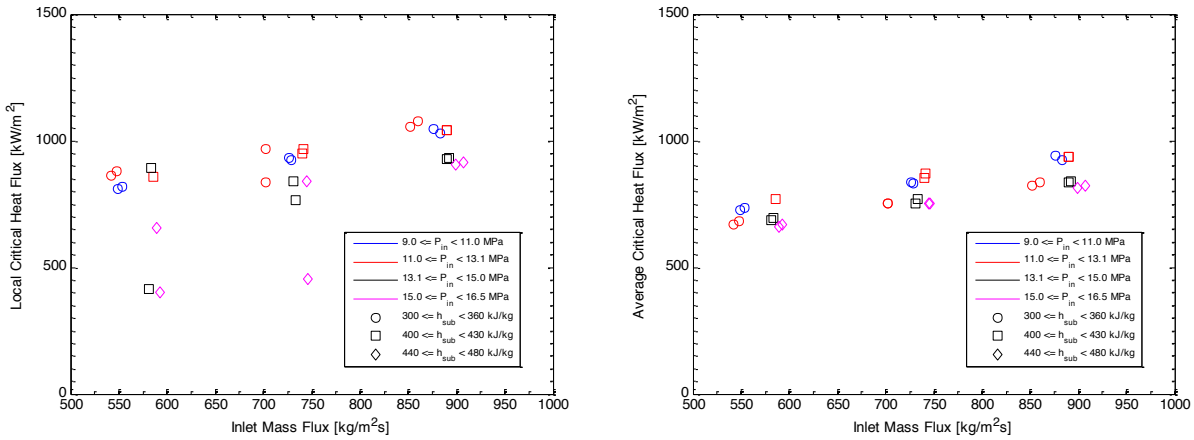


Fig. 54 – The CHF as a function of mass flux

V.D. Thermodynamic Quality

Fig. 55 demonstrates this behavior as well as provides support to the hypothesis that the CHF of these high pressure, low mass flux tests would be associated with the DNB CHF region (low quality). Increases in mass flux and pressure correspond to reductions in the quality at a CHF event with which the data set is consistent (Fig. 56).

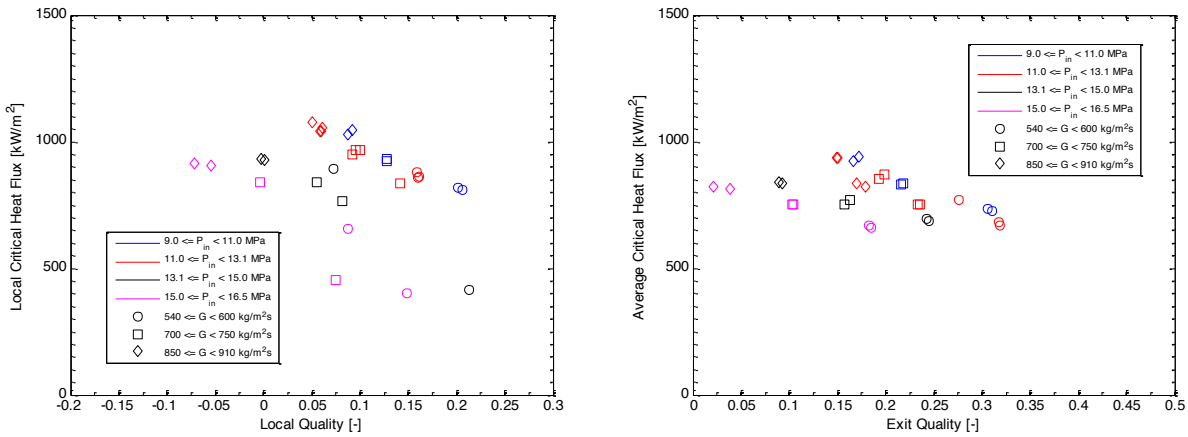


Fig. 55 – The CHF as a function of thermodynamic quality

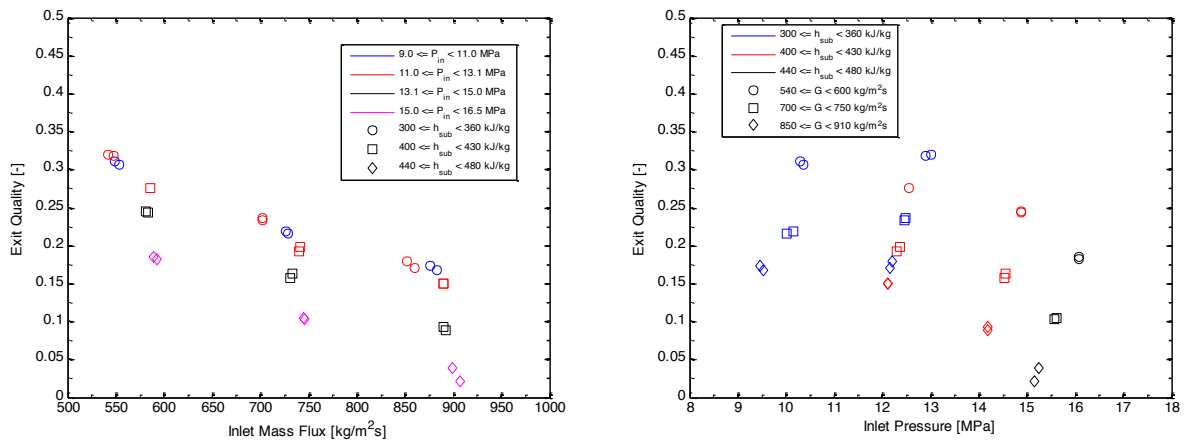


Fig. 56 – The thermodynamic exit quality as a function of (Left) mass flux and (Right) inlet pressure

V.E. CHF Location

The location of each tripped thermocouple, both axial and circumferential positions, for all tests is summarized in Fig. 57. See Table IV and Fig. 23 for exact dimensional locations of the thermocouples. More data points are included than tests run because at times more than one thermocouple would indicate CHF. The axial and circumferential location of the CHF events corresponds with expectations, (i.e. upstream of the end of the heated length and areas of minimum spacing). As no CHF occurrence occur on heater 1 or 2 there appears to be a slight non-uniformity in subchannel properties. However, when the

approach to CHF is observed, oscillations indicative of a approaching CHF condition are observed and CHF could be reasonably expected to occur with a small additional increase in power. A CHF location map such as Fig. 57 appears to be common and reasonable^{34 54}.

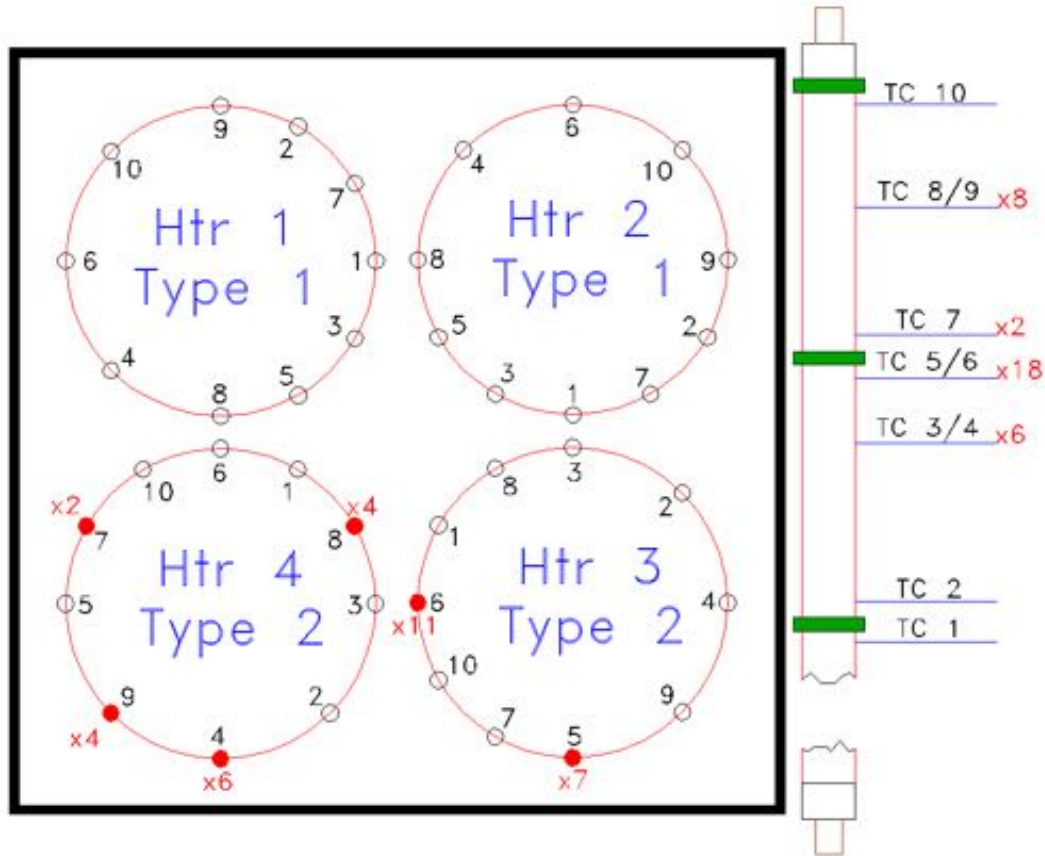


Fig. 57 – Axial and circumferential location of CHF occurrence detected with embedded thermocouples.

V.F. Repeatability

Two ‘identical’ tests were performed for every fixed inlet condition to determine reproducibility of the CHF event. A coarse evaluation of the variation for the primary inlet conditions and the associated heat fluxes is presented in Table XI. This table shows that there is very good consistency across tests with the same inlet conditions both in regards to the repeatability of the inlet parameters and the associated CHF. The majority of the error of the local CHF corresponded to three sets of tests which had multiple

tripped thermocouples. The larger deviation of the local CHF is therefore attributed to the inability to completely map the heater surfaces with temperature indicators and thereby capture the true onset of CHF location. For comparison, when the mentioned data sets are removed, the deviation is significantly reduced.

Table XI – Average deviation between identical tests

Inlet Subcooling	Inlet Pressure	Mass Flux	Local CHF	Average CHF
0.9%	0.2%	0.2%	7.7%	0.6%
3.3 kJ/kg	0.024 MPa	1.7 kg/m ² s	51 kW/m ²	4.4 kW/m ²
			1.6%*	
			14 kW/m ² *	
*excludes 6 data points with highly variant axial tripped TC				

As additional data is gathered, it will be assimilated into the evaluation for repeatability. The uncertainty of the parameters mentioned is different, and likely greater, than the deviations determined from this repeatability analysis. See section IV.F for a discussion of measurement uncertainty.

VI. Summary & Future Work

In summary, a high pressure, low mass flux critical heat flux test facility has been designed, constructed, and has been used for the acquisition of a preliminary round of data. Initial evaluation indicates that general trends documented in the literature for fixed inlet conditions appear to be satisfied and that the data is repeatable.

The future work required of this project is four fold. First, additional data points will be obtained to increase the range of tests performed including repeatability tests. Second, gathered data will be compared with the various prediction methods indicated in the literature review along with a detailed uncertainty analysis of the data. Third, a subchannel code (e.g. COBRA) and/or a system modeling tool (e.g. TRACE) will be used to model the system for additional insight. Fourth, a possible preliminary investigation into visualization methods of the test section may be undertaken.

Once completed, this report will be updated with suggestions, findings, data base, etc. and be presented again to the Examination Committee members indicated on the title page in partial fulfillment of the requirements degree of Doctorate of Philosophy in Nuclear Engineering and Engineering Physics.

Bibliography

- [1] T. B. Drew and A. C. Mueller, "Boiling," in *American Institute of Chemical Engineers*, Toronto, 1937, pp. 449-473.
- [2] S. Nukiyama, "The Maximum and Minimum Values of the Heat Q Transmitted from Metal to Boiling Water under Atmospheric Pressure," *International Journal of Heat and Mass Transfer*, vol. 9, pp. 1419-1433, 1966.
- [3] International Atomic Energy Agency (IAEA), "Thermohydraulic Relationships for Advanced Water Cooled Reactors," TecDoc 1203, 2001.
- [4] G. P. Celata and A. Mariana, "CHF and Post-CHF (Post-Dryout) Heat Transfer," in *Handbook of Phase Change: Boiling and Condensation*.: Taylor & Francis, 1999, ch. 17, pp. 443-493.
- [5] J. G. Collier and J. R. Thome, *Convective Boiling and Condensation*, 3rd ed.: Clarendon Press, 1994.
- [6] S. M. Ghiaasiaan, *Two-Phase Flow, Boiling and Condensation In Conventional and Miniature Systems*.: Cambridge University Press, 2007.
- [7] G. F. Hewitt, "Burnout," in *Handbook of Multiphase Systems*.: Hemisphere Publishing Corporation, 1982, ch. 6.4, pp. 6.66-6.141.
- [8] G. F. Hewitt and N. S. Hall-Taylor, "Burnout," in *Annular Two-Phase Flow*.: Pergamon Press, 1970, ch. 11, pp. 219-252.
- [9] L. S. Tong and Y. S. Tang, *Boiling Heat Transfer and Two-Phase Flow*, 2nd ed.: Taylor & Francis, 1997.
- [10] L. S. Tong and J. Weisman, *Thermal Analysis of Pressurized Water Reactors*, 3rd ed.: American Nuclear Society, 1996.
- [11] Y. Ahang, and J. R. Howell A. Faghri,.: Thermal Fluids Central, 2009, ch. 8.2.
- [12] S. G. Kandlikar, "Critical Heat Flux in Subcooled Flow Boiling - An Assessment of Current Understanding and Future Directions for Research," *Multiphase Science and Technology*, vol. 13, no. 3, pp. 207-232, 2001.
- [13] The U.S. Department of Energy's Office of Nuclear Energy. (2014, September) Small Modular Nuclear Reactors. [Online]. <http://www.energy.gov/ne/nuclear-reactor-technologies/small-modular-nuclear-reactors>
- [14] J. N. Reyes Jr. and P. Lorenzini, "NuScale Power: A modular, scalable approach to commercial

- nuclear power," *Nuclear News*, pp. 97-104, June 2010.
- [15] U. S. Nuclear Regulatory Commission, "Briefing on Small Modular Reactors," in *Transcript of Proceedings*, 2011.
- [16] International Atomic Energy Agency, "Status of Small and Medium Sized Reactor Designs," IAEA, Supplement 2012.
- [17] Z. Liu and J. Fan, "Technology Readiness Assessment of Small Modular Reactor (SMR) Designs," *Progress in Nuclear Energy*, vol. 70, pp. 20-28, 2014.
- [18] United States Nuclear Regulatory Commission. (2014, September) [Online].
<http://www.nrc.gov/reactors/advanced/nuscale.html>
- [19] M. S. McGough, "Presentation to Energy NorthWest Member Forum XVI," NuScale Power, Kennewick, Washington, Presentation 2013.
- [20] K. Welter, "NuScale Technology Overview to the U. S. Nuclear Regulatory Commission," NuScale Power, Rockville, MD, Presentation 2010.
- [21] M. De Angelis, M. S. Greenwood, and J. Yang, "Critical Heat Flux under Natural and Forced Convection," in *American Nuclear Society Annual Meeting*, Chicago, Illinois, 2012.
- [22] K. Mishima and M. Ishii, "Experimental Study on Natural Convection Boiling Burnout in an Annulus," in *7th International Heat Transfer Conference*, Munich, 1982, pp. 309-314.
- [23] D. C. Groeneveld, S. C. Cheng, and T. Doan, "1986 AECL-UO Critical Heat Flux Lookup Table," *Heat Transfer Engineering*, vol. 7, no. 1-2, pp. 46-62, 1986.
- [24] D. C. Groeneveld et al., "The 1995 Look-Up Table for Critical Heat Flux in Tubes," *Nuclear Engineering and Design*, vol. 163, pp. 1-23, 1996.
- [25] D. C. Groeneveld et al., "The 2006 CHF Look-Up Table," *Nuclear Engineering and Design*, vol. 237, pp. 1909-1922, 2007.
- [26] A. N. Baker, "Study of Existing Data and Correlations on Rod Bundle Critical Heat Flux," University of Wisconsin, Madison, Master's Thesis 1972.
- [27] E. D. Hughes, LP Ka-Lam, A. N. Baker, and M. W. Carbon, "A Compilation of Rod Array Critical Heat Flux Data Sources and Information," *Nuclear Engineering and Design*, vol. 30, pp. 20-35, 1974.
- [28] C. F. Fighetti and D. G. Reddy, "Parametric Study of CHF Data Volume 1: Compilation of Rod Bundle Chf Data Available at the Columbia University Heat Transfer Research Facility,"

EPRI/Columbia University, NP-2609 Volume 1 Research Project 813, 1982.

- [29] D. G. Reddy and C. F. Fighetti, "Parametric Study of CHF Data Volume 2: A Generalized Subchannel CHF Correlation for PWR and BWR Fuel Assemblies," EPRI/ Columbia University, NP-2609 Volume 2 Research Project 813, 1982.
- [30] C. F. Fighetti and D. G. Reddy, "Parametric Study of CHF Data Volume 3, Part 1: Critical Heat Flux Data," EPRI/Columbia University, NP-2609 Volume 3 Part 1 Research Project 813, 1982.
- [31] C. F. Fighetti and D. G. Reddy, "Parametric Study of CHF Data Volume 3 Part 2: Critical Heat Flux Data," EPRI/Columbia University, NP-2609 Volume 3 Part 2 Research Project 813, 1982.
- [32] R. J. Weatherhead, "Nucleate Boiling Characteristics and the Critical Heat Flux Occurrence in Subcooled Axial-Flow Water Systems," Argonne National Laboratory, Argonne, Illinois, AEC Research and Development Report ANL-6675, 1963.
- [33] S. Moon, W. Baek, and S. H. Change, "Parametric Trends Analysis of the Critical Heat Flux based on Artificial Neural Networks," *Nuclear Engineering and Design*, vol. 163, pp. 29-49, 1996.
- [34] S. Moon, S. Chun, S. Cho, and W. Baek, "An Experimental Study on the Critical Heat Flux for Low Flow of Water in a Non-Uniformly Heated Vertical Rod Bundle Over a Wide Range of Pressure Conditions," *Nuclear Engineering and Design*, vol. 235, pp. 2295-2309, 2005.
- [35] Y. W. Wu, G. H. Su, S. Z. Qiu, and B. X. Hu, "Experimental Study on Critical Heat Flux in Bilaterally Heated Narrow Annuli," *International Journal of Multiphase Flow*, vol. 35, pp. 977-986, 2009.
- [36] A. W. Bennet, G. F. Hewitt, H. A. Kearsley, R. K. F. Keeys, and D. J. Pulling, "Studies of Burnout in Boiling Heat Transfer," *Transactions of the Institution of Chemical Engineers*, vol. 45, no. 21, pp. T319-T333, 1967.
- [37] S. C. Yao, L. E. Hochreiter, and W. J. Leech, "Heat-Transfer Augmentation in Rod Bundles Near Grid Spacers," *Transactions of ASME*, vol. 104, pp. 76-81, February 1982.
- [38] D. C. Groeneveld and W. W. Yousef, "Spacing Devices for Nuclear Fuel Bundles: A Survey of their Effect on CHF, Post-CHF Heat Transfer and Pressure Drop," in *ANS/ASME Topical Meeting on Reactor Thermal-Hydraulics*, Saratoga, New York, 1980.
- [39] General Electric, "General Electric BWR Thermal Analysis Basis (GETAB): Data, Correlation and Design Application," NEDO-10958-A 1977.
- [40] L. S. Tong, "Boundary-Layer Analysis of the Flow Boiling Crisis," *International Journal of Heat and Mass Transfer*, vol. 11, pp. 1208-1211, 1968.

- [41] J. Weisman and B. S. Pei, "Prediction of Critical HEat Flux in Flow Boiling at Low Qualities," *International Journal of Heat and Mass Transfer*, vol. 26, no. 10, pp. 1463-1477, 1983.
- [42] C. H. Lee and I. Mudawwar, "A Mechanistic Critical Heat Flux Model for Subcooled Flow Boiling Based on Local Bulk Flow Conditions," *International Journal of Multiphase Flow*, vol. 14, no. 6, pp. 711-728, 1988.
- [43] W. S. Lin, C. H. Lee, and B. S. Pei, "An Improved Theoretical Critical Heat Flux Model for Low-Quality Flow," *Nuclear Technology*, vol. 88, no. 3, pp. 294-306, 1989.
- [44] G. Yadigaroglu, "CMFD and the Critical-Heat-Flux Grand Challenge in Nuclear Thermal-Hydraulics - a letter to the Editor of this special issue," *International Journal of Multiphase Flow*, p. in press, 2014.
- [45] M.V. De Angelis, "The UW-Madison High Pressure Test Facility Design Report," University of Wisconsin, Madison, 2012.
- [46] Stern Laboratories Inc., "Technical Specification for 9.5 mm OD Fuel Simulators with a Cosine Axial Power Profile for the University of Wisconsin," Ontario, Canada, SLTS-76, 2012.
- [47] S.K. Moon, S.Y. Chun, S.D. Hong, W.P. Baek S.W. Akhtar, "Modeling Capability of R134a for a Critical Heat Flux of Water in a Vertical 5x5 Rod Bundle Geometry," *International Journal of Heat and Mass Transfer*, vol. 49, pp. 1299-1309, 2006.
- [48] U. Muller X. Cheng, "Critical Heat Flux and Turbulent Mixing in Hexagonal Tight Rod Bundles," *International Journal of Multiphase Flow*, vol. 24, pp. 1245-1263, 1998.
- [49] S.Y. Chun, S.K. Moon, W.P. Baek, Y. Kim S. Cho, "Flooding Limited CHF in a Vertical 3x3 Rod Bundle with Non-Uniform Axial Heat Flux," *Nuclear Engineering and Design*, vol. 235, pp. 77-90, 2005.
- [50] S.K. Moon, S. Chun, J.K. Park, D.H. Hwang, W.P. Baek, S.K. Park, C.Y. Lee K.Y. Choi, "Critical Heat Flux Tests for an Appliation of the Three-Pin Fuel Test Loop in HANARO," *Heat Transfer Engineering*, vol. 29, pp. 685-694, 2008.
- [51] S.H. Chang B.S. Shin, "CHF Experimeint and CFD Analysis in a 2x3 Rod Bundle with Mixing Vane," *Nuclear Engineering and Design*, vol. 29, pp. 899-912, 2009.
- [52] MFC-3Ma-2007, "Orifice Plates," *ASME*, pp. 19-27.
- [53] Michael Avery, "Project Report of Critical Heat Flux at Conditions Representative of TRIGA-Type Reactors," University of Wisconsin, Madison, Master's Thesis 2012.
- [54] J. Yang, M. Avery, M. De Angelis, and M. S. Greenwood, "4 Rod Bundle Test Appendix,"

University of Wisconsin, Madison, 2013.

Appendix A Official Documents

Original Project Proposal



Critical Heat Flux Phenomena at High Pressure and Low Mass Fluxes: Tests and Models

PI: Michael Corradini, University of Wisconsin Collaborators: Mark Anderson, University of Wisconsin

Qiao Wu, Oregon State University

Program: Reactor Concepts RD&D (SMR-3)

ABSTRACT

The proposed work will examine critical heat flux (CHF) phenomena, both by experiment and modeling, under high-pressure and low mass flux conditions, in a heated rod bundle for prototypic integral reactor core designs. The experimental results will provide important validation data for an updated critical heat flux model for use in thermal-hydraulic computer codes to be used for integral light water reactors (LWRs), which operate under these conditions. The conceptual LWR designs considered as a reference for this study are the NuScale Pressurized Water Reactor Power Plant and the Babcock-Wilcox mPower Reactor Power Plant. There is minimal experimental data at low mass flux conditions and high pressure and not in a rod bundle. Our work will provide data and associated modeling, as well as a better understanding of the CHF process with prototypic flow and pressure ranges in a rod bundle geometry for integral small modular reactor (SMR) designs. These data currently do not exist.

The CHF phenomenon is one of the key physical phenomena that limit the allowable linear power for a nuclear reactor core design under steady-state operating conditions, and can be a limiting condition under transients. The advanced LWR designs being considered for modular reactor plants normally involve core flow rates (either under natural circulation or forced circulation) at mass fluxes far below current LWR conditions. Based on an open literature review, one finds that no data exist for rod bundles and only a sparse database for heated tubes. For these advanced designs to address the needed safety conditions, some fundamental understanding must be obtained for CHF under these conditions.

This proposal will focus on four specific tasks:

- 1) Perform a scaling analysis for rod bundle geometry that is appropriate for the proposed small modular reactor core designs for a single rod and multiple rod experiments;
- 2) Design and construct a CHF test facility similar to existing flow loop with scoping tests;
- 3) Under prototypic controlled flow and pressures conditions, measure flow velocities and pressure drops approaching CHF to determine onset of CHF and flow instabilities. Create a database of experimental CHF data and any associated flow instability conditions;
- 4) Compare the CHF data with current correlations, if appropriate, and develop a more mechanistic model to increase the reliability of predictions under low flow conditions.

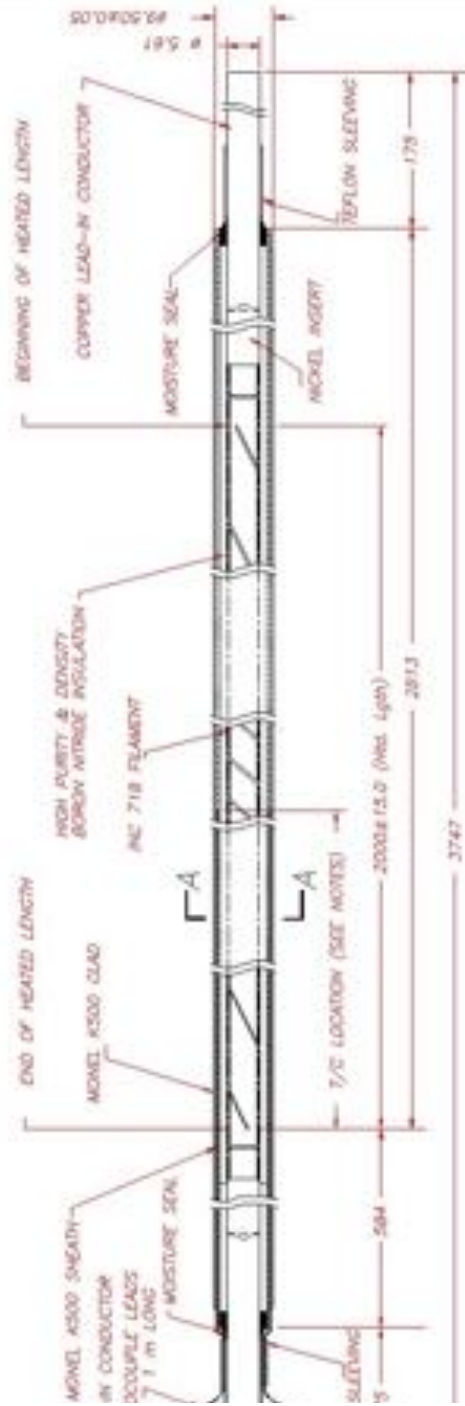
Stern Labs Non-Uniform Heater Elements

General Requirements

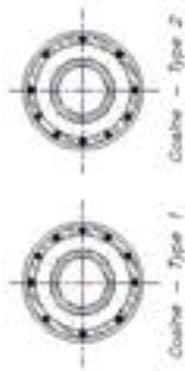
Operating Pressure (max)	16.0 MPa
Operating Temperature (max)	347 °C
Design Power:	100 kW
Design Voltage	570 V
Nominal Current:	175.4 A
Axial Power Profile (Cosine):	0.300 / 1.500 / 0.300
Linear Power (maximum):	75.0 kW.m ⁻¹
Heated Length:	2000 ± 15 mm
Outside Diameter:	9.50 ± 0.05 mm
Electrical Resistance: (at room temperature)	3.094 ± 5% Ohms ± 5% of lot average per type (before swaging)
Electrical Resistance: (estimated at operating temp.)	3.249 ± 5% Ohms
Clad Surface Finish	As swaged, 1.6 µm Ra or better
Maximum External Sheath Temperature (recommended at maximum power)	430 °C

Thermocouple Specifications

Type	Premium grade ANSI Type K 0.51 mm diameter
Sheath	Inconel 600
Insulation	MgO
Junction	Ungrounded, BN backfilled
Length	2750 mm (approx.)
Resistance, Lead to Sheath	60 x 10 ⁵ Ohm m at ± 50 V (before swaging) 6 x 10 ⁵ Ohm m at ± 50 V (after swaging)
Length Beyond Sheath	minimum 750 mm



A-A



- NOTES:
1. All dimensions in millimeters.
 2. The fuel simulators will be manufactured with the axial locations of thermocouples as per Figure 2.

High Pressure Pump Information

MODEL NO: OCT-3E-36I
SERIAL NO: 2452314-1

*****APPLICATION DATA*****

FLUID: SUPERCRITICAL WATER
TDH (FT): 56.5
CAPACITY (GPM): 160
PUMPING TEMP (F): 60-1100
SPECIFIC GRAVITY: 1.0
VISCOSITY (CP): 1.122 @ 60 F
VAPOR PRESS (PSIA): 0.25 @ 60 F
SUCTION PRESS (PSIG): ADVISE
NPSH AVAIL (FT): ADVISE
NPSH REQ (FT): 18.1

IMPELLER DCA (IN): 5
NET WT (LBS): 350

***MATERIALS OF CONSTRUCTION**

BEARING HOUSINGS: 316SS
CASING: INCONEL 625
IMPELLER: 316SS
BEARINGS: CG-A/316SS
STATOR & ROTOR: HASTC/316LSS
JOURNALS: M-2
CIRC TUBE ASSY: INCONEL 625
GASKETS: SPIRAL WOUND

*****MODEL DATA*****

DISCHARGE FLG: 2" GRALOC
VERTICAL DISCHARGE DOWN
SUCTION FLG: 2" GRALOC
HORIZONTAL END SUCTION
DESIGN PRESSURE: 3600 PSI
@ 1100 F

*****MOTOR DATA*****

PH: 3 CYC: 60 VOLT: 230
SPEED: 3450 RPM INEL CLASS: H
TCO SET: 356 F ENC: TELC
STATOR FILL: DRY - NONE

FULL LOAD AMPS: 17.6
FULL LOAD KW: 5.0
START KVA: 28.4
HORSEPOWER: 5.0
LOCKED ROTOR CODE: F
OPER TEMP CODE: T3A
PH SEQ: 1-2-3

>ROTATION INDICATOR
>COMMERCIAL GRADE PUMP
>REMOVABLE HEAT EXCHANGER
>3/60/230
>SLEEVED ANTIMONY BEARINGS
>HASTELLOY C STATOR LINER &
ROTOR SLEEVE
>USE SPIKE-RESISTANT WINDING
INSULATION AS REQUIRED FOR
MOTOR TO BE SUITABLE FOR USE
WITH VARIABLE FREQUENCY DRIVE
--VFD BY OTHERS.
>CAPPED CASING VENT.
>ALL PRESSURE-RETAINING PARTS
SUBJECT TO HIGH TEMPERATURE
(CASING, STATOR BAND, FRONT
END BELL, REAR COVER) TO BE
INCONEL 625.

HYDRAULIC TEST-NON WITNESSED
PROCEDURE A-15852

HYDROSTATIC TEST-NON WITNESSED
PROCEDURE A-21409

QUALITY ASSURANCE REQUIREMENT
PROVIDE HYDROSTATIC TEST
REPORT AND CERTIFIED CURVE
AND IOM MANUAL WITH PUMP

SEE LINE 900 FOR DRAWING
REQUIREMENTS.

Appendix B Facility Operation Procedures

Start-Up/Shutdown Procedure

Notice: This procedure assumes a pressure test has been performed and all miscellaneous actions (e.g. orifices installed properly) have been performed. Consult 'Safety Checklist' before Operating Facility.

Start-up Procedure

1. Plugin all DAQ hardware.
2. Turn on computer and startup LabVIEW program. An error will result if the DAQ hardware was not turned on before the computer.
3. Open valves for secondary cooling and ensure flow path for the LP pump is open.
4. Open valves for Glycol/Water chiller line. Shut the yellow bypass valve halfway to increase flow to GW HX.
5. Attach compressed air line.
6. Plug in SCRs and Inverters.
7. Start Glycol/Water chiller in the back corner of the room (switch on side of display with frequency of ~40 Hz).
8. Turn on GW pump to 2.5 V.
9. Fully open HX Bypass valve (counter clockwise).
10. Turn on LP pump for cooling to rod ends/accumulator line (~1 gpm - ~4.5V) and slightly to shell of HX (~0.15kg/s) by adjusting voltage and valve to HX.
11. Switch fuse boxes for all rods to ON.

Shut Down Procedure

1. Slowly cool facility to below 100°C.
2. Turn off rod power.
3. Turn off HP pump.
4. Turn off LP pump.
5. Turn off GW pump.
6. Turn off glycol/water chiller.
7. Close gas cylinder and regulator.
8. Depressurize facility to slightly above atmospheric conditions and drain water (if need to refill with water or if facility will be idle for an extended period of time).
9. Detach compressed air line for pneumatic valves.
10. Shutoff SCR fuse boxes.
11. Unplug SCRs.
12. Unplug Inverters.
13. Shutdown LabVIEW program.
14. Unplug DAQ hardware.
15. Backup test data.
16. Close valves to all secondary cooling and to LP pump.
17. Shutdown computer.

Safety/End of Day Checklist

1. Never start the HP pump without water in the test loop!
2. Don't exceed 21°C (70°F) on Glycol return line.
3. Glycol pump takes a few moments to turn on/off. Operating frequency should be ~40Hz.
4. Do not let TRIGA tank pressure > 4 bar (58 psia)
5. Maximum operating condition for Viton o-rings and the moisture seal (copper rod/sheath interface) of the rods is 200°C. The top graphite thread lubricant is good to a higher temp but will burn off if too high. The LabView code recommends a lower operating temperature for safety and to avoid boiling to insure consistent cooling.
6. Stay away from test section when rod fuse boxes are in ON position.
7. HP Inverter requires a wait of 15 min once unplugged before performing maintenance.
8. Check that top/bottom TCs are flush to surface.

Don't Forget Your **SOCS**!

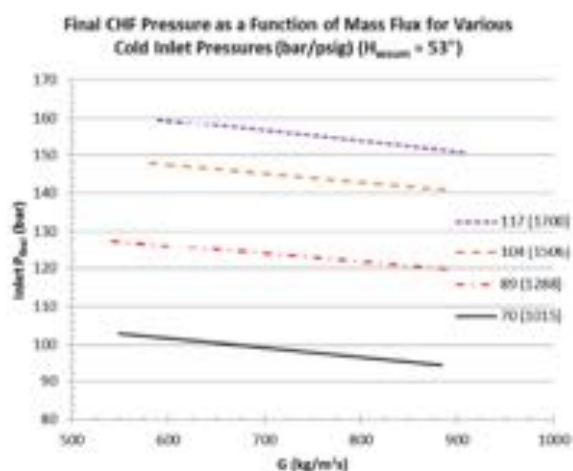
- Be **S**afe: You are the most valuable piece of equipment. Every person has stop work authority.
- Be **O**rganized: Plan your emergency actions and keep pathways and work areas clean.
- Be **C**areful: High Voltage, Pressure, and Temperature are present and must be respected at ALL times. Additionally, the heater elements and other equipment are delicate; treat them with care so they are not broken.
- Be **S**mart: Think before you act! Ask for help if you need it! Stop work if necessary!

- | | |
|--------------------------|--|
| <input type="checkbox"/> | Unplugged Inverters (2) for pumps (HP/LP/GW) |
| <input type="checkbox"/> | Unplugged SCRs |
| <input type="checkbox"/> | Fuse boxes switched to OFF |
| <input type="checkbox"/> | Glycol/Water Chiller turned OFF |
| <input type="checkbox"/> | Unplugged compressed air |
| <input type="checkbox"/> | Unplugged DAQ hardware |
| <input type="checkbox"/> | Backed up Data |
| <input type="checkbox"/> | Shutdown computer |
| <input type="checkbox"/> | All valves (e.g. secondary cooling) are closed |
| <input type="checkbox"/> | Gas cylinder and regulator are closed |

Pressurization/Test Procedure

Pressurization Procedure

1. Check the water level of the accumulator in the LabVIEW code. If it is too low, depressurize the accumulator and fill. Take the opportunity to ensure the Level dP line is full of water.
2. Using the needle valve, drain water from the accumulator until the desired water level is reached.
3. Close regulator on Argon tank (counter clockwise).
4. Open Argon tank.
5. Open regulator until pressure is slightly greater than the accumulator pressure.
6. Open pneumatic valve from the Argon tank to accumulator.
7. Slowly increase pressure to the necessary point which will attain the correct pressure after heat up and approach to CHF (see table for rough guideline).
8. Close pneumatic valve from the Argon tank to accumulator. Close Argon tank.



Test Procedure

1. Turn on HP pump to ~ 300 kg/m²s (1 V).
2. Set and keep CHF trip temperature ~ 75 - 100°C above the hottest rod temperature ($\sim 150^\circ\text{C}$ above the saturation temperature).
3. Turn on all rods to ~ 1 kW (enable SCR and Manual) and slowly increase 'Test Inlet Temperature' (1 - $2^\circ\text{C}/\text{min}$) until significant boiling begins to occur. This will be evident by sharp increases in pressure and popping in accumulator HX line. Pressure will increase as fluid heats up.
4. As needed change rod power, adjust HPHX valve, and adjust flow to shell side of HX being mindful of the temperature limits on rod ends.
5. Increase flow as needed to limit boiling while also adjusting heat loss.
6. Achieve a steady condition at a flow rate slightly above the desired test mass flux. The pressure will be below the test pressure but will significantly increase as CHF is reached.
7. Set test file name, set desired recording frequency (5 Hz), turn on 'Step Power at CHF On/Off', and Initialize test.
8. Continue to manipulate heat exchange to limit boiling on the low pressure HX (flex hose will shake as boiling increases).
9. Manually increase power slowly until CHF occurs. Power increases should be slow enough that the flow to the accumulator HX does not dry out (flow meter will begin to jump between 0 and its set flow rate).
10. When CHF occurs, turn off the data recording. The power will be automatically reduced to a lower power level and manual control will be shut off.
11. Turn manual control back on, establish a steady condition, change the test name, and repeat the procedure for the next test condition.

Critical Heat Flux Phenomena at High Pressure & Low Mass Fluxes:

NEUP Final Report Part II - Modeling

PART I: Experiments

Michael Corradini (UW PI) and M.Scott Greenwood

Department of Engineering Physics, UW-Madison

Corradini@engr.wisc.edu

PART II: Modeling

Qiao Wu (OSU Co-PI) and Jeff Luitjens

Department of Nuclear Engineering, Oregon State University

Qiao.Wu@Oregonstate.edu

October 15, 2014



WISCONSIN
UNIVERSITY OF WISCONSIN-MADISON



U.S. DEPARTMENT OF
ENERGY

Nuclear Energy

Development of a Mechanistic Critical Heat Flux Correlation

ABSTRACT

In industry the understanding of the limits of the boiling heat transfer mode is crucial to modeling the thermal hydraulic processes that occur and to ensure the safe operation of industrial plants; especially in nuclear power plants which are characterized by relatively high heat fluxes. At high heat fluxes a critical point is reached where the heat removal mechanism(s) is not sufficient enough to remove energy from the surface. This heat flux is referred to the critical heat flux (CHF). When the CHF point is reached the surface temperature rises due to the inability to remove the energy from the surface. This results in temperatures often greater than the melting temperature of the surface. Understanding of the heat transfer processes and the transitions involved is needed to appropriately model the mechanisms of the heat transfer modes to predict the onset of CHF to prevent such scenarios.

Currently the mechanisms of boiling heat transfer are not well understood and rely heavily on empirical correlations and lookup tables. This results in correlations that are often very specific to the scope of the developmental application often resulting from the lack of modeling of mechanistic behaviors. Modeling of the mechanistic process can result in a broader applicability of a developed model. Focus here will be given to the development of a mechanist based low-flow critical heat flux correlation based on mass, momentum, and energy conservation equations.

The ability to develop a mechanistic based model allows for more confidence in the conceptual design phase of facilities that utilize high heat flux conditions. It also allows for the development for a more mature correlation. This has a significant effect on operating costs of high heat flux operating facilities in terms of margin management. A better understanding of one's limits with higher confidence allows for reduction in the unnecessary margin that is used to account for any uncertainties in the utilized correlation. This reduction in margin allows for facilities to operate at a higher capacity increasing capital.

TABLE OF CONTENTS

ABSTRACT	2
List of Figures	5
List of Tables	5
1. INTRODUCTION	6
1.1. Motivation	6
2. UNIVERSITY OF WISCONSIN TEST FACILITY OVERVIEW	6
2.1. Low Pressure Test Facility	6
2.2. High Pressure Test Facility	8
3. Comparison of Existing Correlations to Data	9
4. MODEL DEVELOPMENT AND METHODOLOGY	12
4.1. Heat Transfer Modes	12
4.2. Bubble Forces Perpendicular to a Vertical Heated Surface	13
4.2.1. Surface Tension (F_{σ})	14
4.2.2. Inertial Force (F_{inert})	14
4.2.3. Virtual Mass Force (F_{vm})	15
4.2.4. Bubble Shear Lift Force (F_{sL})	16
4.3. Net Force Balance	18
4.4. Closure Relations	19
4.4.1. Surface Cavity Size	20
4.4.2. Bubble Contact Angle	21
4.4.3. Bubble Contact Radius and Bubble Radius	21
4.4.4. Wall Superheat	21
4.4.5. Nucleation Site Density	21
4.4.6. Convective Heat Flux Correlation	23
4.5. Model Implementation Algorithm	23
5. Results	25

5.1.	Nodalization.....	25
5.2.	Calibration	25
5.3.	Convergence Criteria	26
5.4.	Critical Rod Power.....	27
5.5.	Critical Heat Flux Value.....	28
5.6.	Critical Heat Flux Location	30
6.	Conclusions.....	32
7.	REFERENCES.....	33

LIST OF FIGURES

Figure 2-1 Cross-sectional view of the University of Wisconsin high pressure test facility.....	8
Figure 2-2 Power profile and thermocouple placement of Wisconsin university high pressure test facility.....	8
Figure 3-1 CHF Correlation comparisons to CHF data.....	11
Figure 3-2 Subset of CHF Correlation comparisons to CHF data.	11
Figure 4-1 Bubble perpendicular force balance on a vertically aligned heated surface.	13
Figure 4-2 Activated minimum cavity size versus wall superheat.....	20
Figure 4-3 Nucleation site density correlation comparison to experimental data from Basu [11]22	
Figure 4-4 Correlation algorithm for determining critical heat flux.	24
Figure 5-1 Nodalization of critical heat flux model.	25
Figure 5-2 Relation between system pressure and minimum active cavity radius.	26
Figure 5-3 Convergence process for determine critical heat flux.	27
Figure 5-4 Model pin critical power comparison to experimental data.....	28
Figure 5-5 Model critical heat flux value comparison to experimental data.	29
Figure 5-6 Model critical heat flux comparison to experimental data.....	30

LIST OF TABLES

Table 2-1 Low pressure experimental test conditions for Avery [1].	7
Table 2-2 Low pressure experimental test results for Avery [1].....	7
Table 2-3 High pressure experimental test conditions for Avery.	9
Table 2-4 High pressure experimental test results for Avery.....	9
Table 3-1 Subset of critical heat flux correlation in literature.	10
Table 5-1 Model performance on predicting the critical heat flux.	27
Table 5-2 Model performance on predicting the critical heat flux.	29
Table 5-3 Model performance on predicting the critical heat flux location.....	30

1. INTRODUCTION

1.1. Motivation

Many methods exist in literature aiming to predict the onset of the critical heat flux. Many of which are developed for specific geometric and fluid conditions with upwards of 40% error. This limits the potential broad applicability of a developed model. It is believed that the development of a mechanistic based critical heat correlation will be more suited to allow for the development a more broadly applicable correlation by means of modeling the surface behavior through conventional mass, force, and energy balances. Development of a physics based relation is believed to remove the heavy dependence on geometry and fluid conditions as long as these characteristics are captured by the physical model itself.

The ability to develop a widely applicable model allows for more confidence in conceptual design phase of facilities that utilize high heat flux conditions. It also allows for the development for a mature correlation in which the error is greatly reduced (as much as half of the conventional reported error). This has a significant effect on the operating costs of high heat flux operating facilities in terms of margin management. A better understanding of one's limits with a higher confidence allows for a reduction in the unnecessary margin that is used to account for any uncertainties in the utilized correlation. This reduction in margin allows for facilities to operate at a higher capacity increasing capital.

2. UNIVERSITY OF WISCONSIN TEST FACILITY OVERVIEW

2.1. Low Pressure Test Facility

The experimental data of Avery [1] is used as the first data set for CHF investigation. A low-pressure forced flow test facility was constructed with full scale fuel pins simulating typical conditions of the General Atomics TRIGA reactor. The tested conditions for the CHF are presented in Table 2-1.

Table 2-1 Low pressure experimental test conditions for Avery [1].

Rod Power	0 - 50 kW
Mass Flux	0 - 400 kg/m ² -s
Pressure	110 - 200 kPa
Channel Diameter	5.1 cm
Heated Pin Diameter	3.7 cm
Heated Pin Length	38.1 cm

The power profile of the tested rod is shown in Equations (2-1) and (2-2):

$$\frac{q''(x)}{q''} = 1.626 \cos(4.926z + 5.34471) \quad (2-1)$$

where x represents the length along the flow channel. The axially dependent heat flux can be described as:

$$q''(x) = 1.626 \cos(4.926z + 5.34471) \frac{q_{pin}}{A_h} \quad (2-2)$$

The results of the critical heat flux tests for the typical General Atomics TRIGA fuel pin tests are summarized in Table 2-2.

Table 2-2 Low pressure experimental test results for Avery [1].

Test #	Inlet Temperature [°C]	Pressure [kPa]	Mass Flux [kg/m ² -s]	Critical Rod Power [kW]
Test 1	30	110	132	33.48
Test 2	30	110	132	32.47
Test 3	30	110	117	30.88
Test 4	30	110	46	23.01
Test 5	30	110	25	19.54
Test 6	30	170	138	38.7
Test 7	30	170	138	37.7
Test 8	30	170	111	35.2
Test 9	30	170	52	29.24
Test 10	30	170	19	22.07
Test 11	30	230	146	44.9
Test 12	30	230	146	43.88
Test 13	30	230	113	40.74
Test 14	30	230	20	24.96
Test 15	50	110	169	31.46
Test 16	50	170	170	37.69
Test 17	50	230	165	41.88

2.2. High Pressure Test Facility

The experimental data of Greenwood is used as the second data set for comparison. A high-pressure forced flow test facility was constructed with a configuration as shown in Figure 2-1 and Figure 2-2. The tested conditions for CHF are presented in Table 2-3.

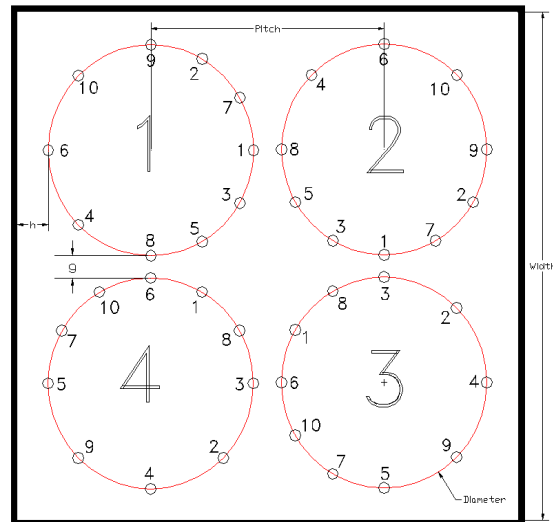


Figure 2-1 Cross-sectional view of the University of Wisconsin high pressure test facility.

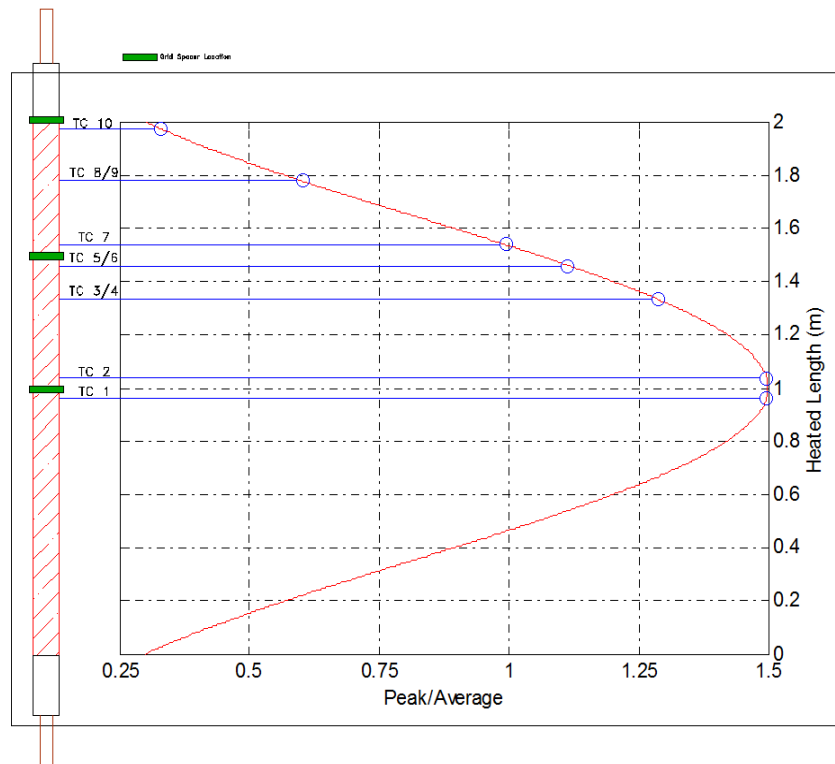


Figure 2-2 Power profile and thermocouple placement of the University of Wisconsin high pressure test facility.

Table 2-3 High pressure experimental test conditions for Greenwood.

Number of Rods	4
Total Cumulative Power	160 - 225 kW
Mass Flux	540 - 890 kg/m ² -s
Pressure	120 - 130 kPa
Channel Width	2.675 cm
Heated Pin Diameter	0.95 cm
Heated Pin Length	200 cm

The axially dependent heat flux used for these tests is shown in (2-3):

$$q''(z) = 0.8187 + 0.6813 \cos\left(4.873\left(z/L - 1/2\right)\right) \frac{q_{pin}}{A_h} \quad (2-3)$$

The results of the critical heat flux tests are summarized in Table 2-4.

Table 2-4 High pressure experimental test results for Avery.

Test #	Inlet Temperature [°C]	Pressure [MPa]	Mass Flux [kg/m ² -s]	Average Critical Rod Power [kW]
Test 1	254.33	12.55	585.68	46.06
Test 2	251.19	12.30	740.34	51.03
Test 3	250.61	12.37	740.97	52.00
Test 4	251.05	12.11	889.43	55.98
Test 5	251.17	12.11	889.61	55.98
Test 6	275.29	13.02	542.19	39.98
Test 7	273.41	12.90	547.46	40.67
Test 8	271.56	12.47	701.66	45.00
Test 9	271.12	12.47	702.05	45.00
Test 10	265.52	12.16	860.17	50.01
Test 11	269.14	12.20	852.36	49.00

3. COMPARISON OF EXISTING CORRELATIONS TO DATA

Low-flow and low-pressure data provided by University of Wisconsin (Table 2-2) with varying test conditions (Table 2-1) were first used to assess the capability of a subset of existing CHF models as shown in Table 3-1. Figure 3-1 shows the performance of the tested correlations and Figure 3-2 shows a subset that includes correlations that are thought to do more reasonably well (within about 30% of experimental results). The lack of consistent predictability of currently available correlations expresses the need for a more general CHF correlation. This can be accomplished through the development of a mechanistic based correlation such as that proposed in the next section.

Table 3-1 Subset of critical heat flux correlation in literature.

Original Source	Correlation
Katto [2]	$q_c = We^{-0.043} \left[h_{fg} + 1.043 We^{0.043} \Delta h_i \right] GA$ $We = \frac{G^2 L}{\sigma \rho_f}$
Oh & Englert [3]	$q_c = 0.458 \left[h_{fg} + \Delta h_i \right] GA$
Lowdermilk [4]	$q_c = \frac{1080}{D_h^{1/5}} \left[\frac{4}{A_h} \right]^{-0.15} \left[GA \right]^{0.85}$
Monde [5]	$q_c = \frac{0.16 GA h_{fg}}{1 + 0.00067 \left[\frac{\rho_f}{\rho_g} \right]^{0.6}}$
Mishima & Ishii [6]	$q_c = A \left[\Delta h_i G + \left(\frac{1}{C_o} - 0.11 \right) h_{fg} \sqrt{\rho_g \Delta \rho D_h g} \right]$ $C_o = 1.2 - 0.2 \sqrt{\rho_g / \rho_f}, \text{ for round tubes}$ $C_o = 1.35 - 0.35 \sqrt{\rho_g / \rho_f}, \text{ for rectangular channels}$
Mishima & Nishihara [7]	$q_c = 0.00146 G A_h h_{fg} + \left[\frac{0.725}{1 + (\rho_g / \rho_f)^{1/4}} \right]^2 A h_{fg} \sqrt{w \rho_g \Delta \rho g}$ <p>The channel width (w) is taken to be the channel diameter.</p>
Kaminaga [8]	$q_c^* = 0.005 G^{*0.611} + \frac{0.7(w / \lambda)^{0.5}}{\left[1 + (\rho_g / \rho_f)^{1/4} \right]^2}$ $q_c^* = \frac{q_c}{A_h h_{fg} \sqrt{\lambda \rho_g \Delta \rho g}}$ $G^* = \frac{G}{\sqrt{\lambda \rho_g \Delta \rho g}}$ $\lambda = \left(\frac{\sigma}{g \Delta \rho} \right)^{1/2}$ <p>The channel width (w) is taken to be the channel diameter.</p>

Original Source	Correlation
Park	$q_c = \frac{A_f C_w^2 h_{fg} \sqrt{\rho_g g \Delta \rho D_h}}{A_h \left[1 + (\rho_g / \rho_f)^{1/4} \right]^2}$ $C_w^2 = 1.22 \left(\frac{L}{D_h \sqrt{g(\rho_f - \rho_g)}} \right)^{0.12} \left(\frac{\rho_g}{\rho_f} \right)^{0.064} \left(1 + 0.055 Bo - 4.08 \times 10^{-3} Bo^2 \right)$

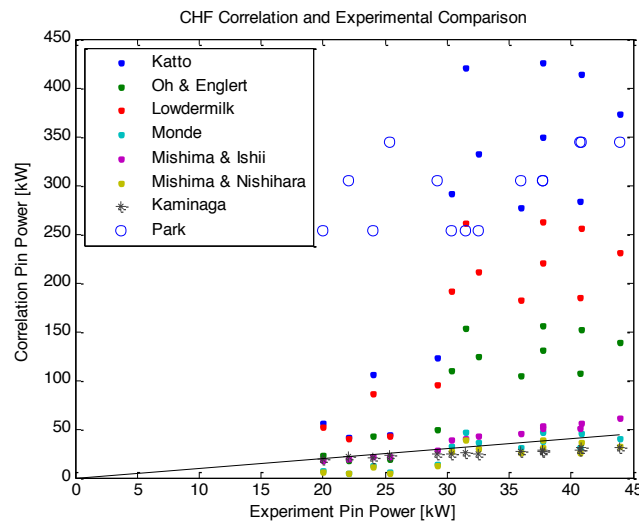


Figure 3-1 CHF Correlation comparisons to CHF data.

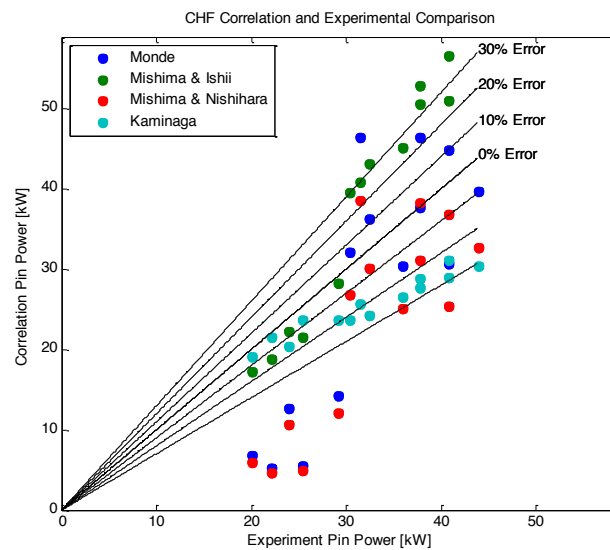


Figure 3-2 Subset of CHF Correlation comparisons to CHF data.

4. MODEL DEVELOPMENT AND METHODOLOGY

Derived here will be the framework for determining a limiting surface heat flux for flow boiling. This includes determining the separate heat transfer components that make up the total heat flux. Focus is given to the phenomena that occur very near the surface (bubble dimensions). This approach is investigated by relating the forces acting on a bubble growing on a heated surface within a flow field. The limiting heat removal (critical heat flux) case is hypothesized to occur at the highest attainable boiling frequency at a nucleation site. The highest attainable boiling frequency implies that at the same time a bubble departs from a nucleation site the next bubble immediately begins to grow. This model does not depend on the coalescence of departed bubbles away from the surface.

For heat transfer to occur from the local superheated fluid to the bubble (evaporation) the bubble internal temperature must be lower than the local fluid superheat temperature. When the bubble internal vapor temperature equals the local superheat temperature the evaporative heat transfer ceases. It is thus assumed that this represents the maximum potential for boiling heat transfer and the bubble(s) are assumed to be at its maximum potential internal vapor temperature set equal to the wall temperature.

4.1. Heat Transfer Modes

The total surface heat flux can be partitioned into the following components:

$$\begin{aligned} q''_{\phi} & - \text{convective heat flux} \\ q''_I & - \text{evaporative (interface) heat flux} \\ q''_{trans} & - \text{transient conduction heat flux} \\ q''_{slide} & - \text{sliding heat flux} \end{aligned} \tag{4-1}$$

The total heat flux is then expressed as:

$$q''_{total} = q''_{\phi} + q''_I + q''_{trans} + q''_{slide} \tag{4-2}$$

It is assumed that the heat flux at the surface is high enough (due to the CHF condition) such that the bubble generation rate is continuous at a given nucleation site. Also, due to the high heat flux the bubble departure from a cavity and bubble lift-off from the surface are assumed coincident (i.e. the bubble does not slide on the heated surface). With these assumptions liquid is not allowed to occupy the region of the previous departed bubble nor is there a displacement of liquid along the surface where boiling does not

occur. Thus the transient conduction heat flux mechanism at the nucleation site and heat removal from sliding of a bubble along the surface is not present and Equation (4-5) can be simplified to:

$$q''_{total} = q''_{\phi} + q''_I \quad (4-3)$$

Relations describing the evaporative interfacial energy transfer and the single phase heat transfer are developed in the following sections.

4.2. Bubble Forces Perpendicular to a Vertical Heated Surface

For a vertically aligned flow channel the assumed forces acting perpendicular to a heated surface are:

- surface tension force
- inertial (evaporative) force
- virtual mass inertial force
- bubble shear lift force

These forces are outlined in Figure 4-1. The forces in action on this volume are described in the following sub-sections. For this analysis only the forces perpendicular to the surface are assumed to participate in the departure of the bubble. The parallel forces are assumed to be equal and opposite.

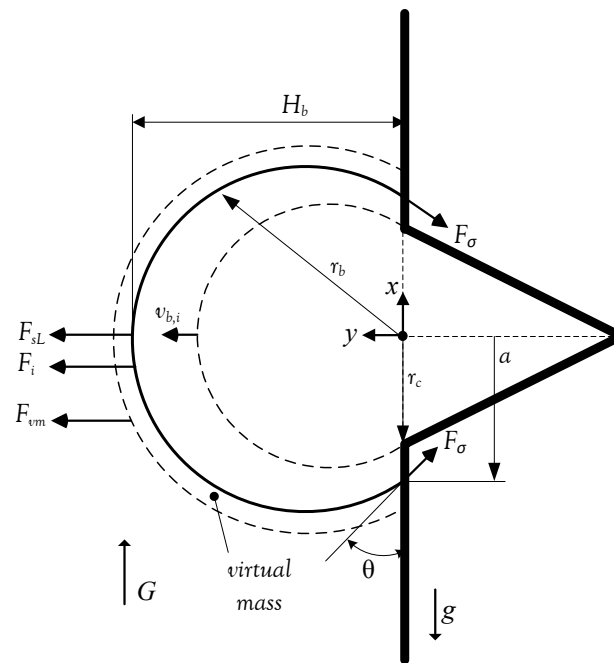


Figure 4-1 Bubble perpendicular force balance on a vertically aligned heated surface.

4.2.1. Surface Tension (F_σ)

The surface tension force describes the force along the bubble interface contact line with the surface. This forces works to keep the bubble interface attached to the surface. This force is expressed as:

$$\begin{aligned} F_{\sigma,y} &= 2\pi\sigma a \sin(\theta) \\ \sigma &= \text{surface tension} \\ a &= \text{radius of vapor and solid contact area} \\ \theta &= \text{liquid-vapor-solid interface contact angle} \end{aligned} \tag{4-4}$$

4.2.2. Inertial Force (F_{inert})

The inertial force derives from the bubble growth rate due to the interfacial mass transfer across the bubble interface. This evaporation is proportional to the heat flux and the bubble size (interfacial area). Due to symmetry and neglecting advancing versus receding contacting angles of the bubble, the inertial forces in the direction parallel to the heated surface negate each other. In the direction perpendicular to the surface there is a net inertial force projected above and away from the interface of the bubble.

$$F_{inert,y} = \frac{d(mv)}{dt} = v \frac{\partial m}{\partial t} + m \frac{\partial v}{\partial t} \tag{4-5}$$

The bubble surface velocity perpendicular to the plate is determined by an energy balance of the growing bubble. The bubble here is assumed to have a spherical shape as shown in Figure 4-1. An energy balance of the bubble yields:

$$\rho_v h_{fg} \frac{dV_b}{dt} = q''_I A_b \tag{4-6}$$

The terms q''_I and A_b represent the heat transfer rate at the bubble interface and the total bubble interface surface area. The volume of a spherical shaped bubble is:

$$V_b = \frac{\pi}{6} H_b (3a^2 + H_b^2) \tag{4-7}$$

where a is the vapor-solid contact area radius and H_b is the bubble height from the surface to the bubble cap, both of which vary with time as the bubble grows. The total surface area of a spherical shaped bubble is:

$$A_b = 2\pi r_b H_b = \pi(a^2 + H_b^2) \quad (4-8)$$

Inserting these geometric relations into the bubble interface velocity (Equation (4-6)) perpendicular to the heated surface results in the following expression:

$$\frac{\pi}{2} \rho_v h_{fg} \frac{dH_b}{dt} (a^2 + H_b^2) = q_i'' \pi (a^2 + H_b^2) \quad (4-9)$$

$$v_{b,i} = \frac{dH_b}{dt} = \frac{2q_i''}{\rho_v h_{fg}} \quad (4-10)$$

It is noted that the interface velocity is independent with time with the assumption that the interfacial heat flux is also constant with time (quasi steady state).

Using the defined boundary in Figure 4-1 the mass evaporation rate at the interface is found similarly using the energy balance equation:

$$h_{fg} \frac{dm_b}{dt} = q_i'' A_b, \quad (4-11)$$

$$\dot{m}_b = \frac{dm_b}{dt} = \frac{q_i'' \pi (a^2 + H_b^2)}{h_{fg}}. \quad (4-12)$$

Inserting Equation (4-10) and Equation (4-12) into Equation (4-5) and noting that since the rate of change of the bubble height is zero the inertial force for is then:

$$F_{inert,y} = v_{b,i} \frac{dm_b}{dt} = \left(\frac{q_i''}{h_{fg}} \right)^2 \frac{\pi (a^2 + H_b^2)}{\rho_v} \quad (4-13)$$

4.2.3. Virtual Mass Force (F_{vm})

The virtual mass inertial force derives from the bubble growth rate due to the evaporation rate but effects the immediate surrounding 'thin layer' of liquid around the bubble interface which acts and moves with the bubble. Here virtual mass acts an extension to the bubble. The equations developed here will be derived where the virtual mass constant (C_{vm}) can be substituted depending on the relation desired.

The induced mass inertial force is written similarly to the bubble inertial mass except that the liquid density is used and the virtual mass volume is related to the bubble volume by:

$$V_{vm} = C_{vm} V_b \quad (4-14)$$

The mass exchange across the virtual mass interface is evaluated as:

$$F_{vm} = \frac{d(m_{vm} v_{b,i})}{dt} = v_{b,i} \frac{\partial m_{vm}}{\partial t} + m_{vm} \frac{\partial v_{b,i}}{\partial t} \quad (4-15)$$

Since $m = \rho V$, $V_{vm} = C_{vm} V_b$ then $m_{vm} = C_{vm} \frac{\rho_l}{\rho_v} m_b$, the virtual mass force can be written as:

$$F_{vm} = \frac{d(m_{vm} v_{b,i})}{dt} = C_{vm} \frac{\rho_l}{\rho_v} \frac{d(m_b v_{b,i})}{dt} = C_{vm} \frac{\rho_l}{\rho_v} F_{inert,y} \quad (4-16)$$

$$F_{vm} = C_{vm} \frac{\rho_l}{\rho_v} \left(\frac{q_i^*}{h_{fg}} \right)^2 \frac{\pi (a^2 + H_b^2)}{\rho_v} \quad (4-17)$$

4.2.4. Bubble Shear Lift Force (F_{sL})

The bubble shear lift force results from the entrainment phenomena on a bubble from the bulk fluid movement parallel to the surface. The result of adding this force is to aid in bubble removal from the surface and will thus result in a decrease in the maximum heat flux required to remove a bubble from the surface. With the increase of this force the evaporative potential will decrease but there will be a counter increase in the convective heat flux.

The lift force as derived by Klausner and Mei [9] is expressed as:

$$F_{sL} = \frac{1}{2} C_L \rho_l u_l (y')^2 \pi r_b^2 \quad (4-18)$$

where y' is the bubble center of mass distance from the wall approximated here as $y' \approx H_b / 2$. The lift coefficient is expressed by [9] as:

$$C_L = 3.877 G_s^{\frac{1}{2}} \left[Re_b^{-2} + 0.014003 G_s^2 \right]^{\frac{1}{4}} \quad (4-19)$$

with

$$G_s = \left| \frac{du_l}{dy} \right| \frac{y}{u_l(y)} \quad (4-20)$$

$$Re_b = \frac{r_b u_l(y')}{\nu_l} \quad (4-21)$$

Using the standard turbulent velocity profile near the wall:

$$u^+ = \frac{u_l}{u^*} = \frac{u_l}{\sqrt{\tau_w / \rho_l}} \quad (4-22)$$

$$y^+ = \frac{y u^*}{\nu_l} = \frac{y \sqrt{\tau_w / \rho_l}}{\nu_l} \quad (4-23)$$

The bubbles are assumed to be of a small size thus the distance from the center of the bubble to wall is assumed to be small with a $y^+ \leq 5$ then:

$$y^+ = u^+. \quad (4-24)$$

The wall shear stress is calculated as:

$$\tau_w = C_f \frac{1}{2} \rho_l U_l^2 \quad (4-25)$$

where U_l is the volumetric average velocity. Then the wall shear stress is defined as:

$$C_f = \frac{\lambda}{4} \quad (4-26)$$

$$\lambda = \begin{cases} \frac{64}{Re}, & Re < 2320 \\ \frac{0.3164}{Re^{0.25}}, & 4 \times 10^3 < Re < 10^5 \\ 0.0032 + 0.221 Re^{-0.237}, & 10^5 < Re < 2 \times 10^6 \end{cases} \quad (4-27)$$

The differential term of Equation (4-20) is evaluated with Equation (4-22) and Equation (4-23):

$$\left| \frac{du_l}{dx} \right| = \frac{u^{*2}}{\nu_l} \left| \frac{du^+}{dx^+} \right|. \quad (4-28)$$

Based on the assumption from Equation (4-24) and inserting the definition of the non-dimensional velocity (Equation (4-22)):

$$\left| \frac{du_l}{dx} \right| = \frac{u^{*2}}{\nu_l} = \frac{\tau_w}{\mu_l}. \quad (4-29)$$

This can be integrated to yield the expected result:

$$u_l(y) = \frac{\tau_w}{\mu_l} y. \quad (4-30)$$

where $u_l(y=0) = 0$ as a result of the no-slip condition at the wall. This again assumes a linear velocity profile very near the wall ($y^+ \leq 5$). For the case of analyzing the critical conditions for bubble lift off, inserting Equation (4-29) and Equation (4-30) into the expression for G_s (Equation (4-20)) it is found that G_s simplifies to 1.

$$G_s = \left| \frac{du_l}{dx} \right| \frac{y}{u_l(y)} = \frac{\tau_w}{\mu_l} \frac{y}{\frac{\tau_w}{\mu_l} y} = 1. \quad (4-31)$$

It is noted that this equation is only valid for distances very near to the wall for $y^+ \leq 5$ (i.e. very small bubble sizes). With the derived relations above, the shear lift force induced on a growing bubble by a flow parallel to the surface can be determined.

4.3. Net Force Balance

Combining the results of all the individual forces derived results in a net force balance. The balance equation for the forces studied here is expressed as:

$$F_{\sigma,y} = F_{inert,y} + F_{vm} + F_{sL} \quad (4-32)$$

$$2\pi\sigma a \sin(\theta) = \left(\frac{q_i''}{h_{fg}} \right)^2 \frac{\pi(a^2 + H_b^2)}{\rho_v} + C_{vm} \frac{\rho_l}{\rho_v} \left(\frac{q_i''}{h_{fg}} \right)^2 \frac{\pi(a^2 + H_b^2)}{\rho_v} + \frac{1}{2} C_L \rho_l u_l^2|_{H/2} \pi r_b^2 \quad (4-33)$$

Solving for the interfacial heat flux (q_i''), the evaporative component of the heat flux from a single bubble represented in Equation (4-3) can be expressed as:

$$q_i'' = \left(\frac{2\pi\sigma a \sin(\theta) - \frac{1}{2} C_L \rho_l u_l |_{H/2}^2 \pi r_b^2}{\frac{\pi(a^2 + H_b^2)}{\rho_v h_{fg}^2} \left(1 + C_{vm} \frac{\rho_l}{\rho_v}\right)} \right)^{1/2} \quad (4-34)$$

The fractional boiling area is determined from the nucleation site area density (Na), the average bubble size (\bar{A}_b), and the total heated area (A_h).

$$f_{boil} = Na A_h \frac{\bar{A}_b}{A_h} = Na \bar{A}_b \quad (4-35)$$

The total contribution to the convective heat flux is then:

$$f_{conv} = 1 - f_{boil} \quad (4-36)$$

The Nusselt number for the convective heat transfer coefficient is determined from standard single phase convective relations such that:

$$Nu = \frac{\bar{h}_{conv} L_c}{k_f} \quad (4-37)$$

and

$$q_{1\phi}'' = \bar{h}_{conv} (T_w - T_{bulk}) \quad (4-38)$$

The total heat transfer is then expressed as:

$$q_{total}'' = \bar{h}_{conv} (T_w - T_{bulk}) (1 - f_{boil}) + \left(\frac{2\pi\sigma a \sin(\theta) - \frac{1}{2} C_L \rho_l u_l |_{H/2}^2 \pi r_b^2}{\frac{\pi(a^2 + H_b^2)}{\rho_v h_{fg}^2} \left(1 + C_{vm} \frac{\rho_l}{\rho_v}\right)} \right)^{1/2} f_{boil} \quad (4-39)$$

This equation will give the maximum potential heat transfer for flow boiling and will be compared to experimental work in the following section.

4.4. Closure Relations

A set of closure relations are necessary in-order to obtain a final solution. The remaining parameters to be defined are:

- nucleation site cavity size
- bubble-surface contact angle

- bubble-surface contact radius
- bubble radius
- wall superheat
- nucleation site density
- convective heat flux

The choice and justification for each parameter and relation is described in the following subsections.

4.4.1. Surface Cavity Size

Hino and Ueda [10] reported that for R113 on a stainless steel surface the maximum cavity size ranged from 0.22 microns to 0.34 microns. An average cavity size of 0.35 microns is used in this study for all conditions assuming similar surface conditions. It is noted however that a distribution of cavity sizes is expected with the total availability of cavities increasing with increasing wall superheat. This can be seen by investigation of Figure 4-2 with the use of the Clausius-Clapeyron relation:

$$\Delta T_w = \frac{2\sigma T_{sat}}{\lambda \rho_v r_c} \quad (4-40)$$

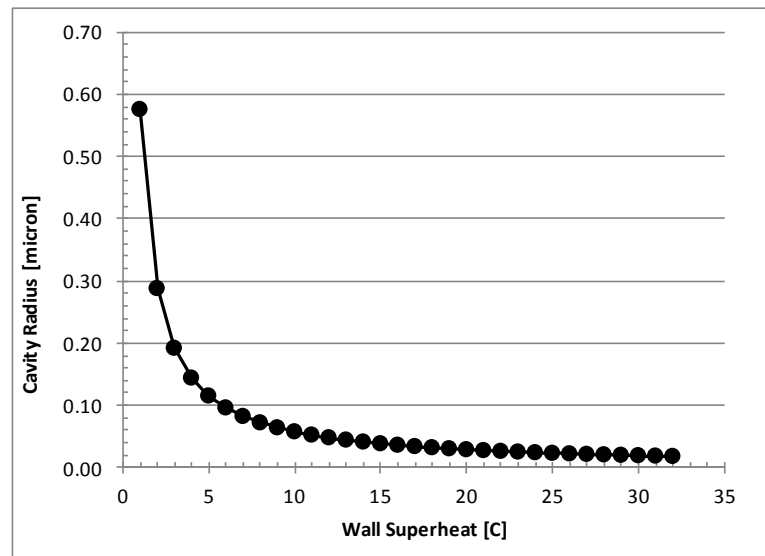


Figure 4-2 Activated minimum cavity size versus wall superheat

The net integrated number of nucleation sites increases with increasing wall superheat conditions.

4.4.2. Bubble Contact Angle

A contact angle of 45.0° is assumed.

4.4.3. Bubble Contact Radius and Bubble Radius

The bubble radius (r_b) is taken to be an average radius calculated by the average cavity size (Section 4.4.1) where the bubble radius is calculated from the cavity size and contact angle by Equation (4-41).

$$r_b = \frac{a}{\sin(\theta)} \quad (4-41)$$

The bubble radius is used in combination with the contact angle to determine the bubble height as:

$$H_b = r_b (1 + \cos(\theta)) \quad (4-42)$$

4.4.4. Wall Superheat

The wall superheat for Equation (4-45) is approximated by a static force balance on a bubble in contact with a surface:

$$\Delta P = \frac{2\sigma}{r_c} \quad (4-43)$$

The cavity size here is taken to be smallest active cavity size and differs from the average active cavity size. The smallest active cavity size is the calibration factor for experimental and model results and is dependent on the surface conditions. This method is employed since detailed surface temperature is not known from experimental results. Based on the internal vapor pressure the wall superheat is approximated as the saturation temperature at the bubble internal pressure:

$$T_w \approx T_{sat}(P_v) \quad (4-44)$$

4.4.5. Nucleation Site Density

The nucleation site density as a function of wall superheat was fit by Basu [11] based on experimental data. Most data was correlated to within 40% as shown by Figure 4-3.

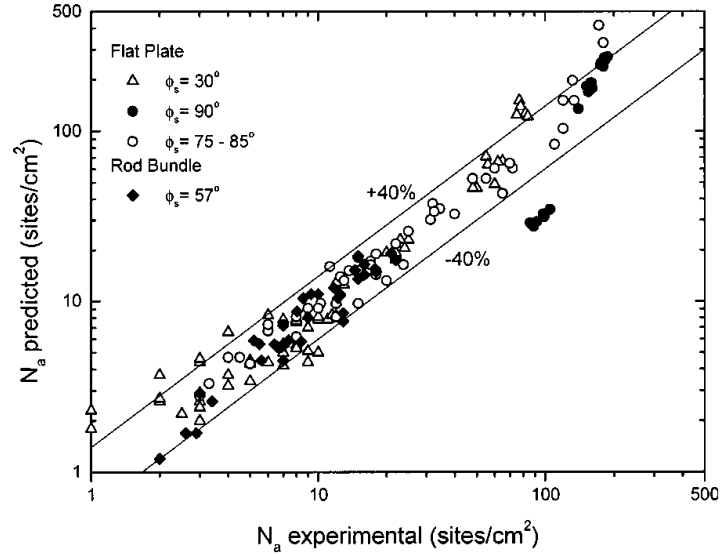


Figure 4-3 Nucleation site density correlation comparison to experimental data from Basu [11]

The correlation that describes Figure 4-3 is:

$$\begin{aligned} N_a &= 0.34(1 - \cos(\theta_s))\Delta T_w^{2.0}, & \Delta T_w < 15^\circ \\ N_a &= 3.4 \times 10^{-5}(1 - \cos(\theta_s))\Delta T_w^{5.3}, & \Delta T_w \geq 15^\circ \end{aligned} \quad (4-45)$$

where,

N_a = nucleation site density $[sites / cm^2]$

θ_s = static contact angle $[degrees]$

ΔT_w = wall superheat temperature $[^\circ C]$

This is used in (4-35) to determine the boiling fraction of the entire heated surface area. This also determines the convective heat transfer fraction of the heated surface as defined by Equation (4-36). It is noted that with the use of two equations that discontinuities may be expected for varying wall superheats within a channel.

4.4.6. Convective Heat Flux Correlation

The convective heat correlation used is the simple Dittus-Boelter relation:

$$Nu = 0.023Re^{0.8}Pr^n$$

where,

$$Pr = \frac{c_p \mu}{k} \quad (4-46)$$

$n = 0.4$ for heating or 0.3 for cooling

This is used in Equation (4-37) to determine the convective heat transfer coefficient.

4.5. Model Implementation Algorithm

An overview of the algorithm proposed for determining the critical heat flux is given in Figure 4-4. The theoretically derived critical heat flux is solved axially in a flow channel. This is then compared to experimental data to validate the newly developed mechanistic model that is centered on a momentum balance of a bubble at a nucleation site.

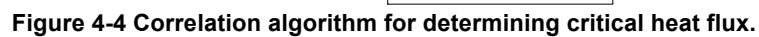


Figure 4-4 Correlation algorithm for determining critical heat flux.

5. RESULTS

5.1. Nodalization

The nodalization employed for the low and high pressure test models are equivalent. A one-dimensional axial nodalization is defined with three sub=regions. The first region is the heat source modeled simply as boundary condition. The second is the fluid near the wall utilizing fluid properties at the wall temperature. The last region is the bulk region where fluid properties are determined by a one-dimensional energy balance in the channel. Figure 5-1 depicts the general nodalization scheme and the three sub-regions.

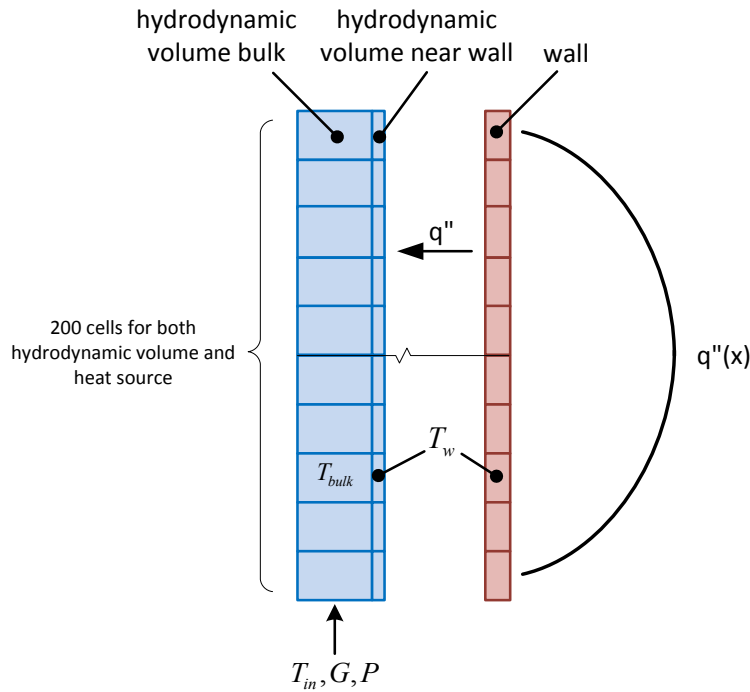


Figure 5-1 Nodalization of the critical heat flux model.

5.2. Calibration

Based on the high and low pressure data a calibration was performed to determine the active nucleation cavity size. This is used only to determine the wall superheat value. Dependence was found to be mainly related to the system pressure (Figure 5-2). The following form was developed:

$$a[m] = 0.7442 \times 10^{-6} P_{sys} [MPa]^{-0.977}$$

$$a[m] = 0.0785 \times 10^{-6} P_{sys} [bar]^{-0.977}$$

(5-1)

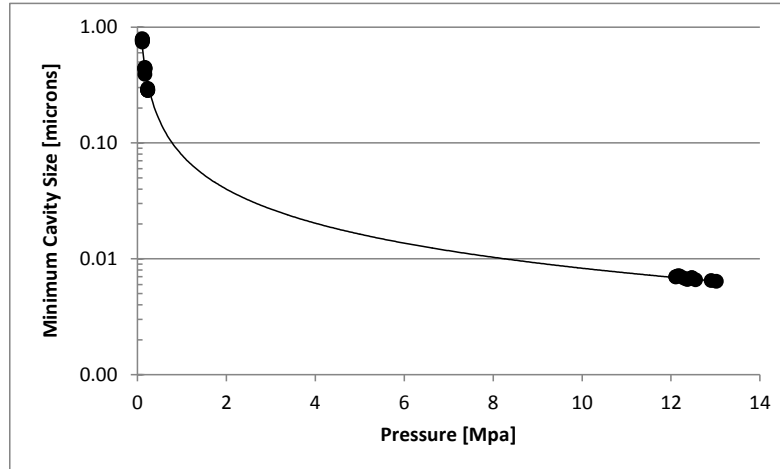
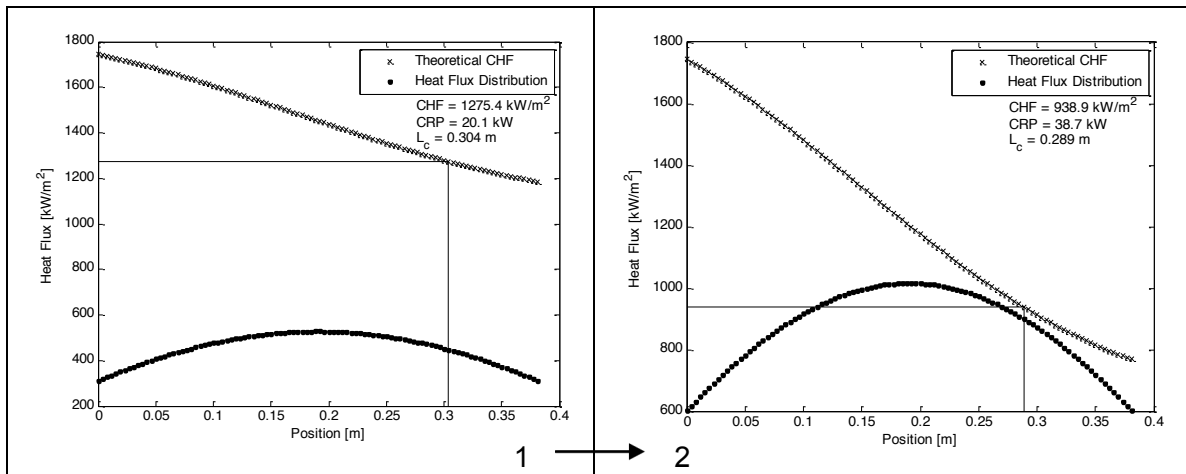


Figure 5-2 Relation between system pressure and minimum active cavity radius.

5.3. Convergence Criteria

Iterations were performed between the model predicted heat flux distribution and the predicted critical heat flux curve. The model pin power was iteratively increased until it made contact with the critical heat flux curve. This process is shown in Figure 5-3 for the first low-pressure case. A total of 6 iterations were required to obtain the final results for this case. Convergence was determined by the distance between closest point on the critical heat flux curve and pin heat flux. A value of 0.01% was used for all tests.



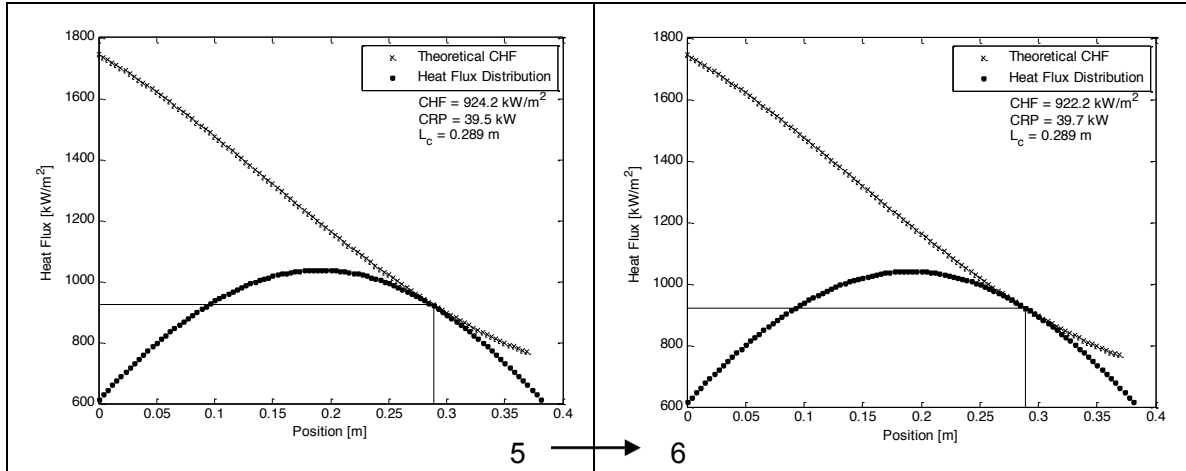


Figure 5-3 Convergence process for determining the critical heat flux.

5.4. Critical Rod Power

As can be seen by Table 5-2 and Figure 5-4 excellent agreement exists between the experimental critical rod power and that predicted by the proposed model. The highest error for the high pressure tests is less than 7% and a mean error of -2.40%. The low pressure tests do not perform as well with a maximum error less than 60% and mean error of -1.85%. It is interesting to note that for the low pressure data the mean error is very low while the max error is rather high. This potential shows the variability of the critical heat flux value at low-flow and low-pressure conditions. The high pressure results are very tight together (Figure 5-4) indicating a more consistent critical heat flux at high pressures and moderate flow.

Table 5-1 Model performance on predicting the critical heat flux.

Test # ^[1]	CHF Value [kW/m ²]		% Error
	Experiment	Model	
HP1	46.06	45.45	1.33%
HP2	51.03	51.56	-1.04%
HP3	52.00	51.16	1.62%
HP4	55.98	57.14	-2.07%
HP5	55.98	57.09	-1.98%
HP6	39.98	39.75	0.57%
HP7	40.67	41.06	-0.96%
HP8	45.00	47.34	-5.21%
HP9	45.00	47.44	-5.41%
HP10	50.01	53.26	-6.50%
HP11	49.00	52.30	-6.73%
LP1	33.48	39.67	-18.50%
LP2	32.47	39.67	-22.18%
LP3	30.88	37.53	-21.53%

Test # ^[1]	CHF Value [kW/m ²]		% Error
	Experiment	Model	
LP4	23.01	28.40	-23.42%
LP5	19.54	31.15	-59.40%
LP6	38.70	37.82	2.28%
LP7	37.70	38.05	-0.92%
LP8	35.20	34.59	1.73%
LP9	29.24	23.49	19.68%
LP10	22.07	21.89	0.82%
LP11	44.90	37.35	16.81%
LP12	43.88	37.35	14.88%
LP13	40.74	33.59	17.55%
LP14	24.96	16.60	33.49%
LP15	31.46	37.62	-19.57%
LP16	37.69	35.22	6.54%
LP17	41.88	33.36	20.34%

^[1] HP=high pressure tests; LP=low pressure tests.

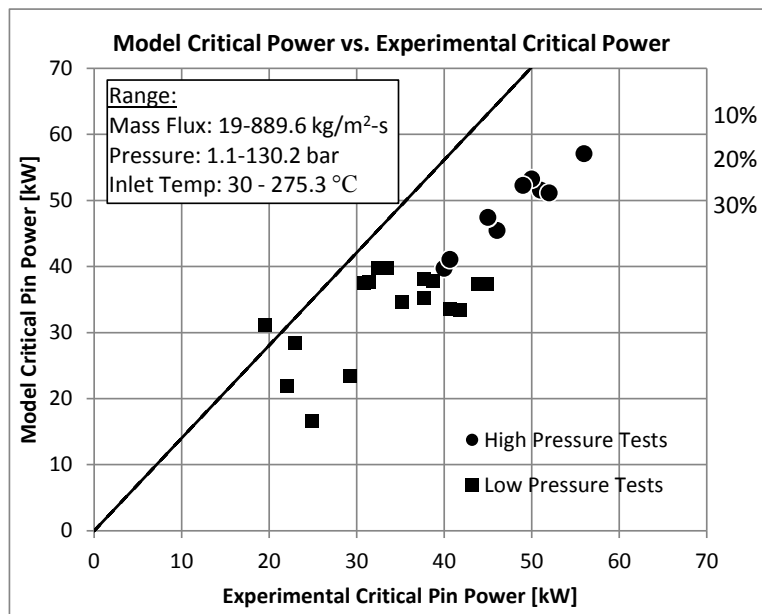


Figure 5-4 Model pin critical power comparison to experimental data.

5.5. Critical Heat Flux Value

The actual critical heat flux value location and value were not reported for the low-pressure data; only the high pressure data is discussed here. Figure 5-5 and Table 5-2 show the results of the value of the critical heat flux and associated error. The average model error is 23.55% compared to the data showing that the model tends to under-predict the critical heat flux location. Under-prediction of the CHF locations results in an over-prediction of the CHF value as shown in Section 5.5.

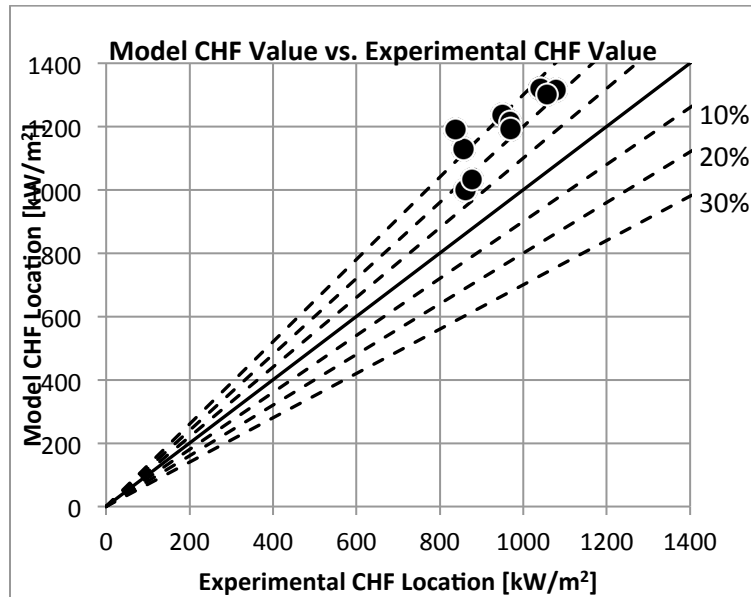


Figure 5-5 Model critical heat flux value comparison to experimental data.

Table 5-2 Model performance on predicting the critical heat flux.

Test # ^[1]	CHF Value [kW/m^2]		% Error
	Experiment	Model	
HP1	856.70	1128.26	-31.70%
HP2	950.87	1236.40	-30.03%
HP3	968.44	1213.56	-25.31%
HP4	1042.03	1322.15	-26.88%
HP5	1041.97	1320.76	-26.76%
HP6	861.90	998.85	-15.89%
HP7	877.82	1031.91	-17.55%
HP8	837.67	1189.47	-42.00%
HP9	969.24	1191.13	-22.89%
HP10	1077.60	1314.60	-21.99%
HP11	1056.04	1301.47	-23.24%
LP1	Not Reported	922.11	-
LP2		922.11	-
LP3		863.39	-
LP4		745.16	-
LP5		737.77	-
LP6		895.93	-
LP7		909.35	-
LP8		795.85	-
LP9		556.42	-
LP10		543.24	-
LP11		900.14	-
LP12		900.14	-
LP13		788.43	-
LP14		435.30	-
LP15		913.76	-

Test # ^[1]	CHF Value [kW/m ²]		% Error
	Experiment	Model	
LP16		868.34	-
LP17		828.02	-

^[1] HP=high pressure tests; LP=low pressure tests.

5.6. Critical Heat Flux Location

The proposed model allows for calculation of the critical heat flux location. The actual critical heat flux value location and value were not reported for the low-pressure data; only the high pressure data is discussed here. Figure 5-6 and Table 5-3 show the results of the value of the critical heat flux and associated error. The average model error is -26% compared to the data showing that model tends to over-predict the critical heat flux value. This is also dependent on the predicated location of the CHF occurrence as discussed in Section 5.6.

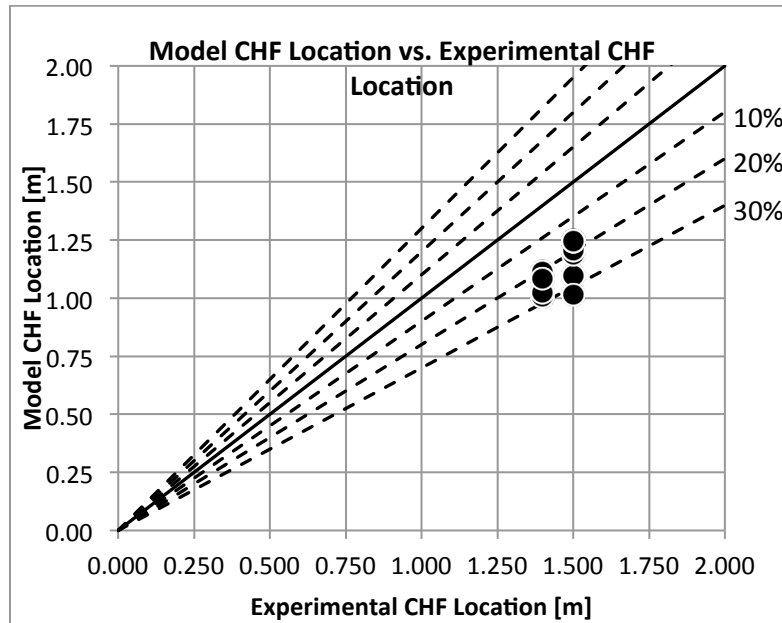


Figure 5-6 Model critical heat flux comparison to experimental data.

Table 5-3 Model performance on predicting the critical heat flux location.

Test # ^[1]	CHF Value [kW/m ²]		% Error
	Experiment	Model	
HP1	1.500	1.10	26.97%
HP2	1.500	1.19	20.94%
HP3	1.500	1.21	19.60%
HP4	1.500	1.25	16.92%
HP5	1.500	1.25	16.92%
HP6	1.398	1.01	28.10%
HP7	1.398	1.01	28.10%
HP8	1.500	1.02	32.33%

Test # ^[1]	CHF Value [kW/m ²]		% Error
	Experiment	Model	
HP9	1.398	1.03	26.66%
HP10	1.398	1.12	20.19%
HP11	1.398	1.09	22.34%
LP1	Not Reported	0.29	-
LP2		0.29	-
LP3		0.29	-
LP4		0.18	-
LP5		0.10	-
LP6		0.28	-
LP7		0.28	-
LP8		0.29	-
LP9		0.28	-
LP10		0.12	-
LP11		0.27	-
LP12		0.27	-
LP13		0.28	-
LP14		0.18	-
LP15		0.27	-
LP16		0.26	-
LP17		0.26	-

^[1] HP=high pressure tests; LP=low pressure tests.

6. CONCLUSIONS

A mechanistic base critical heat flux model has been developed and assessed against low- and high-pressure data under various flow conditions. The current dataset evaluated lacked information in the intermediate pressure region ($1 \text{ MPa} < P < 10 \text{ MPa}$); however a single calibration curve was developed to determine the wall superheat for both extremes of data presented in this summary. The model developed allows for determination of the critical heat value, the critical heat flux location, and the critical pin power for a given set of power profiles and test conditions.

7. REFERENCES

1. Avery, M., et al., *Critical Heat Flux in TRIGA-Fueled Reactors Cooled by Natural Convection*. Nuclear Science and Engineering, 2012. **172**(3): p. 249-258.
2. Katto, Y., *Generalized Correlations for Critical Heat Flux of Natural Convection Boiling in Confined Channels*. Transactions of The Japan Society of Mechanical Engineers (in Japanese), 1978. **44**(387): p. 3908-3911.
3. Oh, C.H. and S.B. Englert, *CRITICAL HEAT-FLUX FOR LOW FLOW BOILING IN VERTICAL UNIFORMLY HEATED THIN RECTANGULAR CHANNELS*. International Journal of Heat and Mass Transfer, 1993. **36**(2): p. 325-335.
4. Lowdermilk, W.H., C.D. Lanzo, and B.L. Siegel, *Investigation of boiling burnout and flow instability of water flowing in tubes*, N.A.C.f. Aeronautics, Editor. 1958, Lewis Flight Propulsion Laboratory: Cleveland, OH.
5. Monde, M., H. Kusuda, and H. Uehara, *Critical Heat-Flux during Natural Convective Boiling in Vertical Rectangular Channels Submerged in Saturated Liquid*. Journal of Heat Transfer-Transactions of the Asme, 1982. **104**(2): p. 300-303.
6. Kaichiro, M. and M. Ishii, *Flow regime transition criteria for upward two-phase flow in vertical tubes*. International Journal of Heat and Mass Transfer, 1984. **27**(5): p. 723-737.
7. Mishima, K. and H. Nishihara, *The effect of flow direction and magnitude on CHF for low pressure water in thin rectangular channels*. Nuclear Engineering and Design, 1985. **86**(2): p. 165-181.
8. Kaminaga, M., et al., *Experimental study of critical heat flux in a narrow vertical rectangular channel*. Nippon Kikai Gakkai Ronbunshu, B Hen, 1989. **55**(517): p. 2809-2813.
9. Klausner, J.F., et al., *Vapor Bubble Departure in Forced-Convection Boiling*. International Journal of Heat and Mass Transfer, 1993. **36**(3): p. 651-662.
10. Hino, R. and T. Ueda, *Studies on Heat Transfer and Flow Characteristics in Subcooled Flow Boiling-Part I. Boiling Characteristics*. International Journal of Multiphase Flow, 1985. **11**(3): p. 269-281.
11. Basu, N., G.R. Warrier, and V.K. Dhir, *Onset of Nucleate Boiling and Active Nucleation Site Density During Subcooled Flow Boiling*. Journal of Heat Transfer, 2002. **124**(4): p. 717-728.